

**MODELLING OF RESIDUAL STRESS RELAXATION OF SHOT-
PEENED ASTM A516 GRADE 70 STEEL**

MOHD RASHDAN BIN ISA

**COLLEGE OF GRADUATE STUDIES
UNIVERSITI TENAGA NASIONAL**

2020

**MODELLING OF RESIDUAL STRESS RELAXATION OF SHOT-
PEENED ASTM A516 GRADE 70 STEEL**

MOHD RASHDAN BIN ISA

**A Thesis Submitted to the College of Graduate Studies, Universiti
Tenaga Nasional in Fulfilment of the Requirements for the Degree of**

Doctor of Philosophy (Engineering)

JANUARY 2020

DECLARATION

I hereby declare that the thesis is my original work except for quotations and citations which have been duly acknowledged. I also declare that it has not been previously, and is not concurrently submitted for any other degree at Universiti Tenaga Nasional or at any other institutions. This thesis may be made available within the university library and may be photocopied and loaned to other libraries for the purpose of consultation.

MOHD RASHDAN BIN ISA

Date :

ABSTRACT

Residual stress is defined as the remaining stress present in an object with the absence of an external load. It can be divided into tensile and compressive residual stress. Compressive residual stress is beneficial to prolong the fatigue life of the product especially for products made of metallic material. It was demonstrated that the fatigue life of metallic materials can be extended by the near-surface macroscopic compressive residual stress which can be introduced by shot peening process whereby fatigue crack initiation and crack growth can be reduced. However, the initial residual stress field inherent or induced in the finished product may not remain stable during the operation due to the relaxation of the residual stress. The previous empirical model to predict the residual stress relaxation did not incorporate the surface hardness parameter. The main objective of this research is to determine the relaxation of the residual stress of ASTM A516 Grade 70 carbon steel which is widely used in the automotive and oil industries. Empirical and numerical model were particularly generated for this material at the end of this research. This study involved simulation and experimental methods. The simulation part was performed by developing a CAD model with the same dimension of the actual sample. The simulation method consists of shot peening simulation to induce the initial residual stress and simulation was the residual stress relaxation. On the other hand, the experimental part began with the preparation of the sample material according to standard dimension, followed by the introduction of residual stress in the material through shot peening process at low and high intensities. The cyclic load was applied to both variables with low load (20% of Yield Strength) and high load (80% of Yield Strength). The load was varied by the number of cycles. Finally, the residual stress was measured using X-Ray diffraction on the samples to study the relaxation trend. Based on the results, the residual stress relaxed during the first cycle. The experiment results of residual stress relaxation was validated numerically and showed good agreement. Hence, the experimental result was validated by the simulation result. Finally, two sets of equations (numerical model) were developed for the residual stress relaxation of this material. Of the two, the FE model developed can be used to predict the value of residual stress in any cycle.

ACKNOWLEDGMENT

Alhamdulillah, thanks to Allah S.W.T, whom with His willing giving me the opportunity to complete my PhD dissertations. I would like to express my gratitude to my supervisor, Dr. Omar Suliman Zaroog on his support and supervision from every aspect throughout the completion of this study. Without his guidance, I would not be able to handle this study wisely. Also thanks to my colleague Saiful Naim Sulaiman from Universiti Teknikal Melaka who was my field supervisor. Without his expertise in the finite element method, I could have never completed my simulation activity which is the key to this study.

I dedicate my sincere gratitude to my loving and caring wife who always there for me during my sick and health, during my pain and struggle. She is the one who sacrifice her energy and time to take care of our beloved children while I was doing this study. Without her sacrifice, I would have never completed this study according to the plan. To my beautiful children, Adam Rifa'ie, Siti A'isyah, Ahmad Raihan and Siti Aafiyah, I could never thank enough. You have made me stronger, better and more fulfilled than I could have ever imagined. I love you to the moon and back. Not to forget, my mother Kamariah Bt. Mohd Tahir and my late father Isa Bin Yaacob who always prayed for my success.

Last but not least, I acknowledge my greatest thanks to Universiti Tenaga Nasional for all support and accommodations given to complete this study.

DEDICATION

I dedicate this dissertation to Universiti Tenaga Nasional by sponsoring me through Uniten BOLD Scholarship, Uniten Internal Grant (UNIIG 2017) as well as Ministry of Higher Education Malaysia (MOHE) through the FRGS grant number FRGS/1/2015/TK03/UNITEN/02/3. The funding by these institutes were a major factor of succeeding this study. I would also like to acknowledge the Innovation and Research Management Centre (iRMC) of Universiti Tenaga Nasional for continuous support during this study.

TABLE OF CONTENTS

	Page
DECLARATION	ii
ABSTRACT	iii
ACKNOWLEDGMENT	iv
DEDICATION	v
TABLE OF CONTENTS	vi
LIST OF TABLES	x
LIST OF FIGURES	xiii
LIST OF SYMBOLS	xvii
LIST OF ABBREVIATIONS	xix
LIST OF PUBLICATIONS	xx
CHAPTER 1 INTRODUCTION	1
1.1 Background of study	1
1.2 Problem statement	3
1.3 Research objectives	4
1.4 Scope and limitation of study	5
1.5 Thesis organisation	5
CHAPTER 2 LITERATURE REVIEW	7
2.1 Introduction	7
2.2 Material ASTM A516 grade 70 carbon steel	8
2.3 Material properties	9
2.3.1 Tensile properties	10
2.3.2 Hardness properties	10
2.3.3 Fatigue properties	11

2.3.4	Surface roughness properties	12
2.3.5	Morphological characterisation	12
2.4	Shot peening process	13
2.4.1	Almen Strip	16
2.4.2	Shot size	18
2.4.3	Shot angle	20
2.4.4	Shot velocity	20
2.4.5	Effect of shot peening on material	21
2.5	Shot peening simulation	23
2.5.1	Single shot simulation	23
2.5.2	Multiple shot simulation	26
2.6	Simulation software	29
2.6.1	Comparison of simulation software	29
2.7	Residual stress	31
2.7.1	Methods of introducing residual stress	31
2.7.2	Residual stress effect on fatigue properties	34
2.7.3	Incorporating the concept of residual stress into the design	36
2.7.4	Residual stress measurement	38
2.8	Residual stress relaxation	48
2.8.1	Previous works on residual stress relaxation	50
2.9	Modelling of residual stress relaxation	50
2.10	Summary of literature review	53
CHAPTER 3	MATERIALS AND METHODOLOGY	56
3.1	Introduction	56
3.2	Experiments	59
3.2.1	Sample preparation	59
3.2.2	Raw material control (mechanical and microscopic test)	60

3.2.3	Shot peening process	64
3.2.4	Mechanical test on shot-peened material	66
3.2.5	Cyclic loading	66
3.2.6	Residual stress measurement (X-Ray diffraction)	67
3.2.7	Surface roughness measurement	68
3.3	Simulation	69
3.3.1	CAD modelling	69
3.3.2	Defining material properties	71
3.3.3	Meshing	71
3.3.4	Shot peening simulation	75
3.3.5	Residual stress relaxation simulation	78
CHAPTER 4	RESULTS AND DISCUSSION	81
4.1	Introduction	81
4.2	Experimental results	81
4.2.1	Tensile behaviour	81
4.2.2	Hardness	83
4.2.3	Fatigue behaviour	87
4.2.4	Microscopy test	88
4.2.5	Residual stress induced by shot peening process	91
4.2.6	Residual stress relaxation against cyclic loading	91
4.2.7	Surface roughness	98
4.2.8	Empirical modelling of residual stress relaxation	99
4.3	Simulation results	104
4.3.1	Shot peening simulation result	104
4.3.2	Mesh convergence result	107
4.3.3	Residual stress relaxation simulation result	109
4.3.4	Numerical modelling of residual stress relaxation	119
4.3.5	Validation of experimental result by simulation result	121

CHAPTER 5	CONCLUSION AND RECOMMENDATIONS FOR	
	FUTURE WORK	128
5.1	Conclusion	128
5.2	Recommendation for future works	130
	REFERENCES	131
	APPENDIX A	146
	APPENDIX B	154

LIST OF TABLES

Table 2.1	Chemical composition of ASTM A516 Grade 70 Carbon Steel	8
Table 2.2	Physical, mechanical, electrical and thermal properties of ASTM A516 Grade 70 steel	9
Table 2.3	Cast shot numbers and screening tolerances	19
Table 2.4	Result of saturation study on L-type aluminium test strips, T-type aluminium test strips and A-type Almen strips	20
Table 2.5	Advantages and disadvantages of ANSYS, Abaqus and HyperWorks	29
Table 2.6	Main origins of residual stress from different manufacturing processes	33
Table 2.7	Increase in the fatigue life of various mechanical components as a result of shot-peening	37
Table 2.8	Summary of previous studies on modelling of residual stress relaxation	54
Table 3.1	Shot peening A parameters	65
Table 3.2	Shot peening B parameters	66
Table 3.3	Diffractionmeter parameter	68
Table 3.4	Dimensions of CAD model	69
Table 3.5	Number of elements and element densities for shot peening models	73
Table 3.6	Shot peening simulation parameters	77
Table 4.1	Rockwell hardness value of ASTM A516 Grade 70	83

Table 4.2	Hardness reduction for shot-peened material by 6.28 A and 12.9 A intensities against cyclic load with 52 MPa and 208 MPa amplitudes	84
Table 4.3	Summary of fatigue test results before and after shot peening	88
Table 4.4	Residual Stress after Cyclic Loads for shot-peened samples with intensity 6.28 A	91
Table 4.5	Residual Stress after Cyclic Loads for shot-peened samples with intensity 12.9 A	93
Table 4.6	Surface roughness result before and after SP B	98
Table 4.7	Constant values of residual stress relaxation shot peening with intensity 6.28 A	99
Table 4.8	Constant values of residual stress relaxation shot peening with intensity 12.9 A	99
Table 4.9	Constant values of hardness reduction constants in low cyclic region for shot peening with intensity 6.28 A and 12.9 A	100
Table 4.10	Constant values of hardness reduction constants in high cyclic region for shot peening with intensity 6.28 A and 12.9 A	101
Table 4.11	Values for constant A, B, C and D for low cyclic region model	102
Table 4.12	Values for constant E, F, I and J for low cyclic region model	103
Table 4.13	Residual stress values for each shot speed	105
Table 4.14	Mesh sensitivity study	108
Table 4.15	Simulation result of residual stress values against cyclic loads for intensity 6.28 A and 12.9A	112

Table 4.16	Residual stress relaxation constants for of low cyclic region for shot peening with intensity 6.28 A and 12.9A	119
Table 4.17	Residual stress relaxation constants for of high cyclic region for shot peening with intensity 6.28 A and 12.9A	120

LIST OF FIGURES

Figure 1.1	Different types of macro and micro residual stress	1
Figure 2.1	Schematic representation of the SP process	15
Figure 2.2	Schematic illustration of a shot immediately before and after impinging the surface	15
Figure 2.3	The mechanics: (a) a shot impacts a component, (b) on the rebound of the shot	16
Figure 2.4	Schematic diagram of: low coverage	16
Figure 2.5	The shot stream applied on Almen strip for the intensity measurement	17
Figure 2.6	Almen saturation curve against exposure time	18
Figure 2.7	A schematic illustration of impact angle	23
Figure 2.8	Geometry of a sphere in normal contact with a plane	24
Figure 2.9	(a) Residual stress produced by plastic deformation in the absence of heating (b) Residual stress resulting from exceeding the elastic limit after the presence of a temperature gradient	32
Figure 2.10	Effect of residual stress on fatigue lifetime (a) constant life plot for mean stress versus stress amplitude; (b) effective stress intensity range ΔK_{eff} for two compressive residual stress levels (A, B) with non-zero crack closure stress intensity factor K_{cl}	35
Figure 2.11	Basis of method for monitoring development of residual stresses during deposition, experimental data were obtained for various thicknesses of sputtered	39
Figure 2.12	Hole drilling apparatus	41
Figure 2.13	Sample and laboratory coordinate systems	47
Figure 2.14	Residual stress relaxation before and after cyclic loading	48
Figure 2.15	Residual stress relaxation at the surface of a specimen	49
Figure 3.1	Overall research flow	58
Figure 3.2	Detail drawing of test sample sent for cutting	59
Figure 3.3	Actual sample after cutting process	60

Figure 3.4	Tensile test equipment	61
Figure 3.5	Hardness measurement equipment	62
Figure 3.6	SEM machine	63
Figure 3.7	Shot peening process	65
Figure 3.8	Universal testing machine for cyclic loading and fatigue test	67
Figure 3.9	TR200 surface roughness measurer	68
Figure 3.10	Detail dimension of the model	70
Figure 3.11	CAD model of test sample in 3D view	70
Figure 3.12	Mesh geometry of 8-node linear brick (HEPH)	72
Figure 3.13	Meshed area	72
Figure 3.14	Different mesh size for middle area on the body (a) Model 1: Uniform mesh size in whole body (5 x 5 element density);(b) Model 2: Fine mesh in middle area (10 x 10 element density);(c) Model 3: Fine mesh in middle area (18 x 15 element density);(d) Model 4: Fine mesh in middle area (30 x 30 element density); (e) Model 5: Fine mesh in middle area (40 x 40 element density)	73
Figure 3.15	Direction of ball shot direction and angle towards the impact of the shot peening simulation model	77
Figure 3.16	Boundary condition and load setup	78
Figure 3.17	Cyclic load function defined in the residual stress relaxation simulation (a) low cyclic tensile loading (b) high cyclic tensile loading	80
Figure 4.1	Stress-strain curve for raw material and shot-peened ASTM A516 grade 70 steel	82
Figure 4.2	Broken sample after tensile test	82
Figure 4.3	Hardness values against number of cycle for shot peening with intensity 6.28 A (a) 0 to 10,000 cycles (b) 0 to 10 cycles	84
Figure 4.4	Hardness values against number of cycle for shot peening with intensity 12.9 A (a) 0 to 10,000 cycles (b) 0 to 10 cycles	86

Figure 4.5	Grain size of ASTM A516 Grade 70 microstructure. Tensile fracture before and after shot peening A (a) SEM before shot peening (b) SEM after shot peening	89
Figure 4.6	Grain size of ASTM A516 Grade 70 microstructure. Tensile fracture before and after shot peening B (a) SEM before shot peening (b) SEM after shot peening 6.28 A (c) SEM after shot peening 12.9 A	90
Figure 4.7	Experimental residual stress relaxation against cyclic load for shot-peened material with intensity 6.28 A (a) 0 to 1000 cycles; (b) 0 to 10 cycles	92
Figure 4.8	Experimental residual stress relaxation against cyclic load for shot-peened material with intensity 12.9 A (a) 0 to 1000 cycles; (b) 0 to 10 cycles	94
Figure 4.9	Residual stress relaxation against cyclic loading with amplitude of 52 MPa for intensities 6.28 A and 12.9 A (a) 0 to 1000 cycles; (b) 0 to 10 cycles	96
Figure 4.10	Residual stress relaxation against cyclic loading with amplitude of 208 MPa for intensities 6.28 A and 12.9 A (a) 0 to 1000 cycles; (b) 0 to 10 cycles	97
Figure 4.11	Result of simulation of shot peening (a) 3D view (b) Top view. The colour contours represent the different values of the stress. Red for the maximum stress where the highest impact occurred. Followed by the other colours in a descending pattern orange, yellow, greens and blues).	105
Figure 4.12	Depth measurement of the dented area after impact	106
Figure 4.13	Diameter measurement of the dented area after impact	106
Figure 4.14	Graph of stress value against number of element for the mesh sensitivity study	108
Figure 4.15	Model used in relaxation of residual stress simulation	109
Figure 4.16	The point of measurement with maximum residual stress value (node 8477)	110
Figure 4.17	Stress distribution (a) before and (b) after cyclic load applied (1 cycle)	111

Figure 4.18	Residual stress relaxation against cyclic loading with amplitude of 52 MPa and 208 MPa for intensity 6.28 A (a) 0 to 1000 cycles; (b) 0 to 10 cycles	112
Figure 4.19	Residual stress relaxation against cyclic loading with amplitude of 52 MPa and 208 MPa for intensity 12.9 A (a) 0 to 1000 cycles; (b) 0 to 10 cycles	114
Figure 4.20	Residual stress relaxation against cyclic loading with amplitude of 52 MPa for intensities 6.28 A and 12.9 A (a) 0 to 1000 cycles; (b) 0 to 10 cycles	116
Figure 4.21	Residual stress relaxation against cyclic loading with amplitude of 208 MPa for intensities 6.28 A and 12.9 A (a) 0 to 1000 cycles; (b) 0 to 10 cycles	117
Figure 4.22	Comparison between simulation and experimental residual stress relaxation of shot-peened material with intensity 12.9 A and cyclic load applied with amplitude of 52 MPa (a) 0 to 1000 cycles; (b) 0 to 10	121
Figure 4.23	Comparison between simulation and experimental residual stress relaxation of shot-peened material with intensity 12.9A and cyclic load applied with amplitude of 208 MPa	122
Figure 4.24	Comparison between simulation and experimental residual stress relaxation of shot-peened material with intensity 12.9 A and cyclic load applied with amplitude of 52 MPa (a) 0 to 1000 cycles; (b) 0 to 10	124
Figure 4.25	Comparison between simulation and experimental residual stress relaxation of shot-peened material with intensity 12.9A and cyclic load applied with amplitude of 208 MPa (a) 0 to 1000 cycles; (b) 0 to 10	126

LIST OF SYMBOLS

C	Carbon
Fe	Iron
Mn	Manganese
P	Phosphorous
Si	Silicon
S	Sulphur
D	Ball diameter
δ	Total compression
a	Contact radius
P	Load
F	Test load
\bar{E}	Equivalent Young modulus
ν_s	Poisson's ratio of shot
ν_p	Poisson's ratio of plate
E_s	Shot Young modulus
E_p	Plate Young modulus
W	Kinetic energy
W_{ep}	Elasto-plastic energy
W_d	Dissipated energy
K	Ratio of elasto-plastic energy and kinetic energy
m	Mass
V	Velocity
σ_a	Amplitude of admissible stress
σ_m	Mean fatigue stress
σ_D	Purely reverse tensile fatigue limit
R_m	True rupture strength
σ_R	Residual stress
ΔK_{eff}	Effective stress intensity range
K_{cl}	Intensity factor
σ_{RN}	Residual stress at any number of cycle
N	Number of cycle
H	Hardness (Rockwell)
A_h	Arc height

Na	Sodium
Cl	Chloride
ρ_s	Shot density
R	Shot radius
σ	Stress
E	Stiffness
g	Deflection
h	Beam current thickness
l	Beam length
V_0	Velocity in unstressed medium
λ	Wavelength
d_{hkl}	Lattice plane spacing of crystallographic planes
θ_{hkl}	Angular position of diffraction peak
d_0	Unstressed interplanar spacing
σ_{mN}	Mean stress at N th cycle
σ_{m1}	Mean stress at first cycle
σ_y	Material yield strength
$(\sigma_{res})_{ini}$	Initial residual stress
σ_0	Initial residual stress
σ_N^{re}	Residual stress at N th cycle

LIST OF ABBREVIATIONS

ASTM	American Standard for Testing and Materials
CAD	Computer Aided Design
CAE	Computer Aided Engineering
CFD	Computational Fluid Dynamics
CNC	Computer Numerical Control
CRS	Compressive Residual Stress
CTE	Coefficient of Thermal Expansion
FEA	Finite Element Analysis
FEM	Finite Element Method
ISO	International Organization for Standardization
NDT	Non-destructive Test
SAE	Society of Automotive Engineers
SEM	Scanning Electron Microscopy
S-N	Stress – Number of Cycle
SP	Shot Peening
SSP	Simultaneous Shot Peening
UTM	Universal Testing Machine
XRD	X-Ray Diffraction

LIST OF PUBLICATIONS

1. Isa, M.R., Zaroog, O.S., Murugan, K., Guma, S.O.K., Ali, F.S., Improvement of mechanical properties and fatigue life by shot peening process on ASTM A516 grade 70 steel. *Malaysian Journal of Fundamental and Applied Sciences*, 2018. 14(4): pp. 440-442.
2. Isa, M.R., Zaroog, O.S., Ali, F.S., Relationship between compressive residual stress relaxation and microhardness reduction after cyclic loads on shotpeened ASTM A516 grade 70 steel. *Key Engineering Materials*, 2018. 765: pp. 232-236.
3. Isa, M.R., Zaroog, O.S., Raj, P., Sulaiman, S.N., Abu Shah, I., Ismail, I.N., Zahari, N.M., Roslan, M.E., Mohamed, H., Numerical Analysis of Shot Peening Parameters for Fatigue Life Improvement. *AIP Conference Proceedings* 2030, 020217, 2018.
4. Isa, M.R., Zaroog, O.S., Bahrin, M.A.H.S., Ansari, M.N.M., A study of mechanical properties change and residual stress relaxation of ASTM A516 grade 70 steel after shot peening process. *Journal of Fundamental and Applied Sciences*, 2018. 10(7S): pp. 78-90.
5. Isa, M.R., Sulaiman, S.N., Zaroog, O.S., Experimental and simulation method of introducing compressive residual stress in ASTM A516 grade 70 steel. *Key Engineering Materials*, 2019. 83: pp. 27-31.

CHAPTER 1

INTRODUCTION

1.1 Background of study

Residual stress is defined as stress which remained in a body with the absence of external loading or thermal gradient. Manufacturing processes are the most common cause of residual stress that includes casting, welding, machining, moulding, heat treatment, rolling, forging and shot peening [1]. Residual stress is generated due to the misfits in the natural shape either between regions or between different phases within the material. Figure 1.1 illustrates the two types of residual stress, namely macro and micro residual stress. In many cases, these misfits span over large distances, for example, those caused by the non-uniform plastic deformation of a bent bar [2].

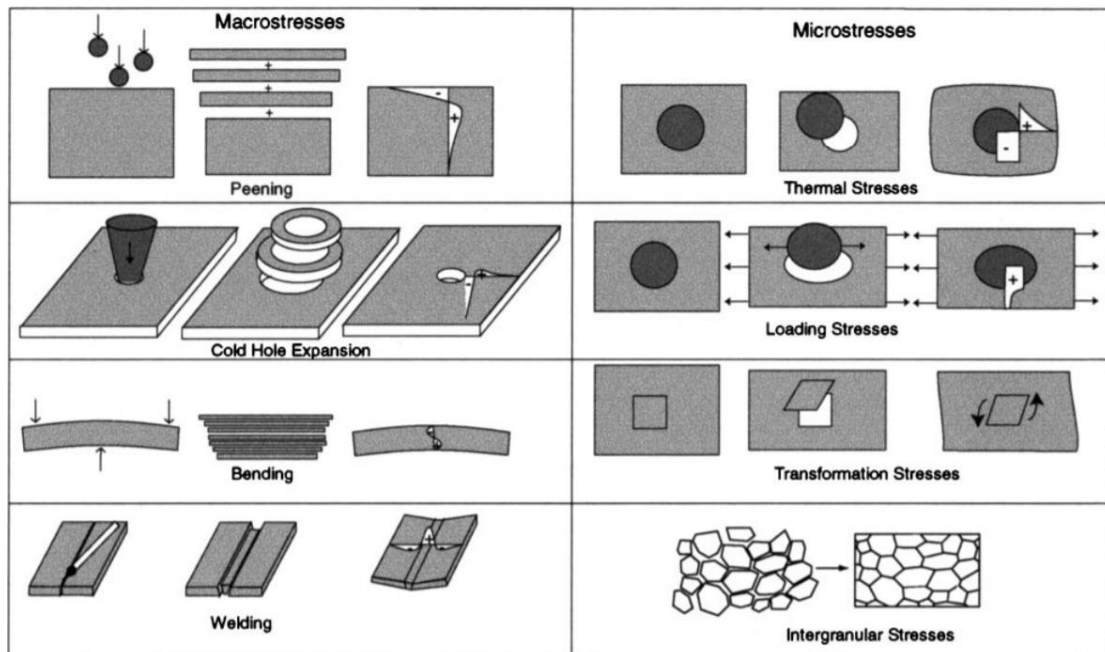


Figure 1.1 Different types of macro and micro residual stress [2].

Compressive residual stress (CRS) plays an important role in improving the fatigue life of metallic components. The fatigue life of metallic materials can be extended by the near-surface macroscopic CRS. The macroscopic CRS can be introduced through many mechanical processes whereby the fatigue crack initiation and the crack growth could be

reduced. However, compressive stress is needed to superpose the tension stress from applied external loads on the material during operation. When a part is subjected to a load for instance in a positive tensile direction, a material which is already in a positive stress state would be exposed to even higher stress as a result of a combination between original positive stress and positive tensile stress. This case is also applicable for different types for bending load applied to the component. Therefore, an appropriate finishing operation such as a shot peening can introduce compressive residual stress i.e. negative stress. A shot peening process can relieve some of the local positive load where, as a result, the mechanical performance of the materials can be increased. The introduction of the residual stress and strain hardening at the surface can improve the fatigue resistance [3-4]. CRS which can enhance the fatigue life of the product increases the stability of the product's geometry and the corrosion resistance [5].

The performance of materials can be improved markedly by the intelligent use of residual stress. For materials which can plastically deform, the residual and applied stresses can only be added simultaneously until the yield strength is achieved. In this respect, residual stresses may accelerate or delay the onset of plastic deformation. However, its effect on static ductile failure is trivial due to the small misfit strains that are soon removed by plasticity. Residual stress can raise or lower the mean stress experienced over a fatigue cycle. Free surfaces are often a preferred site for the initiation of a fatigue crack, which means that considerable advantage can be gained by engineering compressive in-plane stress near the surface region. The greatest benefits are experienced in low amplitude high cycle fatigue, while the gain is least in large strain-controlled low cycle fatigue. The variation exists because, in the latter case, initiation is caused by local alternating strains that exceed the yield stress. These plastic strains will soon relax or smooth prior residual stresses.

Residual stress can be measured using destructive and non-destructive techniques. Examples of destructive methods are curvature, crack compliance and hole-drilling. While the available non-destructive methods include magnetic, ultrasonic and diffraction [6].

The main behaviour of residual stress is that it could be reduced due to applied mechanical or thermal loading. This phenomena is known as residual stress relaxation and it is caused by the stress distribution due to the superposition of the stress. For example, compressive residual stress is opposed by external stress in tensile direction. As a result, the remaining value of residual stress is reduced.

This study focuses on the ASTM A516 grade 70 steel which is an excellent choice to fabricate pressure vessels and boilers because of its high tensile strength and its behaviour under high temperature. Previous research did not focus on the residual stress relaxation of this material. Since the application of ASTM A516 grade 70 steel is wide in various industries [7], it is a good idea to focus this study on this material.

Modelling of residual stress relaxation has been done by few researchers in the pass. This study focuses on the residual stress relaxation for this particular material by applying cyclic loads. Both experiment and simulation were conducted and through these methods, empirical model of residual stress relaxation incorporating a new parameter (surface hardness) of this material is developed. The empirical model is then validated by simulation using finite element (FE) method.

1.2 Problem statement

Fatigue life can be enhanced through mechanical surface treatments such as shot peening. Shot peening process is proven to improve the fatigue life of metallic components up to 50% [8]. The improvement is contributed by the amount of CRS induced during the shot peening process which is controlled by parameters namely shot size, shot angle and shot velocity. The peening coverage and intensity of the process are affected by the control of these parameters. However, due to the relaxation of CRS, the outstanding benefits of the shot peening treatments become uncertain under cyclic load conditions. In this case, a detrimental effect on the fatigue life can be expected, particularly in shot peened materials because their fatigue life depends significantly on the stability of induced CRS [8]. The external load could superpose the residual stress in the opposite direction causing the initial value of residual stress to reduce. This phenomenon is called residual stress relaxation.

Currently, there are many models which could be utilised to estimate residual stress relaxation [9]. The existing models focus on the thermal influence and mechanical cyclic loads governing the residual stress relaxation but did not incorporate surface hardness, the number of cycles and ASTM low carbon steel. A thorough literature review indicated that none of the existing models quantifies the cyclic residual stress relaxation by incorporating the initial residual stress, surface hardness and the number of cycles. It is important to find a method to calculate the remaining residual stress at any stage of component life by non-destructive or semi-non-destructive tests such as surface hardness.

1.3 Research objectives

The aim of this study is to develop an empirical model of residual stress relaxation of shot-peened ASTM A516 grade 70 carbon steel incorporating the surface hardness parameter and a numerical model of residual stress relaxation.

The specific objectives of this study are:

1. To investigate the change in mechanical properties and microstructure of ASTM A516 grade 70 carbon steel after shot peening process,
2. To determine the magnitude of residual stress on the ASTM A516 grade 70 steel introduced by shot peening process,
3. To characterize the relaxation of residual stress of the shot-peened ASTM A516 grade 70 steel after cyclic load is applied by experimental and simulation, and
4. To measure the surface roughness developed by shot peening process on ASTM A516 grade 70 steel.

1.4 Scope and limitation of study

The scope of the study involves both experimental and simulation analyses to investigate the relaxation of residual stress. The experimental method which was used to induce the initial CRS was shot peening. The simulation method used, on the other hand, was a finite element method (FEM) using Altair HyperWorks software.

The limitations and justifications of this study include:

1. The residual stress measurement was conducted on the surface as the samples were re-used for the measurement for hardness and microstructure test. This is a non-destructive test (NDT) measurement.
2. Due to the wide range of shot peening parameters, the introduction of residual stress is limited to shot peening intensity alone where it was differentiated by different shot sizes. Other parameters such as peening angle, velocity and shot size were not controlled in this research.
3. The number of cycles for cyclic loads was set at 1, 10, 100, 1000 and 10000 due to the high cost of X-Ray Diffraction measurement.

1.5 Thesis organisation

Chapter one is the introduction of the thesis. This chapter includes the study background, problem statement, research objectives as well as scope and limitation of the study.

Chapter two is the literature review. This chapter focuses on the previous research or studies that were related to this study. The topic covered in this chapter includes the material properties used in this study which is ASTM A516 grade 70 carbon steel, shot peening process which includes the mechanism and parameters of the process. Furthermore, this chapter also covers the simulation of shot peening including the software to be used for the simulation activity. Last but not least, the residual stress topic which includes the methods of introducing the stress, the effect of the stress on fatigue properties, methods of measurement and the relaxation of residual stress.

Chapter three is the methodology. This chapter discusses in details on the methods used during this study which were divided into two parts, simulation and experimental. Simulation part discusses on methods of performing the shot peening simulation and residual stress relaxation simulation using HyperWorks finite element software. Experimental part discusses mainly on the mechanical tests performed on ASTM A516 grade 70 steel before and after shot peening process. The mechanical tests performed includes tensile test, hardness test, fatigue test and other test is scanning electron microscope (SEM), performing cyclic loading with low and high amplitude as well as the measurement of initial residual stress introduced by different shot peening intensities and residual stress values after cyclic loads were applied. Additionally, surface roughness test also is performed on the material.

Chapter four is results and discussion. This chapter discusses on the result for all mentioned activity and tests performed on ASTM A516 grade 70 steel which also were divided into simulation and experimental. The results include the simulation result of shot peening and residual stress relaxation. At the end of simulation part, numerical model of residual stress relaxation was developed based on the result obtained from simulation. The experimental results include the tensile test, hardness test, fatigue test, microscopy test (SEM), surface roughness test, initial residual stress values introduced by different shot peening intensities and the values of the residual stress after cyclic loads (low and high) were applied. The values obtained from the residual stress measurement after different number of cycles were used to develop empirical model which is also discussed in this chapter. Finally, this chapter also covers on the validation of simulation result.

Chapter five is the conclusion and recommendations for future work. This chapter answers the five objectives that were proposed in this study. Moreover, recommendations for future studies related to this topic were also proposed in this chapter.

CHAPTER 2

LITERATURE REVIEW

2.1 Introduction

This chapter focuses on prior studies mainly to decipher the fundamental of the topic, to analyse the methodology used, and to note previous acknowledgements. Furthermore, research gaps are discussed in this chapter. This chapter starts with discussion of detailed information regarding the selected materials for this research, which is ASTM A516 Grade 70 steel. The information includes chemical properties, mechanical properties, and applications of this material in industries. The next section elaborates the shot peening process, which refers to the metal surface treatment applied in this study. It focuses on the mechanism of the process itself and the effect of this process on the material properties. Shot peening simulation using Finite Element Method (FEM) is discussed thoroughly to address several common methods applied for simulation.

The following section is related to residual stress introduced by surface treatment. It explains the definition, the methods to induce stress, the effect of this stress on fatigue properties of material, the methods of measurement. Lastly, the main topic, which refers to the modelling of residual stress relaxation, is presented. Since residual stress relaxes or reduces its value during operation due to applied external loads, many researchers have proposed various models in light of cutting-edge trend. In fact, empirical and numerical models have been developed in prior studies. The idea is to determine the gap in these models, while the next chapter of this study presents the proposed model with new contributions to knowledge and novelty.

2.2 Material ASTM A516 grade 70 carbon steel

ASTM A516 grade 70 is reckoned as pressure vessel material. This material is normally used in oil & gas and petrochemical industries due to its exceptional performance under low temperature and high tensile strength [10].

Table 2.1 lists the chemical composition of this material. One may observe the low percentage of carbon, when compared to other elements contained in this material. Nevertheless, this composition may vary with plate thickness. This material consist of 98.315% iron. Manganese varies between 0.85 to 1.2% and silicon varies between 0.15 to 0.4%. The rest of the material consist of 0.035% phosphorous, 0.05% sulphur and most importantly 0.31% carbon which influence the hardness of the material.

Table 2.1 Chemical composition of ASTM A516 Grade 70 Carbon Steel [10].

Component element properties	Percentage
Carbon, C	0.31%
Iron, Fe	98.315%
Manganese, Mn	0.85 – 1.2%
Phosphorous, P	0.035%
Silicon, Si	0.15 – 0.4%
Sulphur, S	0.04%

Table 2.2 tabulates the detailed material properties of ASTM A516 Grade 70 steel. The properties are divided into three categories which are mechanical, electrical and thermal. Due to its high tensile strength, this material has become the preferred selection in a range of industrial applications.

Table 2.2 Physical, mechanical, electrical and thermal properties of ASTM A516 Grade 70 steel [10].

Properties		Value	Unit
Physical	Density	7.80	g/cc
Mechanical	Ultimate tensile strength	485 – 620	MPa
	Yield strength	260	MPa
	Elongation at break	17 - 21	%
	Modulus of elasticity	200	GPa
	Bulk modulus	160	GPa
	Poissons ratio	0.29	-
	Shear modulus	80.0	GPa
Electrical	Electrical resistivity	0.0000170	Ohm-cm
Thermal	CTE, linear	120	$\mu\text{m}/\text{m}^{\circ}\text{C}$
	Specific heat capacity	0.470	$\text{J}/\text{g}^{\circ}\text{C}$
	Thermal conductivity	52.0	$\text{W}/\text{m}\text{-K}$

This material is usually used to make pressure vessels and boilers. The material offers exceptional mechanical properties in tough condition, especially the aspect of corrosion resistance [11].

2.3 Material properties

Material properties are the main reference to differentiate material grades. The methods of testing adhere to several standards, such as ASTM and ISO. The standards are specific to the type of material. This research adhered to standards for metallic material, as the material has low carbon steel.

2.3.1 Tensile properties

Tensile tests determine how materials behave under tension load. In a simple tensile test, a sample is typically pulled to its breaking point in order to determine the ultimate tensile strength of the material. A material property that is widely used and recognised is the strength of a material. Tensile testing is imperative to ensure safe and high quality material, apart from avoiding the major liabilities linked with non-compliant products. ASTM E8 “Standard Test Methods for Tension Testing of Metallic Materials” is used for tensile test [12].

2.3.2 Hardness properties

Some available hardness tests refer to Rockwell, Vickers and Brinell, which adhere to their own specific ASTM standards. Subtopics 2.3.2.1 to 2.3.2.3 discuss about the type of hardness test. Rockwell hardness is performed on the samples based on ASTM E-18 “Standard Test Methods for Rockwell Hardness of Metallic Materials”. It is a rapid method developed from production control, with direct readout, and mainly used for metallic materials. The scales used in Rockwell hardness test can be differentiated based on indenter size and total test force in kgf [13].

The Vickers hardness test method, also referred to as a microhardness test method, is mostly used for small parts, thin sections, or case depth work. The Vickers method is based on an optical measurement system. The microhardness test procedure, ASTM E-384, specifies a range of light loads using a diamond indenter to make an indentation which is measured and converted to a hardness value. It is very useful for testing on a wide type of materials, but test samples must be highly polished to enable measuring the size of the impressions. A square base pyramid shaped diamond is used for testing in the Vickers scale. Typically loads are very light, ranging from 10gm to 1kgf, although "Macro" Vickers loads can range up to 30 kg or more [14].

The Brinell hardness test method as used to determine Brinell hardness, is defined in ASTM E10 [15]. Most commonly it is used to test materials that have a structure that is too coarse or that have a surface that is too rough to be tested using another test method, e.g., castings and forgings. Brinell testing often use a very high test load (3000 kgf) and

a 10 mm diameter indenter so that the resulting indentation averages out most surface and sub-surface inconsistencies.

2.3.2.1 Issues of hardness properties related to shot peening

Yang et al. (2018) studied the fretting wear behaviour of Ti-6Al-4V using experimental method. This study compared the effect of different surface asperities and surface hardness induced by shot peening. Morphological analysis was conducted on the samples to compare the cracking phenomena caused by fretting wear for samples without shot peening and after shot peening process. It was found that shot peening process with a moderate intensity increases the wear volume during early fretting period, while reducing material loss in the long-term fretting wear process. This moderate intensity produced a good combination between hardness and toughness of the surface material [16].

Another studied conducted by Fu et al. (2018) was to find the relationship between hardness and residual stress for GCr15 steel after shot peening process. The hardness was found to increase due to the change in micro-structure (finer micro-structure) after shot peening process and increase the compressive residual stress which was also agreed by Ramkumar et al. (2017) in the previous study [17-18]. The methods of CRS measurement was X-Ray Diffraction and the researcher managed to find a new type of non-contact and non-destructive hardness testing using XRD.

2.3.3 Fatigue properties

Fatigue test on metallic alloy is according to ASTM E466. The method is applying constant load amplitude, typically load controlled in fully reversed where the ratio of maximum load to minimum load is -1 ($R = -1$). However, the load direction could be changed to tension – tension or tension – compression depending on the requirement of the test. For high cyclic test, the frequency is kept between 20 to 30 Hz because there will be less damage per cycle. Higher frequency can cause the temperature of the specimen to increase, hence higher possibility to become damage. According to the standard, the temperature increment of the specimen should not exceed 2°C [19 – 20].

2.3.4 Surface roughness properties

This test method describes a shop or field procedure for determination of roughness characteristics of surfaces prepared for painting by abrasive blasting. The procedure uses a portable skidded or non-skidded stylus profile tracing instrument. The usual measured characteristics are maximum height of the profile, R_t and maximum profile peak height, R_p [21].

2.3.4.1 Issues of surface roughness properties related to shot peening

Zhu et al. (2017) studied the influence of process parameters of ultrasonic shot peening on surface roughness on pure titanium. Experimental work was done by changing parameters like the peening duration, shot diameter, sonotrode amplitude and peening distance. Higher impact of shot peening cause higher dislocation and higher hardness. The result found there is a relation between microhardness and surface roughness where the trend of changing in surface roughness followed the trend of the change in microhardness. The change is quite drastic in the early stage of peening duration and both became more stable (saturated) after longer peening duration [22]. The surface roughness becomes rougher due to shot peening process and it was also agreed by Liu et al. (2017) and Kumar et. al (2019) [23– 24].

2.3.5 Morphological characterisation

The scanning electron microscope is mainly used to observe the topography of the cells in the samples over a large range of magnification. Sample preparation for SEM is simple. It is adaptable to various samples and does not require producing ultra-thin slices. SEM is already a routine method in medical research and is especially crucial for studies on the morphologies and interactions of oral bacteria.

SEM can be used to analyze and interpret observations on a micron or nanometer scale. The resolution of a field emission scanning electron microscope can reach as low as 1 nm. Another important feature of the scanning electron microscope is that it can be used to observe and analyze samples three-dimensionally due to its deep depth of field. The greater the depth of field, the more sample information is provided. In microbial

identification, SEM is utilized to observe and detect surface morphology and structural characteristics of microbial cells.

The scanning electron microscope is used to scan sample areas or microvolumes with a fine focused beam of electrons, producing various signals including secondary electrons, back-scattered electrons, Auger electrons, characteristic X-rays, and photons carrying different levels of energy. When the electron beam scans the sample surface, the signals will change according to the surface topography. The limited emission of secondary electrons within the volume close to the electron focusing area results in high image resolution. The three-dimensional appearance of images comes from the deep depth of field and shadow effect of secondary electron contrast [25].

2.4 Shot peening process

Shot peening is a worldwide surface treatment process applied on various parts in a range of industries to improve the mechanical properties of materials and fatigue life. This process is a cold work process that retards crack initiation and propagation by inducing compressive residual stress below the surface of materials.

The mechanism of shot peening is performed by applying multiple shots made by hard particles at high velocity onto the surface [26-28].

The main parameters of this process are shot size, shot angle, and shot speed. Shot peening is measured by its intensity using Almen strip. The following stages [29-30] depict the mechanism required in the shot peening process that changes the microstructure and the properties of the peened layer.

- i. The surface of a metallic component is hit by using a spherical particle called “shot”, made of iron, ceramic beads, glass, cast high-carbon steel, or stainless steel [31-32]. The dominant regime, which is fully plastic, can be indented by the impinging velocities that may hit up to about $12\text{-}150\text{ m}\cdot\text{s}^{-1}$ [35]. Figure 2.3 schematically illustrates this stage. Upon passing through the nozzle (from points A to B on the left side of Figure 2.1), the particles are accelerated by compressed air (or centrifugal forces) (right side of Figure 2.1) [33-34]. Point C displays the

point where the particles highly loaded with kinetic energy from point B was projected. A narrow cone surrounded by an area, which is destroyed at the surface, describes the pattern of shot blast. Stream energy is directly proportional to impact severity. The shot-derived kinetic energy is transferred to the surface during impact with the target, and the shot is returned in the rebound stage, hence the varied target and shot contact pressures with exposure time.

- ii. Some studies revealed equivalence to quasi-static behaviour [36-37] despite dynamic conditions. Numerical assessment using FEM [38] for shot velocities can reach up to 200 m/s at impact. The influence of time dependency is neglected, while the process is modelled with quasi-static approach. Nevertheless, major errors may occur due to the 300 m/s impact during the quasi-static analysis. Some anomalies could be due to: a) formation of shear-band and micro-cracking (effects of non-continuum), as well as b) interactions, strain-rate sensitivity, and elastic-weave (effects of time dependency).
- iii. In order to dissipate kinetic energy from the particle that leads to dimple formation, a finite plastic deformation takes place in the stressed material beneath the particle. The material surface must be yielded in tension to generate dent. Upon energy transformation, momentary rise is noted in temperature that has an impact on flow of plastic for surface of fibres. Heat from rapidly deformed material causes non-diffusing slip localisation called adiabatic shear bands [39]. Restoring surface shape after shot rebounds is impossible due to material continuity in plastic and elastic parts, thus capturing residual stresses in the component. Recovery is only for certain elastic properties of the plastically-deformed area. Figures 2.3a and 2.3b portray the trapped stresses with tensile residual stresses compressed in a thin sub-surface layer dispersed across lower areas. The shot-driven kinetic energy is absorbed by the component upon impact; causing plastic deformation at every impact point on the component surface (see Figure 2.3a), while Figure 2.3b illustrates rebound shot and trapped residual stresses. High impact stresses are caused by rapidly moving or increased dislocation density due to initial impacts.

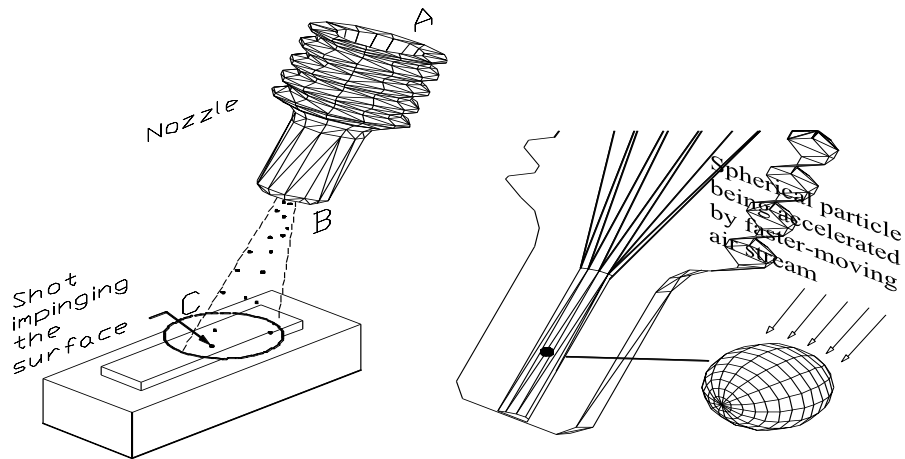


Figure 2.1 Schematic representation of the SP process [35].

- iv. Figure 2.2 presents the permanent global deformation on the uniformly deformed surface layers. The uniform plastic deformation occurs when all surfaces are indented due to peening exceeding its schedule [40]. Figure 2.4 shows the schematic diagram of low coverage of shot peening. The impact of shot on the left caused six dimples, while the dents of plastically deformed layer upon attaining 100% coverage formed a uniform and compressive residual stress layer beneath the surface. Frost and Ashby [41] explained the mechanism of increased fast moving dislocation density. Higher dislocation density lowers mean dislocation velocities that causes lower impact stresses upon saturation of the material.

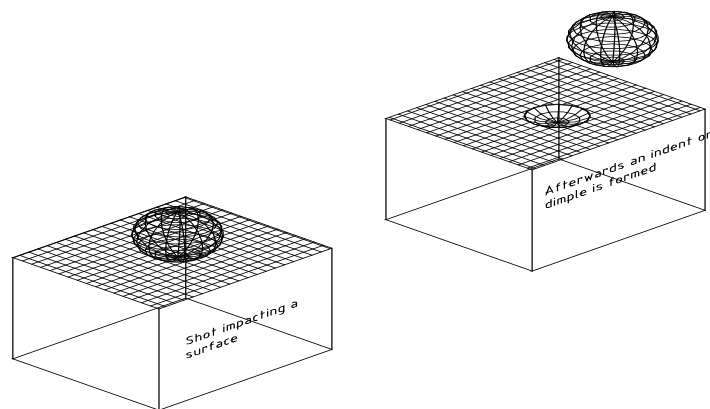


Figure 2.2 Schematic illustration of a shot immediately before and after impinging the surface [39].

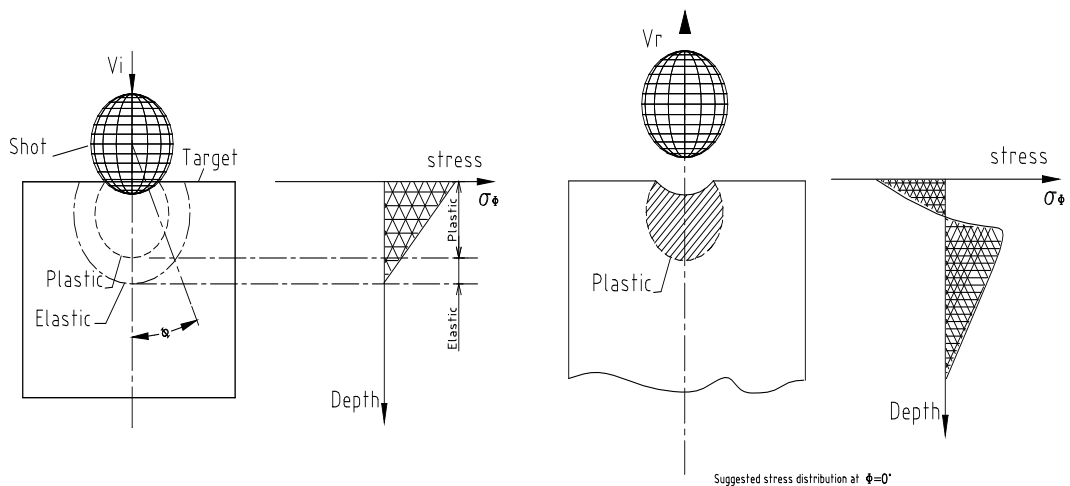


Figure 2.3 The mechanics: (a) a shot impacts a component, (b) on the rebound of the shot [39].

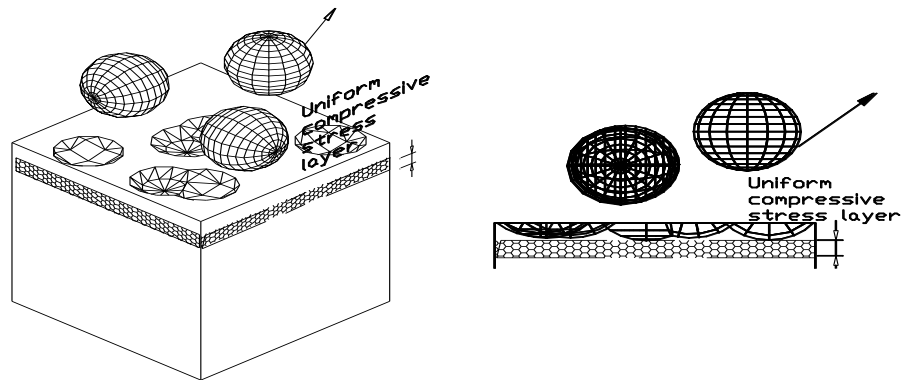


Figure 2.4 Schematic diagram of: low coverage [40].

2.4.1 Almen Strip

Almen strip refers to a rectangular sheet metal (SAE1070) used to measure shot peening intensity. This method of measurement was introduced by J.O Almen, an engineer at General Motors Corporation in 1940. In the procedure, the sheet metal is clamped to a test block and blasted with shots. After the blasting process, the sheet metal is removed and its deflection is measured using an Almen gauge. This arc height determines the intensity level of the shots. The higher height represents higher intensity, thus more compressive residual stress is stored on the surface of material.

Almen strips are composed of N, A, and C types, which are differentiated by their thickness. The dimension of these Almen strips is 3.0” (76.2 mm) long and 0.75”

(19.05 mm) wide. These types are differentiated by their thickness [42]. The thickness of all types are:

- Type 'N' – 0.031" (0.7874 mm) – for low intensity
- Type 'A' – 0.051" (1.2954 mm) – for average intensity
- Type 'C' – 0.0938" (2.3825 mm) – for high intensity

Figure 2.5 illustrates the method of measuring Almen strip. This test is conducted by applying the shots of Almen strip placed on a steel block.

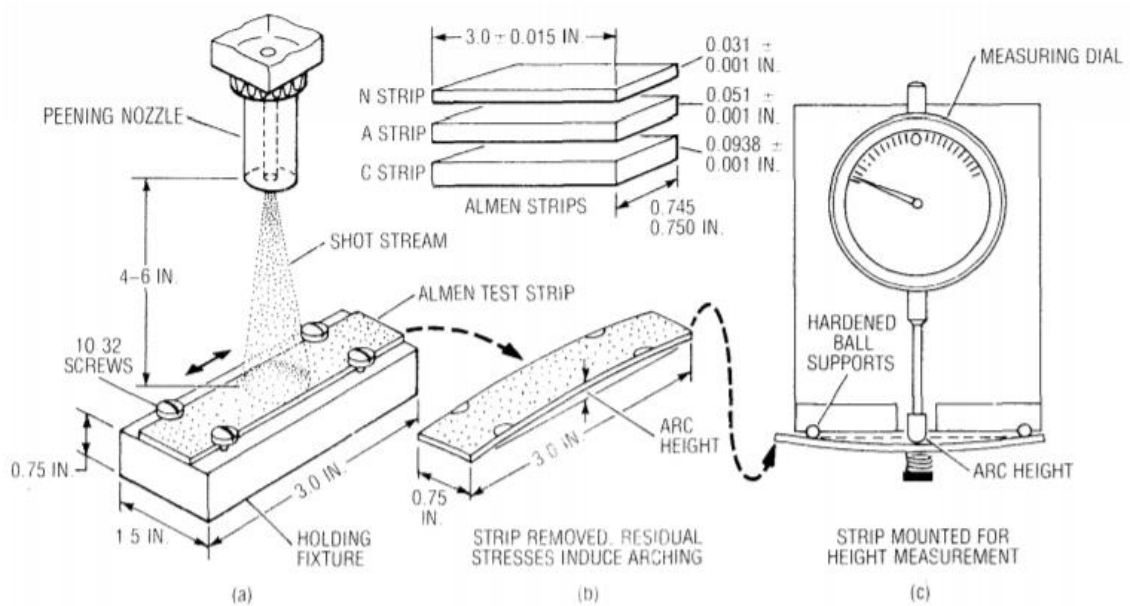


Figure 2.5 Shot stream applied on Almen strip for the intensity measurement [43].

The Almen arc height A_h of each strip is plotted as a function of its exposure time t to obtain the saturation curve. Figure 2.6 shows the Almen saturation curve as a function of exposure time. Shot peening saturation is defined as the point at which doubling the exposure time results in 10% or less increase or less increase in curvature arc height. It is assumed that the curvature of the Almen strip will indicate the rate of compressive stress that leads to a resistance to fatigue failure.

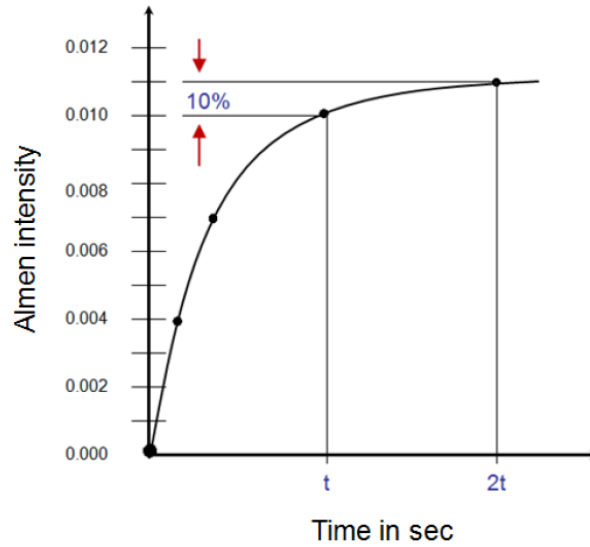


Figure 2.6 Almen saturation curve against exposure time [44].

2.4.2 Shot size

Shot size is the most important property in the shot peening process. Shot size affects saturation intensity, coverage rate, and depth of work-hardened layer. A range of shot sizes can be applied for this process, which depends on the requirement of products. The size differentiates the impact that contributes to the value of residual stress. Bigger shot size generates higher impact and residual stress value. Table 2.3 shows the cast shot numbers with the sizes and screening tolerances. Minimum shot size usually used in industry is 0.1778 mm in diameter and the maximum is 3.3528 mm in diameter.

Table 2.3 Cast shot numbers and screening tolerances [45].

Shot code	Diameter		Mass	Particles
	inch	mm	mg	Per 100g
S70	0.0070	0.1778	0.02313	4,322,983
S110	0.0110	0.2794	0.08976	1,114,037
S170	0.0170	0.4318	0.33134	301,808
S230	0.0230	0.5842	0.82055	121,869
S280	0.0280	0.7112	1.48046	67,547
S330	0.0330	0.8382	2.42362	41,261
S390	0.0390	0.9906	4.00052	24,997
S460	0.0460	1.1684	6.56441	15,234
S550	0.0550	1.3910	11.22045	8,912
S660	0.0660	1.6764	19.38894	5,158
S780	0.0780	1.9812	32.00414	3,125
S930	0.0930	2.3622	54.24643	1,843
S1110	0.1110	2.8194	92.23404	1,804
S1320	0.1320	3.3528	155.11154	645

Specifications, such as SAE J444 and AMS 2431, nominate cast steel shot size in terms of sieving outcomes, thus nominal shot sizes are based on sieve mesh spacing. Cast steel shot size can be associated with the diameter of a sphere. This is convenient because (a) cast steel shot particles are approximately spherical, and (b) a sphere is the only geometrical figure that has only one dimension. Association of a particle size with sphere diameter is based on the concept of “equivalent sphere”. The “equivalent sphere” of an individual shot particle is one that has the same volume as that of the particle (and hence, the same mass).

2.4.3 Shot angle

Shot angle affects the quality of shot peening in terms of surface morphology, surface hardness, and surface roughness [45]. Fuhr et al. (2018) investigated the effect of changing peening angle from 90° to 30° to the peening coverage experimentally. It was found that the coverage varied to a wide extent ranging from 20% to 1200%. Low coverage leads to a loss in the strength of a targeted material, therefore higher coverage is very much important criteria of shot peening [46]. Kim et al. (2013) on the hand investigated the effect of changing the angle using finite element model. The model proposed could be used for various incidence peening angle for multi-shots simulation [47].

2.4.4 Shot velocity

Based on the theory of momentum, higher velocity produces higher impact, hence higher residual stress can be stored under the surface of contact plane. Many have discussed the influence of shot peening speed. Gariépy et al. (2017) performed an experiment by setting three shot velocities at 34.6 m/s, 53.7 m/s, and 66.2 m/s to study peening saturation on L- and T-type aluminium test strips, as well as A-type Almen strips [48]. The results are tabulated in Table 2.4. It is observed that higher velocity increases arc height and decreases saturation time. The velocity of the shot ball is a crucial factor for residual stress distribution mentioned by Xie et al. (2016) [49].

Table 2.4 Result of saturation study on L-type aluminium test strips, T-type aluminium test strips and A-type Almen strips [49].

Shot velocity (m/s)	Saturation time			Arc height at saturation (mm)		
	L	T	Almen	L	T	Almen
34.6	9.466	9.919	23.219	0.224	0.209	0.127
53.7	6.846	6.673	12.178	0.321	0.308	0.189
66.2	5.886	6.119	8.304	0.387	0.376	0.220

2.4.5 Effect of shot peening on material

It is obvious that any treatment experienced by the materials would change their properties, such as mechanical, thermal, and electrical. Many researchers have assessed the effect of shot peening process on material properties. The main concern of product performance is operation duration prior to failure. In this case, the scale of measurement is fatigue life. Shot peening increases fatigue life by slowing the propagation of microcracks caused by applied loads while operation.

For instance, Maleki et al. (2018) estimated the fatigue behaviour of shot peened mould carbon steels by applying a novel alternative approach that adhered to the concept of artificial neural network. The outcomes showed that surface coverage is more important than higher intensity of shot peening to enhance fatigue life [48]. Compressive residual stress is required to increase fatigue life if external load is applied in tensile direction. On the contrary, tensile residual stress is required if external load is applied in compressive direction.

Upon focusing on micro-shot peening process, Zhang et. al (2019) asserted that the process can improve the fatigue properties of alloy in air and in salt atmosphere. He concluded the following [49]:

1. Compressive residual stress field and hardening layer were formed on specimen surface after micro-shot peening.
2. The S-N curve of micro-shot peened specimens in salt atmosphere showed continuous decrease with the increasing number of loading cycles, while that in air shows a step-wise shape. The fatigue strength of peened specimens at 10^7 cycles was increased by 47% and 67% in air and in salt atmospheres, respectively.
3. All the specimens failed from surface, except for the micro-shot peened specimens tested in air, which failed from subsurface zone in high cycle fatigue region. The micro-shot peening cannot change the fracture mode. The specimens in air showed shear mode fracture, while those in salt atmosphere exhibited normal mode fracture.

4. Micro-shot peening can delay both crack initiation and its early propagation, thus improving fatigue strength.

Apart from fatigue behaviour, electrochemical behaviour of a material may also be changed during the shot peening process. Aslan et al. (2019) investigated low-alloy steel to test this said behaviour via corrosion test at room temperature in 3.5% NaCl solution on several intensities of shot-peened sample. The samples were shot-peened with intensities of 16 A, 18 A, 20 A, and 24 A. As a result, the corrosion resistance of the material increased with the increasing shot peening intensity, owing to grain refinement and formation of sub-grains [50]. Liu et al. (2019) also discussed the effect of shot peening on corrosion behaviour. The materials assessed by the researcher were AZ31 and AZ91 magnesium alloys. This study slightly contradicts with Kovaci and Bozkurt, since Kovaci found increased corrosion resistance due to shot peening, while Liu et al. discovered that the shot peening only improved the corrosion resistance of AZ31, but not on AZ91 [51].

Otsuka et al. (2018), studied the effect of shot peening on permeation and retention attributes of hydrogen in alpha iron. It was found that the permeation of a shot-peened iron was reduced by a factor of ten, in comparison to unpeened iron. Permeation leakage is a major concern in several industrial parts, such as vessels, containers, and coolant pipes, especially those made of steel [52].

The thermal behaviour of a material can also be enhanced via shot peening process. Poongavanam et al. (2019), studied the effect of shot peening on heat transfer performance of a tubular heat exchanger. The process improved the performance of heat exchanging, as determined by the increased Nusselt number, friction factor, and figure of merit, which were applied to characterise the performance of tubular heat exchanger [53].

Shot peening has also been proven to reduce friction between mechanical components. Hoffman et al. carried out simultaneous shot peening (SSP) of hard and soft particles in reciprocal sliding to study if this process minimised friction. Reduction of friction is crucial to reduce energy consumption. The researcher tested 25 combinations of normal load and sliding speed during the experiment. As a result, it was revealed that SSP could reduce the average friction by 33% [54].

2.5 Shot peening simulation

There are many articles which discuss on the shot peening simulation using Finite Element Method (FEM). Most of the papers discuss on the effect of changing the shot peening parameters such as the shot size, shot velocity and shot angle.

2.5.1 Single shot simulation

According to Kubler et al. (2019), shot peening simulation can be performed with single shot and multiple shots [55]. Single shot simulation is done to study the value of residual stress induced during the impact between the shot and the surface. On the other hand multiple shots is done to study the coverage as well as the change in the surface roughness due to shot peening process.

The single shot simulation is also known as initial impact damage analysis model. Figure 2.7 illustrates the geometry setup of the model with varied angles of impact.

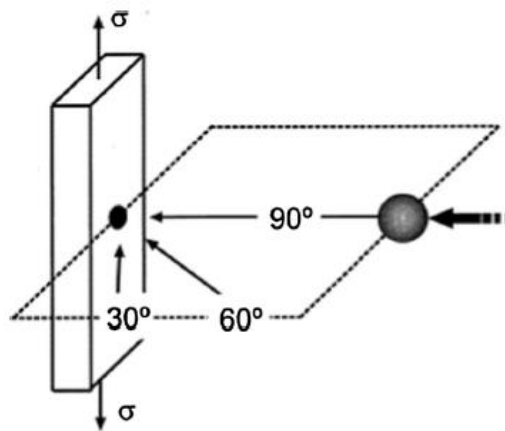


Figure 2.7 A schematic illustration of impact angle [55].

For shot peening using single shot method, the theory behind the calculation of the impact radius is based on Hertz theory [56]. Figure 2.8 presents the geometry of a sphere in normal contact or perpendicular to the plane.

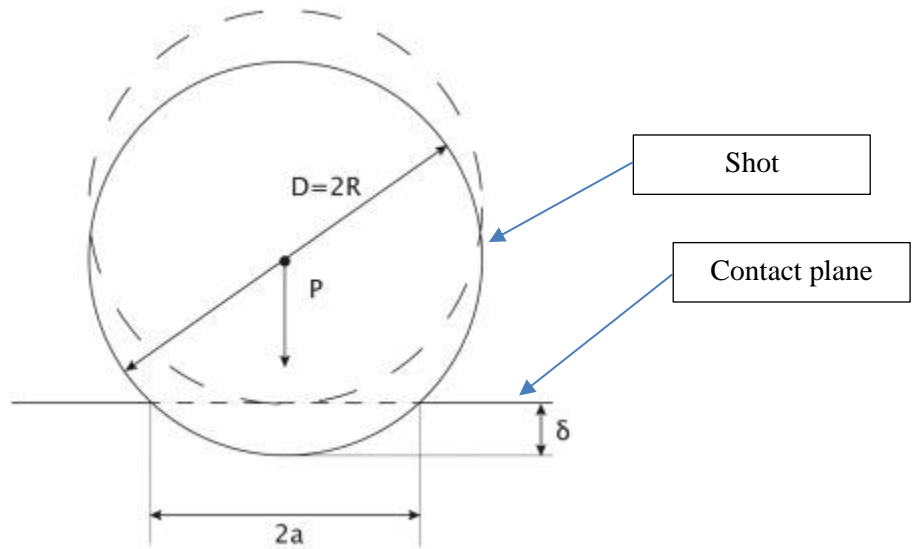


Figure 2.8 Geometry of a sphere in normal contact with a plane [56].

Equation 2.1 shows the total compression δ is related to the contact radius a by:

$$\delta = \frac{a^2}{D} \quad (2.1)$$

where δ is the total compression, a is contact radius and D is the shot diameter. In the Hertz theory, the load P , resulting from the pressure forces of the ball on the plate, is linked to δ by Equation 2.2:

$$P = \frac{4\bar{E}\sqrt{D}}{3\sqrt{2}} \delta^{3/2} \quad (2.2)$$

with \bar{E} is the equivalent Young modulus defined as a function of the elastic material properties of the shot (subscript s) and of the impacted plate (subscript p) as shown in Equation 2.3:

$$\bar{E}^{-1} = \frac{1 - \nu_s^2}{E_s} + \frac{1 - \nu_p^2}{E_p} \quad (2.3)$$

In order to obtain a relationship between the shot peening parameters and the resulting contact area of radius a , an equivalence between an elasto-plastic shock and an elastic

one is made. The kinetic energy W of a shot is converted to an elasto-plastic energy W_{ep} of the impacted material and a energy W_d dissipated in the form of temperature and oscillations such as Equation 2.4:

$$W = W_{ep} + W_d \quad (2.4)$$

The efficiency of the impact is characterized by the ratio K between the elasto-plastic energy and the total kinetic energy (Equation 2.5).

$$K = \frac{W_{ep}}{W} \quad (2.5)$$

The ratio K was estimated to be 0.8 by . The elasto-plastic energy is thus defined as Equation 2.6:

$$W = K \cdot \frac{1}{2} m V^2 = \frac{K \pi \rho_s D^3 V^2}{12} \quad (2.6)$$

where ρ_s is the density of the material of the shot, D its diameter and V its velocity. For a plastic impact at moderate velocities (up to 500m/s), impact velocities are small compared to elastic wave speeds. Thus the impact behaviour can be investigated under static conditions. The kinetic energy W is absorbed in local deformation of the two colliding bodies, up to the instant of maximum compression, which is expressed by Johnson (1985) as Equation 2.7:

$$W = \int_0^{\delta} P d\delta \quad (2.7)$$

where the resulting load P is linked to the average dynamic pressure p_d by Equation 2.8:

$$P = \pi a^2 p_d \quad (2.8)$$

By inserting Equation 2.1 and Equation 2.8 in Equation 2.7, the kinetic energy is expressed (Equation 2.9):

$$W = \int_0^a \pi a^2 p_d \frac{a}{R} da = \frac{\pi a^4 p_d}{4R} \quad (2.9)$$

By writing the equivalence between Equation 2.9 and Equation 2.6, the contact radius is linked to the shot peening parameters finally by Equation 2.10:

$$a = D \cdot \left(\frac{K \cdot \pi \rho V^2}{4\sqrt{2}\bar{E}} \right)^{1/5} \quad (2.10)$$

D = shot diameter

K = ratio of elasto-plastic energy to kinetic energy

P = density of the plate of impact

V = shot velocity

\bar{E} = equivalent Young modulus

Guiheux et al. studied the martensitic transformation induced by single shot peening in austenitic stainless steel. It was found that the transformation occurs due to plastic straining. In this work, the impact of a single spherical steel shot was used and the result was that the martensitic transformation takes place only under the dent and the martensite is in tension at the surface while austenite is in compression. The result was comparable with X-ray diffraction in the experimental work [57].

2.5.2 Multiple shot simulation

It was proposed by Zarka (1990) to predict the stabilized elastoplastic response of structure under a cyclic load using an analytical approach. This approach is used for residual stress profile prediction after shot peening and their evolution during a cyclic behaviour. The advantage of using this model is minimal computational cost for direct resolution. However, this model is not suitable for material with non-standard behaviour and can be used only for homogeneous surface treatment [58].

The effect of shot peening is also often modelled with multiple impacts simulation model using finite element (FE). Jianming et al. (2011), Murutganam et. al (2015), Tu et. al (2017), and Zhang et al. (2018) had used this approach to model coverage, roughness and residual stress profiles on a target material. The initial condition in their FE analysis are the positions and initial velocities of shots [59-62]. Similarly, Guagliano et al. (2001) proposed a model which linked the Almen intensity to residual stress profile prediction in a shot peened part for material 39NiCrMo3 and SAE 1070 steel. Based on the residual stress profile from simulation result of multiple impacts, the bending of Almen strip could be predicted [63]. Klemenz et al. (2009) also used multiple impacts model by simulating 121 rigid spheres (shots) to hit the surface of a target material. This material selected is AISI4140 steel and defined as elasto-viscoplastic model with a combined isotropic-kinematic behaviour. A comparison of surface topography and residual stress field with single and double impacts model was done [64]. To study the shot peening parameter effect such as the impact velocities and shot diameters, Gari'epy et al. (2017) has also used multiple impact model. Isotropi-kinematic hardening formulation is used and the formula is built into the Abaqus solver representing the cyclic hardening behaviour of AA2024-T351 alloy. It was found that residual stress distribution prediction with smaller computational cost could be achieved by reducing the number of impacts [65]. Meguid et al. (2002) investigated the effect of friction coefficient between the shot and the target material on the residual stress profiles. It was found that the coefficient of friction does not really make any changes to the residual stress profiles. Bagherifard et al. (2012) and Xiao et al. (2018) have both studied the effect of random impacts to obtain 100% coverage and impacting density I the residual stress profile using FE analysis [66 – 67].

Analytical and FE approaches were also presented by Gallitelli et al. (2016) to model residual stress fields after shot peening of a part with complex geometries. The process parameters were linked to the stress field which was obtained from the simulation analytically using a dimensional analysis [68]. Chaise et. al (2012) also did something similar with the study but the approach was based on calculation of inelastic stain field and it could predict the same field as FE models with much less computational cost [69].

Few more researchers use the same approach of multiple impacts shot peening simulation [70 – 82]. These researchers' main objective is to determine the residual stress profiles and to optimize the shot peening parameters to be implemented in industries.

In summary, shot peening is an integral process, especially on mechanical components. The process is widely implemented across various industries due to its benefits in terms of cost and ease of handling. The mechanism is simple, while the results are prominent and worthy. The parameters to be controlled during the process are shot size, incidence angle, velocity, intensity, saturation, and coverage. For these, intensity is likely to be the most used control parameter. The measurement method normally used by manufacturers is the Almen strip, where the arc height is used to determine the level of intensity. Shot peening improves the fatigue life of the material by changing its properties, such as tensile, hardness, surface roughness, and microstructure. Compressive residual stress is introduced by this process to superpose the external loads applied on the component during the operation. Shot peening simulation can be categorised into the following:

- (1) Expectedly uniform distribution of shots, in which the shots impinge the specified position on the peening surface in the specified order
- (2) Completely random distribution of shots, in which the shot impinge the completely random position on the peening surface

This study used the first method, which refers to the expectedly uniform distribution of shots. It is an ideal model with the advantage of low computation cost, wherein several representative models have been developed by Meguid et al., [83], Kim et al., [84], and Wang et al., [85], to name a few.

2.6 Simulation software

There are a few simulation software used worldwide such as ANSYS, Abaqus and HyperWorks. These software are very compatible for finite element analysis. Most of previous works for shot peening simulation was done using Abaqus especially for multiple impacts simulation [86 – 93]. There are also studies which used ANSYS as their simulation tool [94 – 100]. However, when the study involves the cyclic loading or fatigue life prediction, many researchers used Hyperworks as their simulation tool [101 – 105]. The advantage of using Hyperworks is it does not need complex coding since everything seems to be found on the interface.

2.6.1 Comparison of simulation software

The simulation software can be compared by their advantages and disadvantages. Mainly users would prefer a software with the most user friendly interface. Table 2.5 shows the summary of advantages and disadvantages of each software [106].

Table 2.5 Advantages and disadvantages of ANSYS, Abaqus and HyperWorks.

Software	ANSYS	Abaqus	HyperWorks
Advantages	<ol style="list-style-type: none"> 1. Wiring a macro is easy. 2. Very basic but one would understand in a better way what happens inside the software. 3. Same window for geometry handling and meshing. 	<ol style="list-style-type: none"> 1. The scripts can be written in Python and work in Abaqus as a Plugin. 2. Very basic but one would understand in a better way what happens inside the software 	<ol style="list-style-type: none"> 1. Best element level control compared to ANSYS and Abaqus. 2. One can use Hypermesh to mesh for different solvers like ANSYS and Abaqus.

Software	ANSYS	Abaqus	HyperWorks
		<p>3. Same window for geometry handling and meshing.</p> <p>4. Good element level control.</p> <p>5. Faster meshing.</p> <p>6. Easier contact treatment.</p>	
Disadvantages	<p>1. Not so accurate for multiple bodies simulation.</p> <p>2. User has to use Design Modeler for geometry handling and ANSYS Mechanical for meshing (different interface).</p> <p>3. Writing a macro is not that easy.</p> <p>4. Lesser element level control.</p>	<p>1. Not aware of units and user has to key in the units in a consistent manner.</p> <p>2. User interface hasn't changed much in all these years and looks really outdated.</p> <p>3. Writing a macro is not that easy.</p> <p>4. Lesser element level control.</p>	<p>1. Mesh controls are not stored.</p> <p>2. Geometry handling features are far superior in comparison with ANSYS and Abaqus.</p>

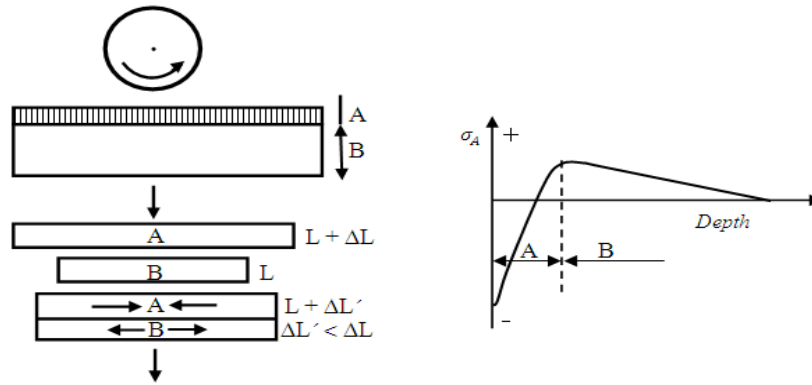
2.7 Residual stress

Every manufacturing process introduces residual stress into the mechanical parts. The residual stress can be in tension (positive) or in compression (negative) form. The stress influences fatigue behaviour. Hence, the role of residual stress is crucial in designing and producing mechanical parts. The stress that remains in mechanical parts and not subjected to external stresses is known as residual stress, which exists in all rigid materials, including metals, polymer, ceramic, wood, and glass. It is the result of metallurgical and mechanical history of each point in the part and the part as a whole during its manufacture. Depending on the scale of the stress, it can be divided into three levels [107, 108]:

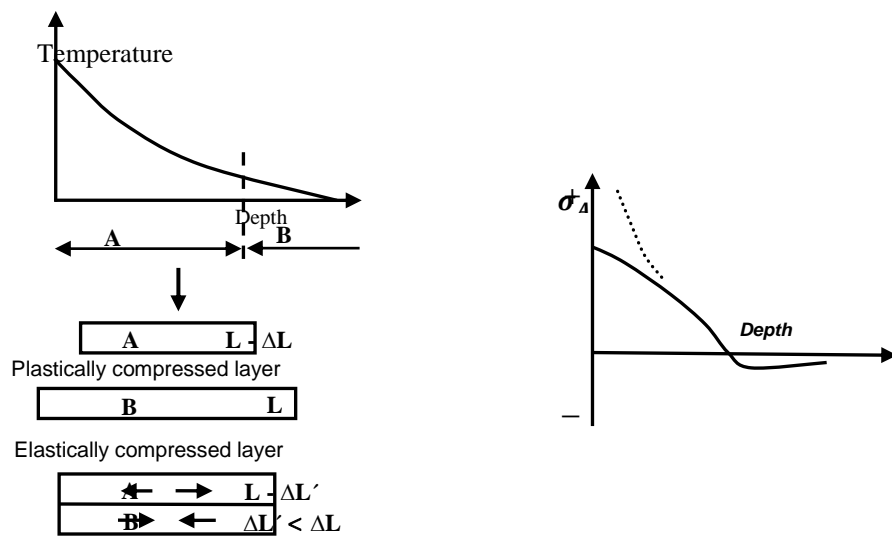
- The first level (macroscopic residual stress) affects the whole mechanical part or a large part of the grains.
- The second level (2nd level residual stress) refers to non-nil stresses caused by the presence of mechanical stress on grains with varied yield points, as resilience develops in adherence to the grains, mainly due to the heterogeneity and anisotropy aspects of each crystal or grain in polycrystalline material. Elimination of load results in heterogeneous attribute.
- The third level is on the on the crystal scale, which hits the limits of the stress due to varying crystalline defects, for instance, grain joints, stacking defects, substitute atoms, twin crystals, dislocations, and interstitial compounds.

2.7.1 Methods of introducing residual stress

Residual stress can be divided into mechanical, thermal, and metallurgical genres, wherein the combination of these factors generates residual stress for grinding. An instance of mechanism that creates residual stress in a particular case can be reflected in the complexity of the origin of residual stress [107] (see Figures 2.9a-2.9b).



(a)



(b)

Figure 2.9 (a) Residual stress produced by plastic deformation in the absence of heating; (b) Residual stress resulting from exceeding the elastic limit after the presence of a temperature gradient [107].

The following are some causes of macroscopic residual stress:

- non-homogeneous plastic flow under external treatment action (shot-peening, auto-fretting, roller burnishing, hammer peening, shock laser treatment)
- non-homogeneous plastic deformation while non-uniform heating or cooling (ordinary quenching, moulding of plastics)
- structural deformation from metalworking (heat treatment)
- heterogeneity of chemical or crystallographic order (nitriding or case hardening)

- varied surface treatments (enamelling, nickel-plating, chrome-plating)
- variation in expanded coefficients and mechanical incompatibility of differing composite components (composites with metallic-organic matrix, ceramic coatings)

Table 2.6 shows the origins of residual stress for metal working operations that are commonly carried out in the industry. In order to produce an industrial part, one or several techniques listed in the table may be applied. In order to calculate the residual stress that exists in a part, the stress source must be determined at the early stage.

Table 2.6 Main origins of residual stress from different manufacturing processes [108].

Process	Mechanical	Thermal	Structural
Smelting Casting	No	Temperature gradient during cooling	Change of phase
Shot-peening Hammer-peening Roller burnishing Bending Rolling Forging Straightening Extrusion	Heterogeneous plastic deformation between the core and surface of the part	No	No
Grinding Milling Drilling Boring	Plastic deformation due to the removal of chips	Temperature gradient due to heating during machining	Change of phase during machining if the temperature is sufficiently high
Quenching without a phase change	No	Temperature gradient	None

Process	Mechanical	Thermal	Structural
Surface quenching with a phase change	No	Temperature gradient	Change of volume due to a phase change
Welding	Flanging	Temperature gradient	Microstructural change (HAZ)
Brazing	Mechanical incompatibility	Thermal incompatibility	New phase at interface
Composite	Mechanical incompatibility	Mechanical incompatibility	No
Electroplating	Mechanical incompatibility	Mechanical incompatibility	Composition of plating depending on bath used

2.7.2 Residual stress effect on fatigue properties

The actual stress for the subjected part is determined by tensor $\sigma_R + \sigma_S$, in which elastic residual stress is characterised by tensor σ_R , and tensor σ_S defines the superposed field of service stresses. The part is bound to be overloaded locally due to addition of residual stress to service stress. Nevertheless, mechanical performance can be enhanced and the part can be relieved of load upon introduction of compressive residual stress at the finishing operation of shot-peening.

Use of residual stress, in a wise manner, may tremendously enhance material performance. Applied and residual stresses can be integrated in plastically deformable materials directly upon hitting yield strength. Plastic deformation onset may be delayed or accelerated by residual stress, despite minor failure in static ductile due to slight misfit strains, which are discarded via plasticity. Mean stress over a fatigue cycle can be increased or decreased with residual stress. Besides, Gerber/Goodman correlation can be applied to determine the impact on fatigue life (see Figure 2.10a). Upon increment in mean stress due to tensile residual stress, reduction of stress amplitude ascertains unaffected lifetime. Static fracture may be triggered by tensile residual stress at huge mean values. Fatigue crack initiation often prefers free surface. Compressive plane stress engineered near surface region offer a range of benefits. The least gains are noted in

strain-controlled low cycle fatigue, while the largest can be found in low amplitude high cycle fatigue. In the former case, local alternating strains that are beyond yield stress lead to crack initiation. Prior residual stresses are relaxed by the plastic strains. With the growth of fatigue crack, mean stress heavily affects high growth rate and near threshold, while being insensitive to Paris regime. Thus, the residual stresses would have minor impact on growth rates of crack in Paris regime, unless crack closure is initiated by mean stress change (see Figure 2.10b). Overall, stresses of types II and III can be washed out via plasticity around crack tip zone, hence the consideration of type I from the perspective of fatigue [109].

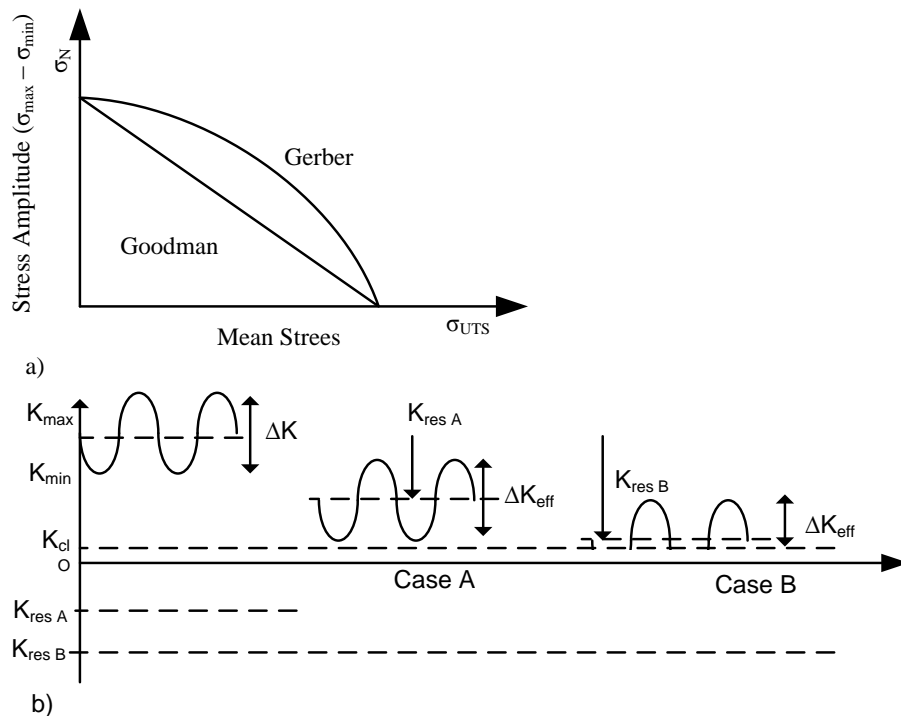


Figure 2.10 Effect of residual stress on fatigue lifetime (a) constant life plot for mean stress versus stress amplitude; (b) effective stress intensity range ΔK_{eff} for two compressive residual stress levels (A, B) with non-zero crack closure stress intensity factor K_{cl} [109].

To date, residual stress can be used to predict fatigue life in a quantitative manner. Fatigue is often the cause of failure in mechanical origin based on statistics. The empirical

outcomes displayed that the Goodman-type linear correlation can determine residual stress:

$$\sigma_a = \sigma_D - \frac{\sigma_D}{R_m} (\sigma_m + \sigma_R) \quad (2.11)$$

Where σ_a is amplitude of admissible stress, σ_m is mean fatigue stress, σ_D is purely reverse tensile fatigue limit, R_m is true rupture strength, σ_R is residual stress measured in the direction of the applied service stress.

2.7.3 Incorporating the concept of residual stress into the design

To date, only a handful of industrial sectors have considered the residual stress parameter directly. In technical specifications, requirements included are often closely related to residual stress without actually naming them.

Incorporating the concept of residual stress into the design must be gradual and can be divided up into several phases [109].

In the first phase of incorporation, one can use a semi-quantitative concept to evaluate the increase in performance in terms of fatigue life or fatigue strength. Table 2.7 presents an instance of the efficacy of shot-peening to enhance fatigue life in a range of mechanical parts [109].

Table 2.7 Increase in the fatigue life of various mechanical components as a result of shot-peening [109].

Component	Stress type	Fatigue life improvement (in %)
Spindles	Reverse bending	400 to 1 900
Shafts	Torsional	700
Gear box	Fatigue life tests in service	80
Crankshafts	Fatigue life tests in service	3000 but highly variable
Aircraft coupling rods	Tensile-compression	105
Driving rods	Tensile-compression	45
Cam springs	Dynamic stress	100 to 340
Helical springs	Fatigue life in service	3500
Torque rods	Dynamic stress	140 to 600
Universal joint shaft	Reverse bending	350
Gear wheel	Fatigue life tests	130
Tank chain	Fatigue life tests	1100
Weld	Fatigue life tests	200
Valve	Fatigue life tests	700
Rocker arm	Fatigue life tests	320

2.7.4 Residual stress measurement

The two techniques that determine residual stress are destructive and non-destructive methods. The destructive techniques that destroy samples until stress relief are hole drilling, compliance, and curvature, whereas ultrasonic, photo-/thermo-elastic, diffraction, and magnetic are instance of non-destructive methods that do not destroy the samples.

2.7.4.1 Curvature

Stresses within layers and coatings are commonly determined via curvature measurements. Layer deposition may lead to curved substrate due to induced stress [110] (see Figure 2.11). The stress variation due to deposit thickness may be calculated based on curvature changes that occur during deposition by using either indirect contact methods (video, laser scanning, grids, double crystal diffraction topology) or direct contact techniques (profilometry, strain gauges) [111], which permits routine characterisation of curvature by approximately 0.1 mm.

Narrow strips (≤ 0.2 width/length) are used for measuring purpose, especially to prevent mechanical instability and multi-axial curvature.

The Stoney [112] equation has been widely applied to associate stiffness E and deflection g of a thin beam of length l to stress, σ , along beam, and d is the thickness of primary shear plane as in equation 2.12:

$$\sigma = -\frac{Eh^2}{3l^2} \frac{dg}{dh} \quad (2.12)$$

where h refers to the current thickness.

This is commonly used for polymeric and metallic composites, as well as thin coatings derived from plasma, or physical vapour deposition [111], or chemical vapour deposition [113]. As it is impossible to discard additional layers, the in-plane stress levels may be estimated based on thickness distribution. However, ambiguity is present in this method due to insignificant stress distribution with curvature.

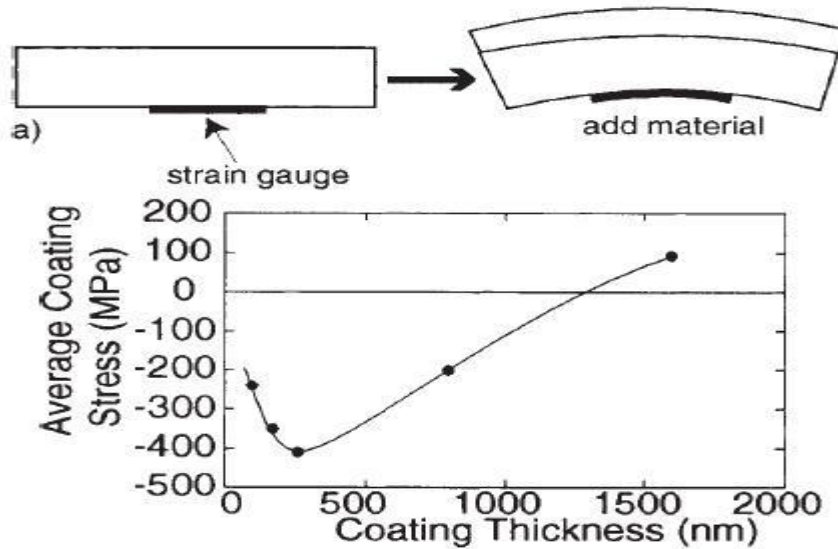


Figure 2.11 Basis of method for monitoring development of residual stresses during deposition, experimental data were obtained for various thicknesses of sputtered [110].

2.7.4.2 Crack compliance method

In the method of crack compliance, a small slot is cut to determine stress relief in crack with strain gauge interferometry. Increasing the depth of the slot will allow resolving the stress field normal to the crack as a function of depth for relatively simple stress distributions [114].

A number of removal approaches have been proposed. For instance, matrix etching and fibre length changes determine residual thermal stresses in the fibre stage of continuous fibre metal matrix composite. Apart from that, a section can be cut using an electro-discharge machine to infer prior normal stresses from planarity deviation [115].

2.7.4.3 Hole-drilling

Residual stress can be measured via hole-drilling method, wherein a hole is drilled into a sample that contains residual stresses. Measuring the surface strains relieved at hole boundary using residual stress strain gauge rosette permit one to back-calculate residual stress [116] by determining the changes in the strain gauge outcomes. Residual stress is determined via hole-drilling upon removing a material from a stressed surface, thus

allowing slight relaxation on the surface, and hence, relaxation of residual stresses as well. Uninterrupted areas with residual stress will relax into varied shape upon machining of locality, thus the generation of data to back-calculate residual stress [117].

As far as the hole drilling method is concerned, it is assumed that the samples are linear elastic, isotropic, and have small stress variation at hole boundary [118].

The benefits of the hole drilling technique are: portable equipment, applicable on huge components, cost-effective, rapid process, applicability across vast materials and surfaces (flat/curved) [119].

Numerous small wires are applied in measuring strain using a strain gauge. Upon modified length of wires when gauge is fixed onto a surface, wire resistance changes indicate change in surface strain. Gauges are arranged in circular around the hole for drilling. In fact, both hole and gauge circle should be concentric, which is determined via special alignment equipment. Accuracy of measurement is determined by exceptional installation and surface preparation [118].

As illustrated in Figure 2.16, the hole is drilled by using a tool, and later, the strain can be measured with laser interferometry based on rosette of indentations, holography, or a rosette of strain gauges. In general terms,

$$\sigma = (\sigma_{max} + \sigma_{min})\bar{A} + (\sigma_{max} - \sigma_{min})\bar{B}\cos 2\beta \quad (2.13)$$

where \bar{A} and \bar{B} refer to hole drilling constants, while β is the angle from x axis to the direction of maximum principal stress, σ_{max} . For hole drilled in infinite plate, \bar{A} and \bar{B} should be numerically calculated [120].

Despite the possibility to determine stress variation by deepening the hole, obtaining reliable measurement is difficult if the depth is beyond its diameter. Only two in-plane components of stress field can be measured with three-strain gauge rosette. The advantages of this method are: cost-effective, and commonly applied, including for polymeric material [121].

The method of water jet is preferred over mechanical drilling to minimise deformation depth induced by machining. Upon exceeding of residual stress by 50% of yield stress, errors may happen because of localised yielding. Despite applicability for all stress levels [122], this method is somewhat unviable for brittle or thin coating ($< 100 \mu\text{m}$).

Some shortcomings of this technique of hole drilling are: the detection is sensitive to close surface stresses (due to rapid decay of relieved strains), and varied results based on depth of hole. Errors may occur due to hole diameter, position, concentricity ($\pm 0.025 \text{ mm}$) [116], and depth (measured and controlled within $1 \mu\text{m}$) [117]. Since stresses can be induced by drilling process, high drilling speed is employed. Such procedure is destructive and the outcomes have readability issue [117] due to flat and rough surface.

The process of hole-drilling, application of calibration coefficients, and data analyses are detailed in ASTM: E837-95 “Standard Test Method for Determining Residual Stresses by the Hole-Drilling Strain-Gauge Method.” The related hole-drilling tool is illustrated in Figure 2.12.



Figure 2.12 Hole drilling apparatus [116].

2.7.4.4 Uncertainty of hole-drilling method

A number of uncertainties are present in the hole drilling technique. First, uncertainties in test system derive from dimension of gauge circle, hole alignment, temperature, and stress due to drilling, while second, stress calculation in test procedure [120]. Tools and experiments may be re-designed in order to minimise the parameter impacts, apart from addressing other factors, such as drill wear, operator skills, feed and speed of drill, gauge installation quality, voltage excitation, and data reduction techniques [121-122]. Since it is challenging to weigh in all parameters upon identifying drawbacks in hole drilling techniques, only few selected parameters are employed for investigations [120].

Outcomes of residual stresses measurements derived from measuring methods normally have single value based on fixed conditions. Uncertainties in methods applied are indicated by the varying empirical outputs [122-123], which may be compared, but unviable outcomes. In meeting the fixed conditions, measurement procedures and experimental set-up must go through careful inspection.

2.7.4.5 Magnetic

Magnetostriction and Barkhausen noise refer to the two magnetic approaches. The magnetostriction technique measures magnetic induction and permeability, whereas magnetic domain wall notion in Barkhausen noise [124]. The preferred domain orientations may be altered when magnetostrictive materials experience stress. This causes domains with nearly-oriented tensile stress to shrink (negative magnetostriction) or grow (positive magnetostriction). Stress-induced magnetic anisotropy send away induced magnetic field rotation from the direction of application. Monitoring such non-massive rotation is indeed possible using sensor coil for plane on the surface of component. Without rotation, both stress and magnetic field (principal axes) become parallel. Upon rotation of assembly, variance between principal stress size and direction can be determined. Changes in magnetostrictive strain due to magnetic domain walls movement generate elastic waves called ‘magnetoacoustic emission’, which can be identified from bulk material [124]. Meanwhile, Barkhausen emission refers to changes in emf that is proportional to the magnetic moment rate identified in probe coils as the

domain walls have movement. High frequencies generated by eddy current shielding attenuate it to provide solely near-surface probe (<250 μm). The advantages of magnetic techniques are cost-effective and viable for measurement of non-destructive residual stress [117].

The eddy current methods reflect induced eddy currents in tested to detect changes in magnetic permeability or electrical conductivity via changes in test coil impedance. Penetration depth may be modified through alteration of excitation frequency (~ 1 mm), while the applied stress direction cannot be determined by the probe. Studies pertaining to this technique display that eddy current techniques may be applied to more material genres than magnetic ones can. Despite inadequacy to fundamental residual stress measurement (eddy current sensitivity in monitoring microstructural variance and plastic work), the methods of eddy current offer cost-effective and rapid procedure [117].

2.7.4.6 Ultrasonic method

The ultrasonic speed alters when a material is subjected to stress, thus the measure of stress along wave path. Calibration tests are used to calculate acoustoelastic coefficients, which is integral for analysis. Varied wave types may be applied, but the critically refracted longitudinal wave technique is the most common. Highest sensitivity is noted when wave is propagated in similar direction as stress [118]. The following presents the fundamental calculation of stress:

$$V = V_0 + K\sigma \quad (2.14)$$

where V_0 denotes that the velocity of a wave is in an unstressed medium, σ is stress, and K is acoustoelastic constant (material parameter) [117].

2.7.4.7 Diffraction methods

Elastic strain, ϵ , can be detected using Bragg's equation (Equation 2.15) and interplanar spacing, d , changes via change in the Bragg scattering angle, $\Delta\theta$, and knowledge of the incident wavelength, λ .

$$\lambda = 2d\sin\theta \quad (2.15)$$

Giving following (Equation 2.16):

$$\epsilon = \Delta d / d_0 = -\Delta \cot\theta_0 \quad (2.16)$$

Thus, it is essential to accurately determine d_0 , the stress-free spacing. The outputs of strain may be translated into stress using suitable stiffness value [119].

i) Neutron diffraction

Neutron diffraction refers to a non-destructive technique that determines residual stresses in crystalline materials. This method offers values of elastic strain components, which are parallel to scattering vector to be translated into stress. Strain components are measured by neutron diffraction based on changes noted in crystal lattice spacing. When the crystalline materials are exposed to wavelength radiation near interplanar spacing (0.5-3 Å) in coherent and elastic manner, the radiation, which is as distinctive as Bragg peaks, is determined using position sensitive detector. The angle of peak is calculated with Bragg's equation [125] as following (Equation 2.17):

$$2d_{hkl}\sin\theta_{hkl} = \lambda \quad (2.17)$$

where λ is radiation wavelength, d_{hkl} is lattice plane spacing of crystallographic planes, hkl , responsible for Bragg peak, and θ_{hkl} is angular position of diffraction peak. The peak appears at $2\theta_{hkl}$ from the incident beam. When a sample becomes elastically

strained, its lattice spacing modifies, hence the apparent elastic strain due to the shift in $2\theta_{hkl}$ for a plane that is illuminated by a fixed wavelength. Upon differentiating Bragg's equation [125],

$$\Delta\theta_{hkl} = -\left(\frac{\Delta d}{d_0}\right) \tan\theta_0 \quad (2.18)$$

where Δd is change in lattice spacing, and d_0 refers to lattice spacing of a stress-free sample. The following (Equation 2.19) displays the calculation for strain in hkl set of planes.

$$\epsilon = \Delta d/d_0 = -\Delta \cot\theta_0 \quad (2.19)$$

The measured strain direction is perpendicular to diffracting planes, and along scattering vector [120-121].

ii) Synchrotron diffraction

Synchrotrons (hard X-rays) offers highly intense beams of high energy X-rays. These X-rays possess higher depth penetration than conventional X-rays (~50 mm in Al). Such scenario leads to increment in penetration depth, suggesting the capability of synchrotron diffraction to give high spatial resolution, and 3D maps of strain distribution to mm depth in engineered elements. Higher penetration depth is a major benefit of synchrotron diffraction over conventional XRD [122].

The intense narrow beams (1 mm - 10 μ m) is also another advantage, which reveals spatial resolutions rapidly, but limited by crystallite size of the material. To date, availability of synchrotron diffraction is noted only at several facilities, similar case as neutron diffraction [122-123].

iii) X-ray diffraction

Figure 2.13 shows the orthogonal coordinate systems applied to generate the equations displayed. The axes \underline{S}_1 S_i are for sample surface with \underline{S}_1 and \underline{S}_2 on the surface. \underline{L}_1 defines the laboratory system with \underline{L}_1 being the direction of normal to planes (hkl), by measuring interplanar spacing, d . \underline{L}_2 is angle ϕ with \underline{S}_2 and is in plane defined by \underline{S}_1 and \underline{S}_2 . Upon obtaining interplanar lattice spacing, d , from the diffraction peak for a given reflection hkl, the strain component along \underline{L}_3 is retrieved via [125] as following (Equation 2.20):

$$(\varepsilon'_{33})_{\phi\psi} = \frac{d_{\phi\psi} - d_0}{d_0} \quad (2.20)$$

where d_0 is unstressed interplanar spacing.

(Primed components refer to laboratory system \underline{L}_1 , while those unprimed are sample coordinate system, \underline{S}_1)

The strain in Equation 2.20 is translated into sample coordinate system via tensor transformation [126] as following (Equation 2.21).

$$\begin{aligned} (\varepsilon'_{33})_{\phi\psi} &= \frac{d_{\phi\psi} - d_0}{d_0} \quad (2.21) \\ &= \varepsilon_{11} \cos^2 \phi \sin^2 \psi + \varepsilon_{12} \sin 2\phi \sin^2 \psi + \varepsilon_{22} \sin^2 \psi \sin^2 \phi \\ &\quad + \varepsilon_{33} \cos^2 \psi + \varepsilon_{13} \cos \phi \sin \psi + \varepsilon_{23} \sin \phi \sin 2\psi \end{aligned}$$

Equation 2.21 reflects the basic equation applied in XRD strain measurement.

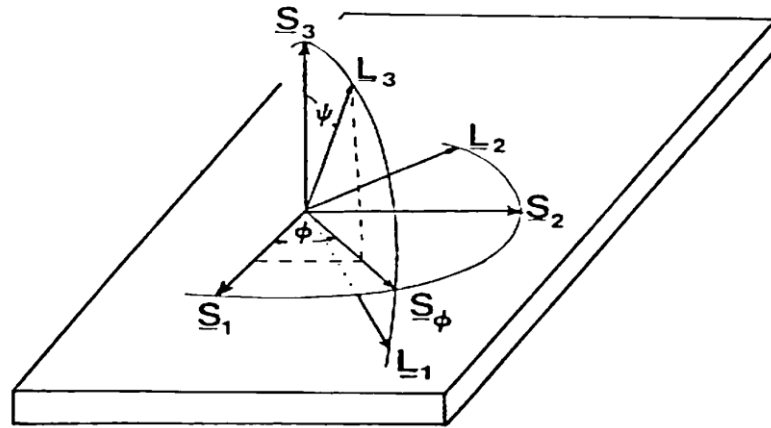


Figure 2.13 Sample and laboratory coordinate systems [120].

A major drawback of XRD refers to the measurement of un-stressed d-space. A number of methods are available to measure unstressed lattice spacing, d_0 . Adhering to biaxial assumption, the lattice spacing measured at $\psi = 0$ is replaced for d_0 , because this assumption gives insignificant amount of errors. Meanwhile, another technique applies data retrieved from the stress measurement itself. With biaxial stress state, this technique can distinguish d_0 from d vs. $\sin^2\psi$ graph. Measurement accuracy can be affected by the procedures applied in identifying unstressed d-space. Increment in d_0 minimises the measured residual stress amplitude [126].

Apart from the mentioned factors, some parameters may introduce errors in measurements, for example, Psi angles for $\sin 2\psi$ technique, peak position technique, plane curvature, aperture dimension, and fluctuation. Nonetheless, XRD is an exceptional method to determine residual stress due to the advanced XRD tools (hard/software) and cutting-edge correction factors calculation in enhancing XRD accuracy. The XRD accuracy in measuring residual stress is ± 20 MPa, limited by surface condition. Penetration for aluminium is $< 50 \mu m$, while other materials, titanium for instance, its penetration is only $< 5 \mu m$ [127]. Errors and uncertainties are present in residual stresses measuring methods [128]. Shortcomings of XRD and hole-drilling are further elaborated as these techniques are employed by 75% of industrial practitioners and academics [129]. Based on the findings of hole-drilling and XRD, it shows that XRD is a better choice of measurement method in this study since the specimens need to be used for surface hardness test as well. Therefore, a non-destructive is the obvious selection in this study.

2.8 Residual stress relaxation

In surface treated components, the residual stresses are self-equilibrating and the profiles of the residual stress fields are dominantly dependent on the material and treatment method [130]. Despite vast studies [131], technical challenge in comprehending, as well as accurately quantifying residual stress relaxation and redistribution (cyclic mechanical and thermal load), is still present. Figure 2.14 shows observation made by Mattson and Coleman [132] about cyclic residual stress relaxation.

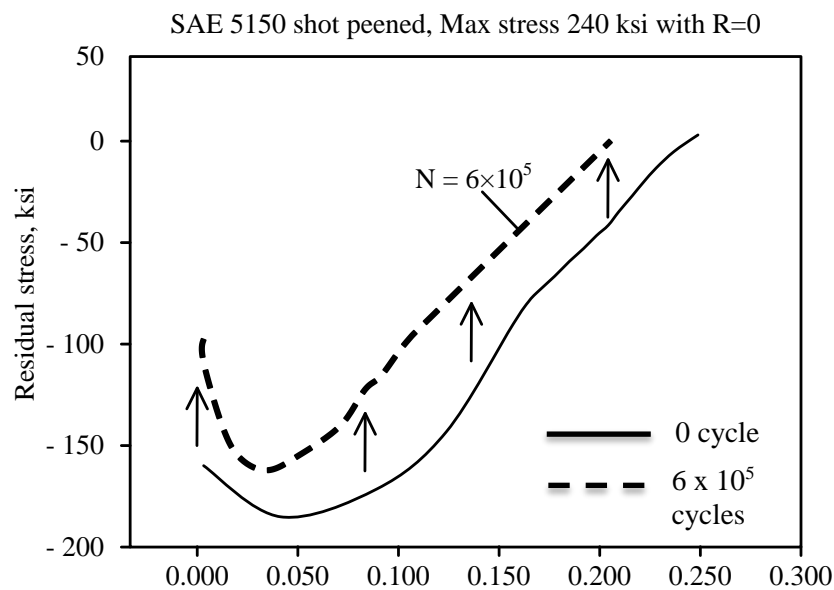


Figure 2.14 Residual stress relaxation before and after cyclic loading [133].

There is a positive impact on fatigue life despite partial relaxation of the compressive residual stress. If residual stress relaxation is omitted, fatigue lives would be underestimated. Nonetheless, the challenges in determining residual stress relaxation while operation of component could impede tracking of relaxation and assessment of effect in light of remaining fatigue life. Morrow and Sinclair [133] estimated residual stress relaxation via mean stress relaxation derived from axial fatigue test.

Based on that conception, Jhansale and Topper [134] formulated a logarithm linear correlation between mean stress relaxation and axial strain-controlled cycles. Both models neglected the effect of stress ratio in light of residual stress relaxation, mainly because the mean stresses in axial tests were dictated by the initially applied mean strain that was held constant. Besides, neither model contended with self-equilibrating residual

stress fields. Within the engineering domain, residual stress fields are subject to varied stress ratios based on component position, except for the case in uniaxial mean stress testing. At component operation, the beneficial compressive residual stresses at the component surface are often imposed to cyclic loading with positive mean stress. As such, the residual stress relaxation rate could become drastic at the initial phases of fatigue cycling. In extreme cases [135], residual stress can become entirely relaxed for the initial few load cycles.

In explaining the mechanism of residual stress relaxation, Kodama [136] measured the decrease of residual stress on the surface of shot-peened samples via XRD. The empirical outputs supported the linear logarithmic decreasing correlation between residual stress and load cycles after the first cycle. This correlation becomes non-applicable to drastic initial residual stress reductions for the first few load cycles. Based on the outcomes illustrated in Figure 2.15, the compressive residual stress in the first load cycle may attain relaxation that could exceed 50%. However, it is impractical to apply a model that fails in estimating the integral relaxation at the initial load cycle. Holzapfel et al., [137] extended this correlation by interpolating residual stress relaxation under thermal fatigue loading, wherein cyclic and thermally activated stress relaxation may take place.

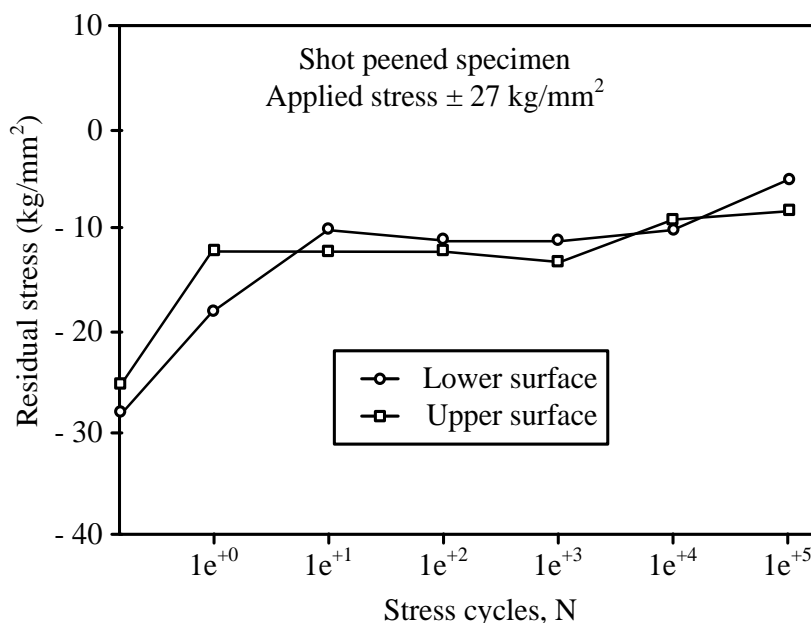


Figure 2.15 Residual stress relaxation at the surface of a specimen [136].

2.8.1 Previous works on residual stress relaxation

Ghaderi et al. (2019) studied the effective parameters on welding residual stress relaxation in aluminium cylindrical shells under cyclic pressure numerically and experimentally [138]. FEM was used in this study to simulate the cyclic pressure with various amplitudes and cycle numbers. Result found cyclic pressure redistribute the residual stress which can be relaxation and enhancement depending on the initial residual stress (compressive or tensile). Cui et al. (2019) found a similar result where the cyclic loading would decrease the weld residual stress [139]. Zhu et al. (2019) performed a study on thermal relaxation of residual stress on alloy composites by experiment. Shot peening was used to induce initial residual stress and annealing temperature of 150°C, 200°C and 250°C were applied. Results showed that shot peened layer decreased firstly due to thermal recovery. It can be concluded that increasing the temperature would accelerate the residual stress decrement [140]. A few other researchers investigated the effect of changing the parameters on material such as annealing temperature, post weld heat treatment and cold expanded holes and they found that the initial residual stress would definitely change or reduced significantly due to these parameters changing [141 -147].

2.9 Modelling of residual stress relaxation

The cyclic relaxation of compressive residual stress [132] reduces the benefits of surface engineering residual stresses.

Strain-controlled fatigue tests and a relationship between mean stress and load cycle were proposed and conducted to quantify cyclic residual stress relaxation [133] as follows (Equation 2.22):

$$\frac{\sigma_{mN}}{\sigma_{m1}} = \frac{\sigma_y - \sigma_a}{\sigma_{m1}} - \left(\frac{\sigma_a}{\sigma_y}\right)^b \log N \quad (2.22)$$

Where σ_{mN} is mean stress at N th cycle, σ_{m1} refers to mean stress at the first cycle, σ_a denotes the alternating stress amplitude, σ_y reflects material yield strength, b is a constant that relies on material softening and applied strain range, $\Delta\varepsilon$. Equation (2.22) is non-applicable for load ratio $R \neq -1$, as the surface residual stress is analogous to mean stress

when material is subjected to completely reversed loading. The empirical outcomes were supported by Equation (2.22) for $N > 10^6$ and $\sigma_{mN} < 20$ MPa.

A linear reduction in residual stress as a function of exponent of the number of cycles, N , was proposed by [134] for welded steel components through the correlation between residual stress ratio after a single load cycle to initial residual stress, $\frac{(\sigma_{res})_{1cycle}}{(\sigma_{res})_{ini}}$ and $\frac{(\sigma_{res})_{ini} + \sigma_{app}}{\sigma_y}$ as follows:

For

$$\frac{(\sigma_{res})_{ini} + \sigma_{app}}{\sigma_y} < 1$$

The relationship between the relaxed residual stress and number of cycle is as in Equation 2.23.

$$(\sigma_{res})_{relax} = (\sigma_{res})_{ini} N^{-0.004} \quad (2.23)$$

On the other hand, for

$$\frac{(\sigma_{res})_{ini} + \sigma_{app}}{\sigma_y} \geq 1$$

The relationship between the relaxed residual stress and number of cycle is as in Equation 2.24.

$$(\sigma_{res})_{relax} = (\sigma_{res})_{ini} \left\{ -1.6 \left[\frac{(\sigma_{res})_{ini} + \sigma_{app}}{\sigma_y} \right] + 2.6 \right\} N^{-0.004} \quad (2.24)$$

The findings showed the relaxation of the residual stress was large at the first cycle load however at the repetition of the cyclic load the residual stress relaxation is negligible to estimate fatigue strength.

The following (Equation 2.25) depicts the correlation between mean stress and load cycle to determine cyclic residual stress relaxation [134]:

$$\sigma_{mN} = \sigma_{m1}(N)^B \quad (2.25)$$

where B is relaxation exponent dependent on material softening and applied strain range $\Delta\varepsilon$.

Residual stress decreases on the surface of shot-peened specimens via XRD was measured by [135] and proposed the following linear logarithm relationship (Equation 2.26).

$$\sigma_N^{re} = A + m \log N \quad (2.26)$$

where σ_N^{re} is surface residual stress after N cycles. A and m are material constants that rely on stress amplitude, σ_a . The empirical outcomes supported the linear logarithm decreasing correlation between residual stress and load cycles only after the initial cycle.

Using FEM proposed analytical model for relaxation of residual stress, it estimates relaxation with $R = 0$ and $R = -1$ very close to that retrieved by FEM [126]. The model includes the impact of initial cold work. The following (Equation 2.27) is the proposed equation to estimate residual stress relaxation:

$$\frac{\sigma_N^{re}}{\sigma_0^{re}} = A \left(\frac{\sigma_{max}\sigma_a}{C_w\sigma_y} \right)^m (N - 1)^B - 1 \quad (2.27)$$

where C_w is a parameter that accounts for cold working extent. Material constants, m and A , rely on cyclic stress and strain response. Constant B controls the relaxation rate versus loading cycles. The initial residual stress is σ_0^{re} . In determining the impact of loading ratio, R , on relaxation, Equation 2.27 is rewritten as follows (Equation 2.28):

$$\frac{\sigma_N^{re}}{|\sigma_0^{re}|} = A \left(\frac{2\sigma_a^2}{(1 - R)(C_w\sigma_y)^2} \right)^m (N - 1)^B - 1 \quad (2.28)$$

Nevertheless, empirical investigation is imminent for cycle-dependent residual stress relaxation to verify both analytical and numerical models.

2.10 Summary of literature review

A component's fatigue behaviour is influenced by residual stresses that are introduced into the mechanical parts during the manufacturing processes. Residual stress exists in all rigid parts, metallic or otherwise. It is a result of the manufacturing process, the metallurgical as well as mechanical properties of the component. Depending on the scale of the stress it has three levels: first level (macroscopic residual stress), second level stress (heterogeneity and anisotropy of each crystal/grain in polycrystalline material), and third level stress (crystal scale).

The residual stress can be divided into mechanical, thermal and metallurgical categories. The residual stress can be used to improve the material performance, for example, inducing compressive residual stresses in the surface region can be advantageous.

The fatigue life can be estimated quantitatively using the residual stress. However, the residual stress parameter is not considered directly by industrial sectors. The inclusion of residual stress into design must be gradual and in phases.

The reduction and redistribution of the residual stresses during the component's fatigue life is called relaxation however compressive residual stress on fatigue life is still beneficial. Quantifying residual stress relaxation and redistribution under cyclic mechanical and thermal load remains a technical challenge. If the residual stress was not taken into consideration, the fatigue life of a component will be under predicted. In reality, the tracking of the residual stress relaxation and assessing its effects on the remaining fatigue life is impeded by the difficulty in measuring residual stress relaxation during component operation.

The main findings throughout the literature review is that the existing models of residual stress relaxation does not incorporate the surface hardness. In addition, there were no studies on the residual stress relaxation for ASTM A516 grade 70 steel material. These findings is tabulated in Table 2.8 with a clear highlight of the research gaps.

Table 2.8 Summary of previous studies on modelling of residual stress relaxation

Journal paper title	Author	Year	Summary/findings
Effect of shot peening variables and residual stress on fatigue life of leaf spring specimens	Mattson & Coleman	1954	Relaxation of residual stress was studied only the 6×10^5 cycle and RS measurement also performed in depth (not only on the surface).
Cycle-dependent stress relaxation	Morrow & Sinclair	1958	Empirical model developed was based on axial fatigue and did not incorporate any other parameters.
The behaviour of residual stress during fatigue stress cycles	Kodama	1972	Empirical model for annealed carbon steel and correlation is linear logarithm and not applicable for drastic initial RS reduction.
Engineering analysis of the inelastic response of a structural metal under variable cyclic strains	Jhansale & Topper	1973	Empirical model and neglected the effect of stress ratio.

Journal paper title	Author	Year	Summary/findings
Residual stress relaxation in an AISI 4140 steel due to quasistatic and cyclic loading at higher temperature	Holzapfel & Schulze	1998	Empirical model developed incorporating annealing temperature. Empirical model developed for residual stress relaxation after cyclic load and did not incorporate other parameters.
Investigation of residual stress relaxation under cyclic load	Zhuang & Hatford	2001	Numerical only and not validated by experimental data. Model incorporated cold work percentage.
Modelling of residual stress relaxation of fatigue in 2024-T351 aluminium alloy	Zarog & Ali	2011	Empirical model and incorporating “micro-hardness” & cold work for 2024-T351 aluminium alloy.

CHAPTER 3

MATERIALS AND METHODOLOGY

3.1 Introduction

This chapter discusses the methods used for this study. This study is divided into two parts namely the experimental and simulation methods.

Firstly, the experimental part was initiated with purchasing ASTM A516 grade 70 steel plate from a material supplier. This plate was then cut into testing samples according to ASTM E8 standard. The samples were then subjected to observation under a scanning electron microscope (SEM), shot peening process with two intensities (6.28A and 12.9A) and mechanical tests like hardness test, tensile test and surface roughness measurement. X-Ray diffraction was used to measure the initial residual stress values induced by different shot peening intensities for the shot-peened samples. Simultaneously, the samples also underwent SEM examination to study the changes in the microstructure due to shot peening process. Cyclic loads at low amplitude (20% of Yield Strength) and high amplitude (80% of Yield Strength) were applied on the shot-peened samples. This process was done to study the relaxation of the initial residual stress and the reduction of surface hardness due to different amplitudes of the cyclic loads. X-Ray diffraction was performed on each of the samples at different cycles (1, 10, 100, 1000 and 10 000) to measure the residual stress values. The result was used to generate an empirical model of residual stress relaxation. In addition, the result from surface hardness reduction was used to integrate with the residual stress relaxation model. The residual stress relaxation model was also used to validate the numerical model generated from the simulation part.

Next, the simulation was initiated with the development of the CAD model using SolidWorks (2016) software according to the dimensions used in the experimental part. The geometry was according to the standard ASTM E8 (Standard Test Methods for Tension Testing of Metallic Materials). Secondly, the material properties and mesh size were set up. In the first part of the simulation, shot peening was employed to introduce

initial residual stress. The methodology of this step is explained in detail in subchapter 3.1. The second part of the simulation involved the mapping of the residual stress known as the residual stress relaxation. The relaxation was simulated by applying a cyclic load, where the remaining residual stress after different cycles (0, 1, 2, 10, 100 and 1000) was determined. The last step for this simulation part was to generate a numerical model based on the results of residual stress after each cycle. Figure 3.1 represents the overall research flow.

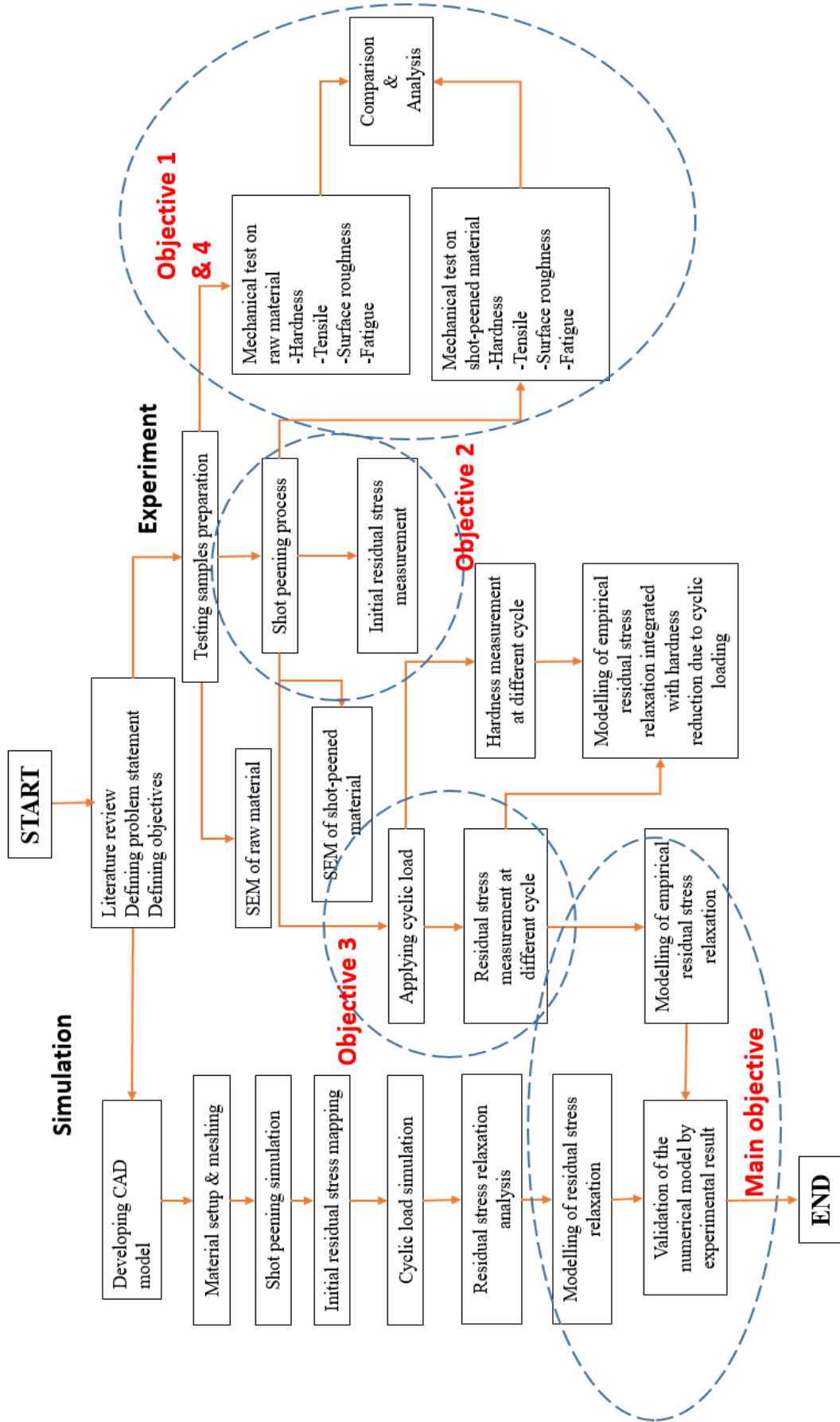


Figure 3.1 Overall research flow.

3.2 Experiments

The experimental method in this study begins from sample preparation, followed by material properties testing which includes hardness test, tensile test, fatigue test, SEM and surface roughness test. The samples were then shot-peened with a set of particular parameters to introduce initial residual stress on the material. The shot-peened samples were once again subjected to material properties testing. The properties between before and after shot peening process were analysed.

Next, the shot-peened samples were subjected to cyclic loading. The surface hardness and residual stress values for each of the samples at different cycle were measured. The measurements were employed to generate an empirical model of residual stress relaxation integrated with the reduction of the surface hardness.

3.2.1 Sample preparation

Material ASTM A516 Grade 70 Steel was purchased in 1-meter x 1-meter size with a thickness of 6.4 mm. The material plate was cut using the Computer Numerical Control (CNC) cutting machine according to the standard ASTM E8 dog bone measurement, which is a Standard Test Methods for Tension Testing of Metallic Materials. Figure 3.2 illustrates the dimensions of the test sample sent for cutting. While Figure 3.3 represents the actual sample after the cutting process.

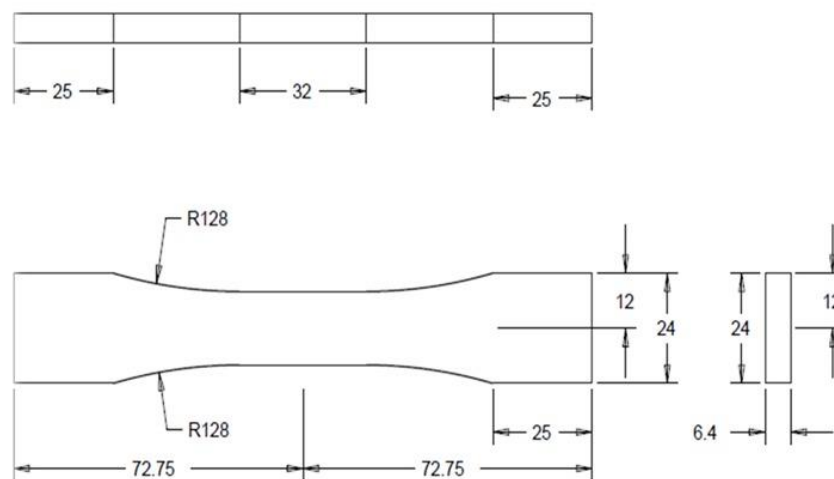


Figure 3.2 Detail drawing of test sample sent for cutting.

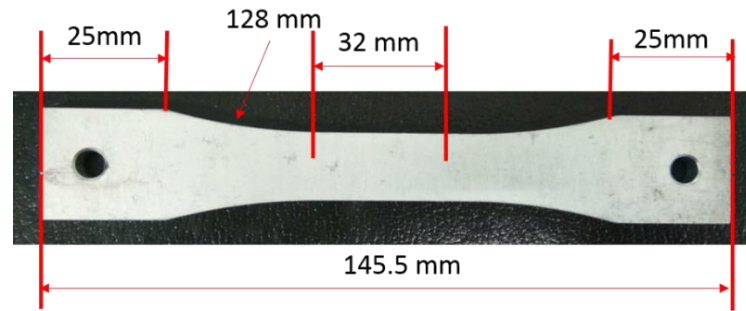


Figure 3.3 Actual sample after cutting process.

3.2.2 Raw material control (mechanical and microscopic test)

Prior to surface treatment, the control material (raw material) was subjected to mechanical and microscopic testing. The test results were retained as control data for comparison purposes. Therefore, the raw material ASTM A516 Grade 70 were subjected to mechanical testing as in the flowchart (Figure 3.1). The tests conducted on the control samples include tensile test, hardness test, fatigue test and SEM.

3.2.2.1 Tensile test

The tensile test was performed at a material laboratory in Uniten using Zwick-Roell tensile testing machine (Zwick-Roell, United States of America). The tensile test was performed according to the ASTM E8 standard [12] to measure the stress-strain performance of the raw material. In this test, the dog-bone-shaped sample was pulled until failure. The sample which experienced pulling within its elastic, necking and plastic regions finally broke. During the pulling process, the data of stress and strain were recorded to generate the “stress-strain curve”. Based on this curve, the value of Yield Strength, Ultimate Tensile Strength and the Young’s Modulus were determined. Figure 3.4 demonstrates the tensile test performed on the samples.

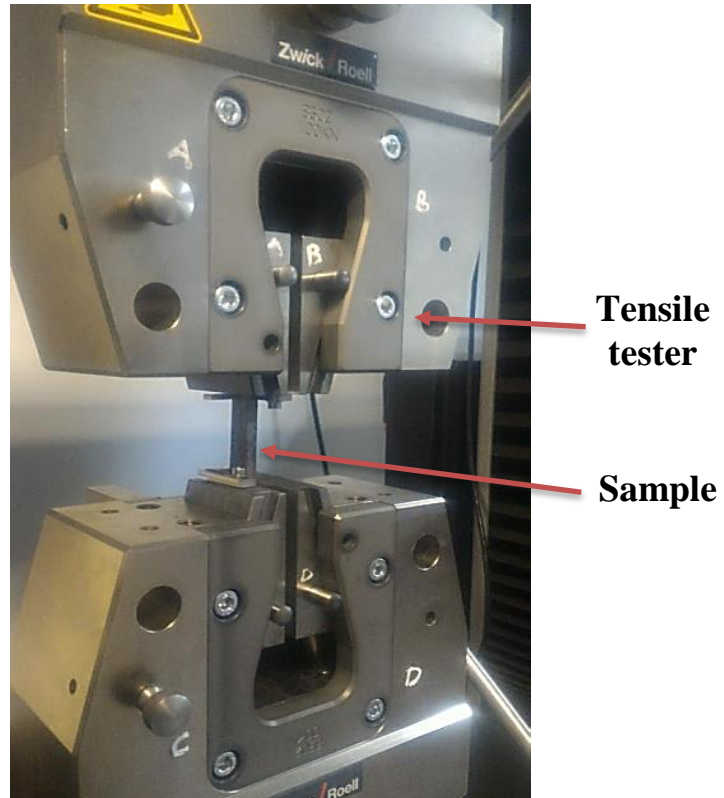


Figure 3.4 Tensile test equipment.

3.2.2.2 Hardness test

Hardness measurement was performed on the samples to study the relationship between hardness and residual stress. Hardness test was carried out using Rockwell Hardness Tester type B at a material lab in Uniten by measuring the hardness at 5 different points on each sample. The measurement was conducted by applying an indenter with a preliminary minor load of 10 kgf according to ASTM E18 standard [12]. Figure 3.5 represents the hardness test conducted on the samples.

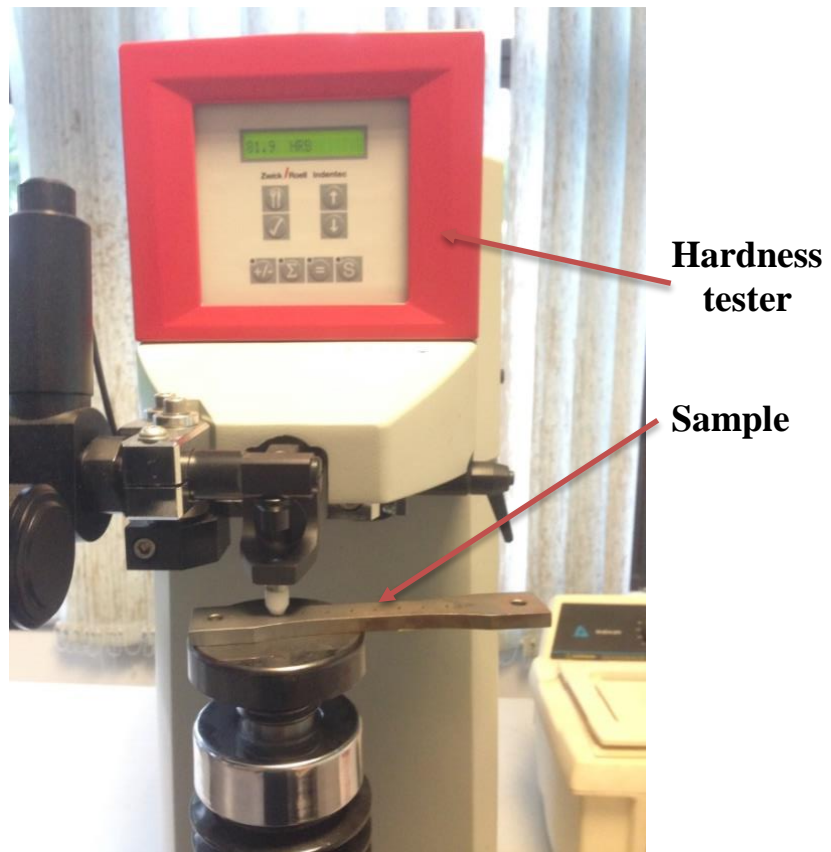


Figure 3.5 Hardness measurement equipment.

3.2.2.3 Fatigue test

Fatigue test was performed based on ASTM E466, “Standard Practice for Conducting Force Controlled Constant Amplitude Axial Fatigue Tests of Metallic Materials” [13]. Universal Testing Machine (UTM) was used to conduct the test. The test was done by applying cyclic loads of 85% (527 MPa) and 75% (465 MPa) of the Ultimate Tensile Strength. The frequency of the test was 15Hz.

3.2.2.4 Morphological characterisation

SEM was used to examine the tensile cracks and fatigue fractures on the samples upon the completion of the tensile and fatigue tests with the magnification of 1500x. Furthermore, a Philips XL30 SEM was used to investigate the microstructural characterisation under various sintering temperature and composition.

The grain size of the elements present in the material was determined from the scanning electron micrographs using the average grain intercept method. The average grain size is then calculated according to the equation proposed by Mendelson [18] as in Equation 3.10.

$$D = L / N \quad (3.10)$$

where “D” is the average grain size, “L” is the measured average interception length and N is number of intercepts the grain boundary makes with the line.

However, the line intercept technique used to determine the average grain size has its limitations. This technique can only be used for polycrystalline ceramics containing equiaxed grains which have grown normally to form a fully dense single-phase microstructure [18]. Figure 3.6 illustrates the SEM machine used to observe the microstructure of the material samples.



Figure 3.6 SEM machine.

3.2.3 Shot peening process

In this study, the shot peening process was executed in two places with different parameters. Shot peening was done at Asian Automotive Steels Sdn. Bhd. (A) and Abrasive Engineering PTE Ltd (B). The former, A, produces stabilizer bars in Malaysia. While, B is a blasting service company located in Singapore.

3.2.3.1 Shot peening A (SP A)

During the first round of shot peening (SP A), the samples were subjected to steel shots using a large size machine which is usually used to produce stabilizer bar. The stabilizer bar or also known as anti-roll bar is an automotive part used to reduce the body roll of a vehicle during fast cornering. The stabilizer bar normally measures between 1.0 to 1.5 m long.

Figure 3.7 illustrates the test sample assembled and ready for the shot peening process. The samples underwent a shot peening process before surface pre-treatment and coating. The stabilizer bar was also included in the figure to compare the size of the sample with the actual part used for this machine. Since this shot peening machine is for bigger size samples, the study samples from this study had to be hanged in the machine using steel wire.

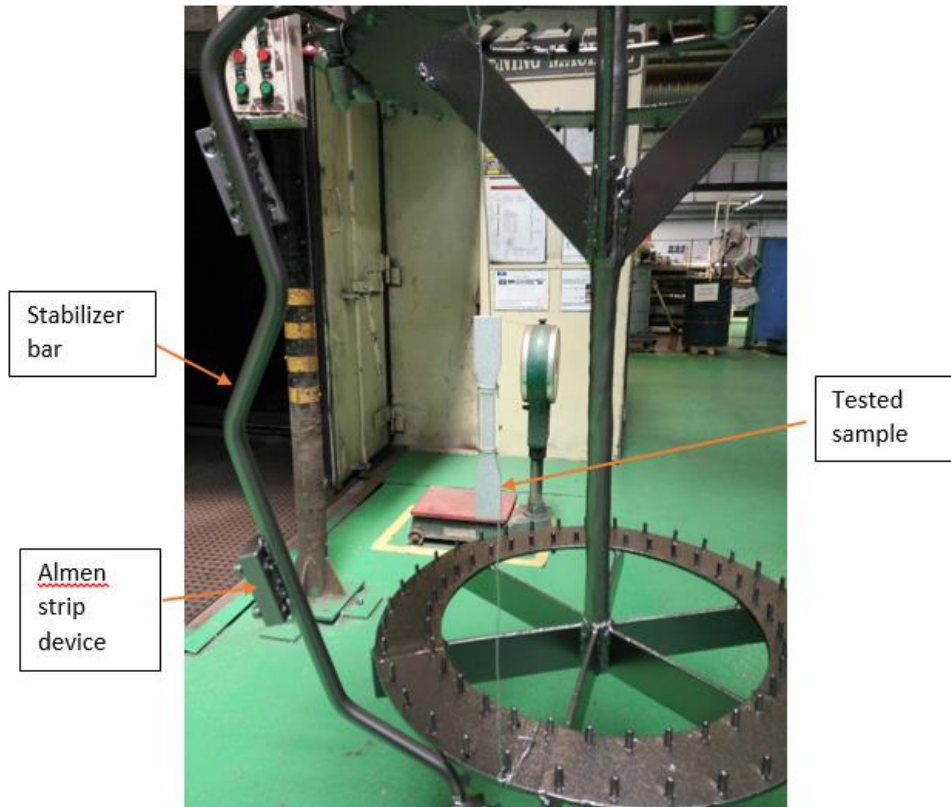


Figure 3.7 Shot peening process.

Parameters of the shot peening process were already fixed according to the manufacturer's product requirement which are the same parameters used for stabilizer bar. There were no changes made in the parameter setting. Table 3.1 summarises the parameters used in the first shot peening process.

Table 3.1 Shot peening A parameters.

Parameter	Value
Arc height (mm)	0.4
Peening coverage (%)	100
Rotation (Amp)	5~10
Steel shot grade	SAE S-330
Steel shot size (mm)	1.0
Steel shot hardness (HRC)	45~55
Nozzle angle (°)	37.5

3.2.3.2 Shot peening B (SP B)

The parameters for SP B were adjusted to study changes in the result. In this shot peening process, two types of steel shots were utilised to obtain different shot peening intensities. The two types of steel shots used were SAE S-110 and SAE S-230. The diameter of the steel shots was 0.4 mm and 0.7 mm respectively. Other parameters namely the applied pressure, nozzle speed, media flow, part to nozzle distance and nozzle angle were fixed. Table 3.2 summarises the parameters used for this shot peening process.

Table 3.2 Shot peening B parameters.

Parameter	Value	
Arc height	6.1A	12.9A
Steel shot grade	SAE S-110	SAE S-230
Steel shot size (mm)	0.4	0.7
Applied pressure (psi)	30	
Nozzle angle (degree)	45	
Nozzle speed (m/s)	0.1	
Part to nozzle distance (mm)	152.4	

3.2.4 Mechanical test on shot-peened material

Following shot-peening of the test materials, mechanical tests like tensile, hardness, fatigue and SEM examination were performed on the shot-peened samples as described in subtopics 3.3.2.1 to 3.3.2.4 to compare the mechanical properties before and after shot peening. An additional test was also done on the shot-peened samples which are the measurement of introduced residual stress by the shot peening process. It involved the application of cyclic loading to study the relaxation of this residual stress.

3.2.5 Cyclic loading

The cyclic load was applied to the samples after the shot peening process with a low load of 52 MPa (20% of Yield Strength) and a high load of 208 MPa (80% of Yield Strength). The number of cycles applied on the samples was 0, 1, 2, 10, 100, 1000 and 10000 cycles for each load. The frequency was set at 15 Hz for cyclic loading, similar to the frequency

for fatigue test. Figure 3.8 illustrates the UTM used to perform cyclic loading and the fatigue test on the study samples.

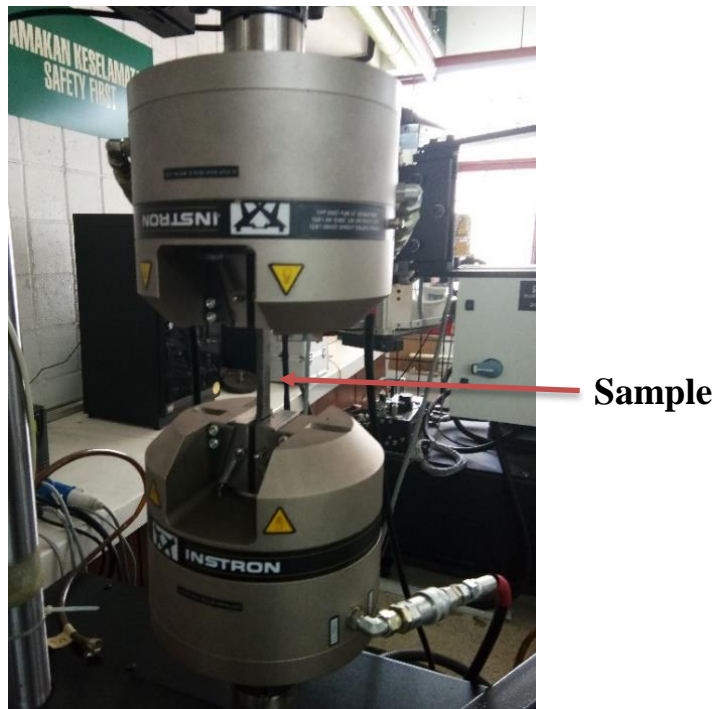


Figure 3.8 Universal testing machine for cyclic loading and fatigue test.

3.2.6 Residual stress measurement (X-Ray diffraction)

X-Ray diffraction (XRD) measurement was done on the samples after cyclic load to study the relaxation of compressive residual stress after the cyclic load was applied. The measurement was only made on the surface in a longitudinal direction at the centre of the gage region on the side opposite the specimen identification markings. XRD was performed using the two-angle sine-squared-psi technique, in accordance with SAE HS-784, employing the diffraction of chromium K-alpha radiation from the (211) planes of the BSS structure of the material. Details of the parameters used during the XRD measurement are listed in Table 3.3.

Table 3.3 Diffractometer parameter.

Parameter	Value
Incident beam divergence	0.8 degree
Detector	Scintillation set for 90% acceptance of the chromium K-alpha energy
Psi rotation	10 and 50 degree
Irradiated area	0.15 x 0.15 in (3.8 x 3.8 mm)

3.2.7 Surface roughness measurement

As an additional test, surface roughness was measured for each sample after shot peening process to study the change in surface roughness of the raw material after being exposed to different shot peening intensities. This test was done according to ISO standards using TR200. Figure 3.9 illustrates the equipment used for the measurement. TR200 is a portable device used to measure surface roughness. It includes graphical display on large LCD with very complete instrument along with pickup stylus position indicator. This product has 20 different roughness parameters..



Figure 3.9 TR200 surface roughness measurer.

3.3 Simulation

In the simulation part of this study, the actual conditions of the experimental setup were modelled using a software known as Altair HyperWorks (2017). Simulation is divided into three parts. First is the development of a CAD model according to the required dimensions in ASTM E8 [12]. Secondly is the shot peening simulation, followed by the residual stress relaxation. Defining the material properties is very important to ensure that the simulation replicates the actual condition.

3.3.1 CAD modelling

CAD model was developed based on the dimensions according to the standard ASTM E8. The sample dimension was set as described in Table 3.4 Figure 3.10 shows the detail dimension on the model.

Table 3.4 Dimensions of CAD model

Length (mm)	145.5
Wide (mm)	24
Thickness (mm)	6.4
Radius of the necking area (mm)	128

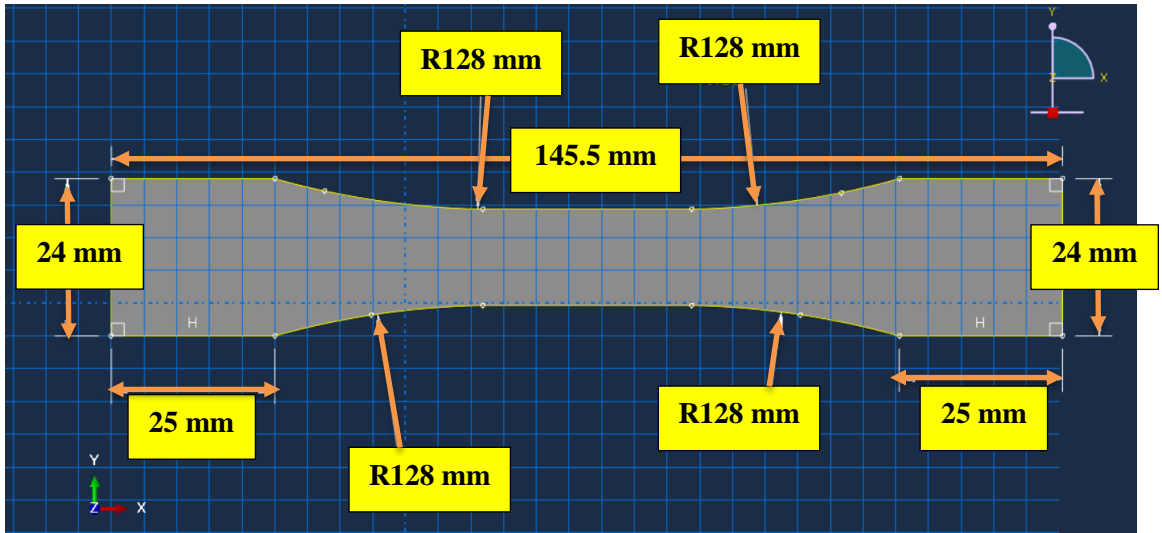


Figure 3.10 Detail dimension of the model.

Figure 3.11 is a 3D representation of the model which was extruded at 6.4 mm thickness.

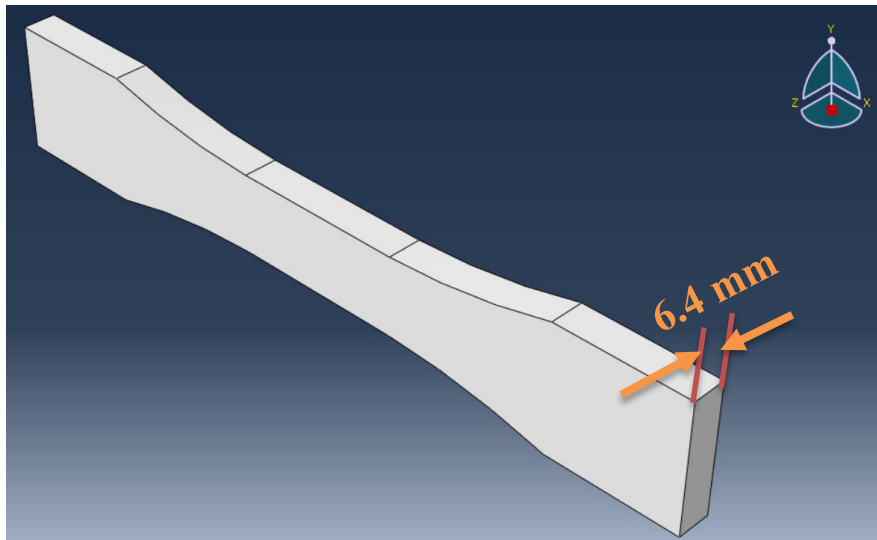


Figure 3.11 CAD model of test sample in 3D view.

3.3.2 Defining material properties

The material properties are defined accordingly based on Piecewise Linear Method . This method defines the material using stress-strain data from the experimental data. Validation was performed by assessing tensile simulation and by comparing the stress-strain curve result with the experimental result.

Based on tabulated Piecewise linear, ASTM A516 Grade 70 carbon steel is defined as an isotropic elastoplastic. The experimental stress-strain data from the tensile test defined the material behaviour in simulation. The values assigned for each property are 7.85 g/cc for material's density, 0.29 for Poisson ratio and 200 GPa for Modulus of Elasticity [9].

The elastic-plastic Piecewise linear material is a material model used to define material properties in a simulation activity. This law models an isotropic elastoplastic material using user-defined functions for the work-hardening portion of the stress-strain curve (for example, plastic strain vs stress) for different strain rates. In this study, this method was used to differentiate the properties of the materials based on their different peening intensities. The elastic portion of the material stress-strain curve is defined by the Young modulus (200 GPa) and the Poisson's ratio (0.29).

3.3.3 Meshing

The objective of meshing is to study the mesh convergence towards the residual stress value after shot peening (ball impact). The mesh type that was selected for this model was the 8-node linear brick known as the software "HEPH". It is a software using the co-rotational 1 Gauss point with physical stabilization via an hourglass control approach. HEPH is improved through the reduced integration with 8 node element, 1 point integration, physical hourglass stabilisation and its best mesh type to compromise between cost and quality. Figure 3.12 illustrates the mesh geometry of HEPH [149].

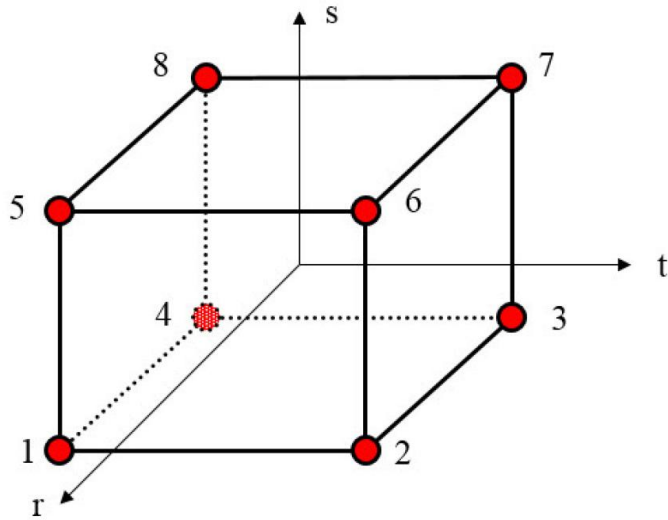


Figure 3.12 Mesh geometry of 8-node linear brick (HEPH) [59].

Several models were created with different mesh densities but the changes are made only around the middle area of the model. However, the mesh size and density at the other parts were maintained at 3 mm. This variation in mesh size and density is because the resulting stress and strain mainly occur in the middle area. While results from other areas were neglected. Besides, different mesh density was used as the meshing strategy because it is easier to control the mesh shape compared to specifying element size value. The higher the mesh density, the smaller the element and the higher the number of total elements. Therefore, five models with element densities ranging from 5x5 to 40x40 were created. The total number of elements were recorded for each model. Figure 3.13 represents the meshed model where the middle area is green in colour and end area in red. The number of elements for each model are tabulated in Table 3.5.

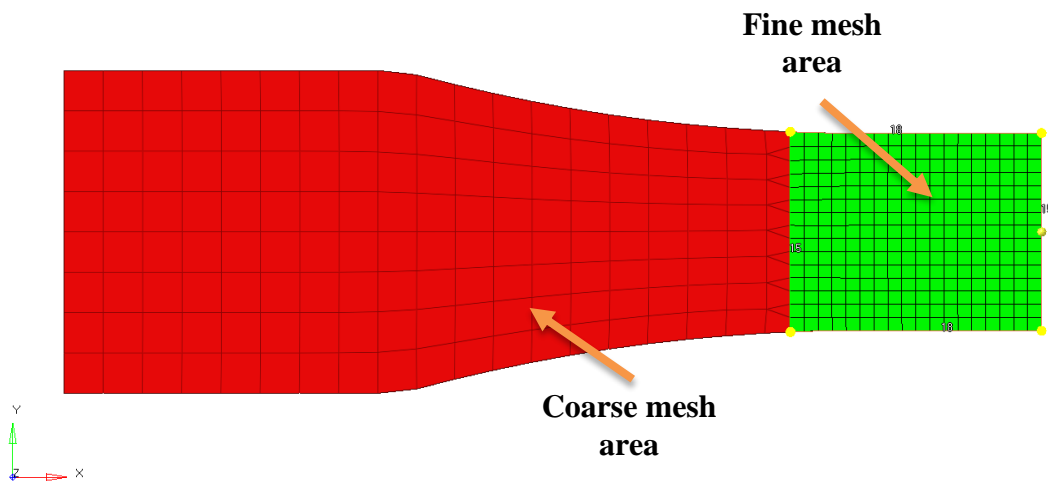
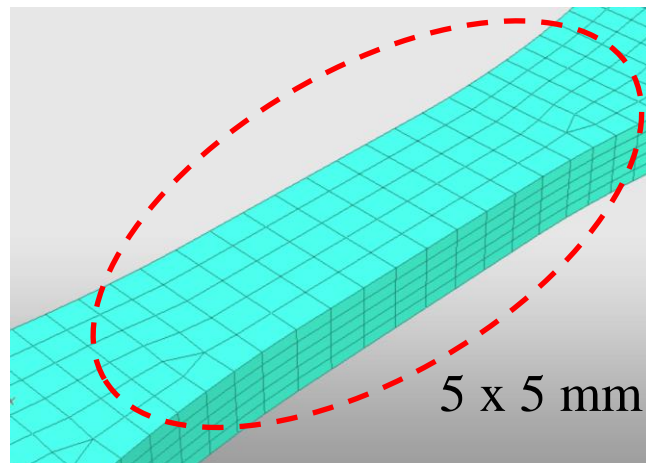


Figure 3.13 Meshed area.

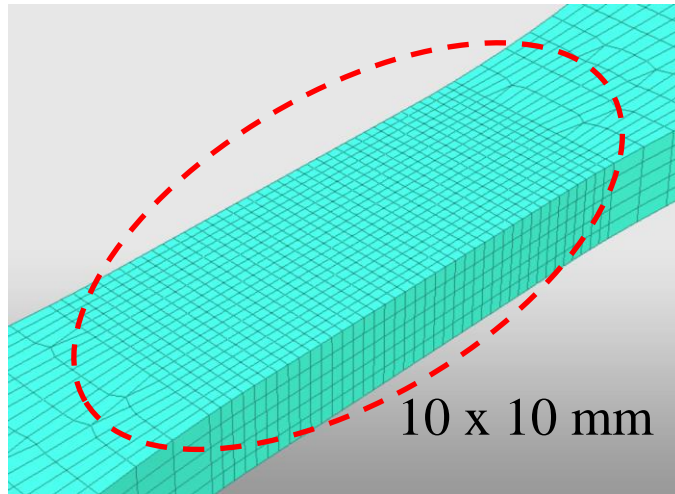
Table 3.5 Number of elements for shot peening models.

Model	No. of elements
1	61237
2	62337
3	63937
4	71498
5	78868

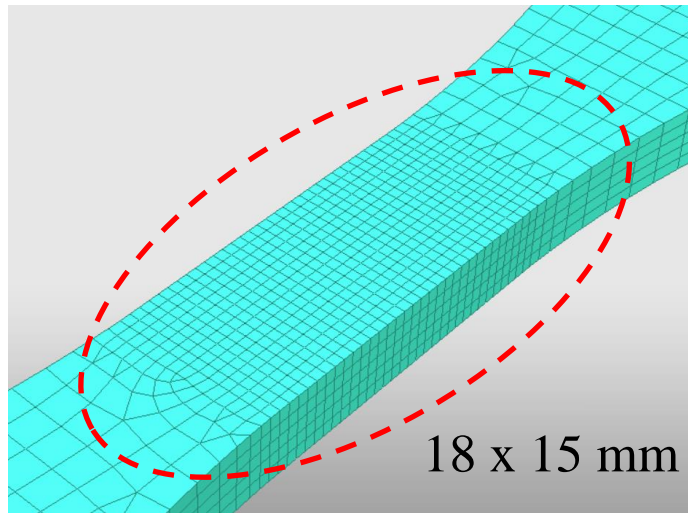
Figure 3.14 (a), (b), (c), (d) and (e) demonstrates the varying mesh sizes in the middle area for all five models with number of element ranging from 61,237 to 78,868 respectively. With the increase in the number of elements in the midsection, accurate simulation results can be generated. Another important criterion to be considered is the computational time which is also known as the simulation running time. A high number of elements increases the computational time and this computational time will be high for both shot peening and residual stress relaxation simulation.



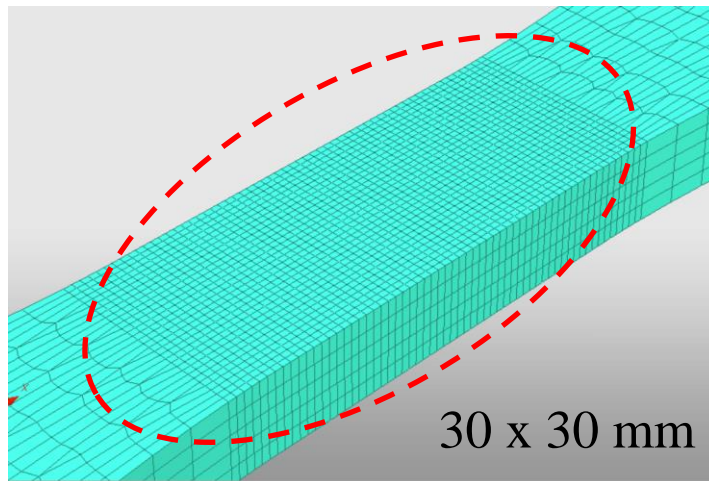
(a)



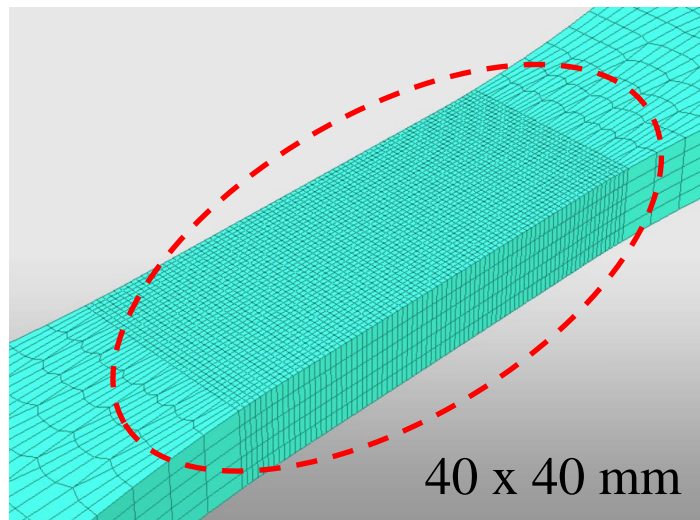
(b)



(c)



(d)



(e)

Figure 3.14 Different mesh size for middle area on the body (a) Model 1: Uniform mesh size in whole body (5 x 5 element density);(b) Model 2: Fine mesh in middle area (10 x 10 element density);(c) Model 3: Fine mesh in middle area (18 x 15 element density);(d) Model 4: Fine mesh in middle area (30 x 30 element density); (e) Model 5: Fine mesh in middle area (40 x 40 element density)

Using single shot impact method, the ball shot in the shot peening procedure is defined as steel ball with a density of 7.85 g/cc, Young's modulus of 210 GPa and Poisson's ratio of 0.3. These properties enable the ball to be classified as a solid. Whereas, the ball moves in a translational motion as it moves along one direction without the involvement of any rotational motion. The parameter of the impact is controlled only by the initial velocity of the ball. The initial velocity of the ball is set at different values (2 m/s, 5 m/s, 25 m/s, 50 m/s and 100 m/s). The stress exerted onto the impacted area is considered as the initial residual stress. The magnitude of the velocity to be used in shot peening simulation is selected based on the value of stress result in the impacted area after the collision. Finally, the results are mapped to test the stress induced by the impact as initial stress in the relaxation simulation.

3.3.4 Shot peening simulation

Once the ball impact parameters were set, the residual stress was introduced onto the material's surface by shot peening simulation. Shot peening simulation is a method to introduce the initial residual stress. This simulation is performed using a single shot impact by a ball with a diameter of 10 mm to cover the gauge area of the specimen. A

single shot was selected because the objective is to introduce a particular value of residual stress in the middle area. Since the target is to produce one value of residual stress, the number of shots does not influence the end result. Thus, the single shot simulation was chosen as it is much simpler and time-saving compared to multiple shots simulation.

The simulation method, HyperWorks consists of the linear and non-linear solver. The linear solver is mostly used in the static case. However, linear solver also can be used for dynamics, buckling, thermal, plasticity, quasi-static and contact cases. This simulation is faster (shorter time) but produces results with low accuracy. On the other hand, the non-linear solver is divided into implicit and explicit solver. The implicit solver is used for quasi-static, dynamics, post-buckling, materials and contact. While the explicit solver is used for impact, thermal, materials and contact. The most suitable solver for the shot peening simulation in this study which produces an impact between a steel ball and the specimen is the explicit solver.

Next, using the explicit solver in HyperWorks, an impact analysis was run between the two bodies as depicted in Figure 3.15 to simulate the shot peening process. The ball hit the sample at a 90^0 angle from the centre. The bottom surface of the sample is fixed in all direction by applying “ENCASTRE” as a boundary condition. A single spherical ball was set to hit the sample by applying initial velocity perpendicular to the impact surface. When shot particles pass through the impact region, they were accelerated by the drag force from the nozzle. The equation (Equation 3.1) of particles is described as:

$$m \frac{d^2y}{dt^2} = - \frac{\pi D^2}{8} C_D \rho_a(y) \{u(x, y) - v(x, y)\}^2 \quad (3.1)$$

where m is the particle mass and C_D is the coefficient of drag. For the spherical ball in turbulent flow, the C_D is 0.47. While $\rho_a(y)$ is the air density, D is the particle diameter, $U(x,y)$ is the air velocity and $v(x,y)$ is the particle velocity. Moreover, air density, $\rho_a(y)$, air velocity and $u(x,y)$ depend on the region of the shot particles [50].

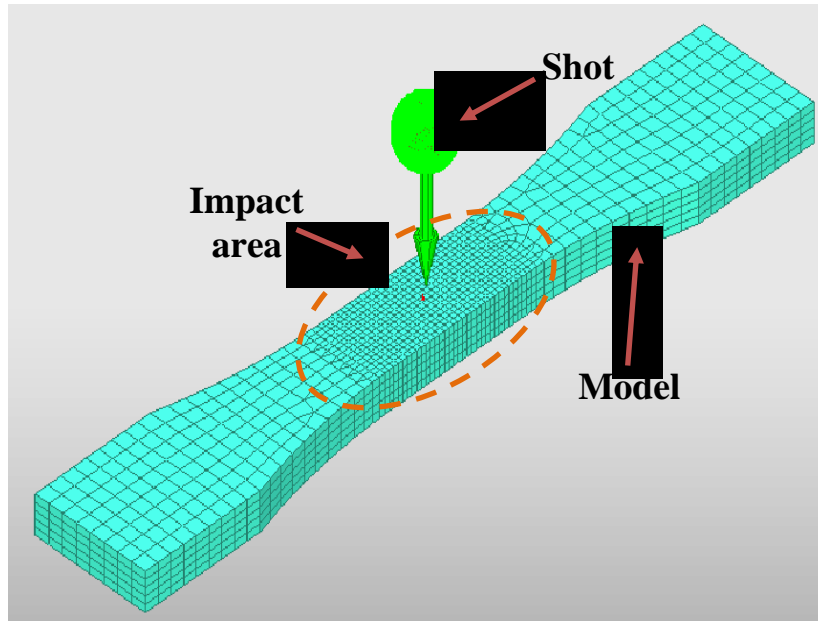


Figure 3.15 Direction of ball shot direction and angle towards the impact of the shot peening simulation model.

The parameters of shot peening simulation is tabulated in Table 3.6.

Table 3.6 Shot peening simulation parameters

Shot diameter (mm)	10
Shot's Young Modulus (GPa)	210
Shot's density (g/cc)	7.85
Shot's Poisson ratio	0.3
Shot angle (°)	90°
Shot speed	To be determined based on the impact stress result
Sample size and dimension	According to ASTM E8

The same FE model is exported to cyclic loading model to simulate the residual stress relaxation, hence to verify the results obtained in the experimental works.

3.3.5 Residual stress relaxation simulation

The relaxation simulation was conducted after the result of the stress impact in shot peening simulation was mapped. The impact of stress was used as the initial stress. The relaxation or reduction of this initial stress was investigated when the cyclic load was applied. Figure 3.16 displays the boundary condition set up for the model of residual stress relaxation. One end is fixed in every direction (ENCASTRE) and the cyclic load was applied in the other end.

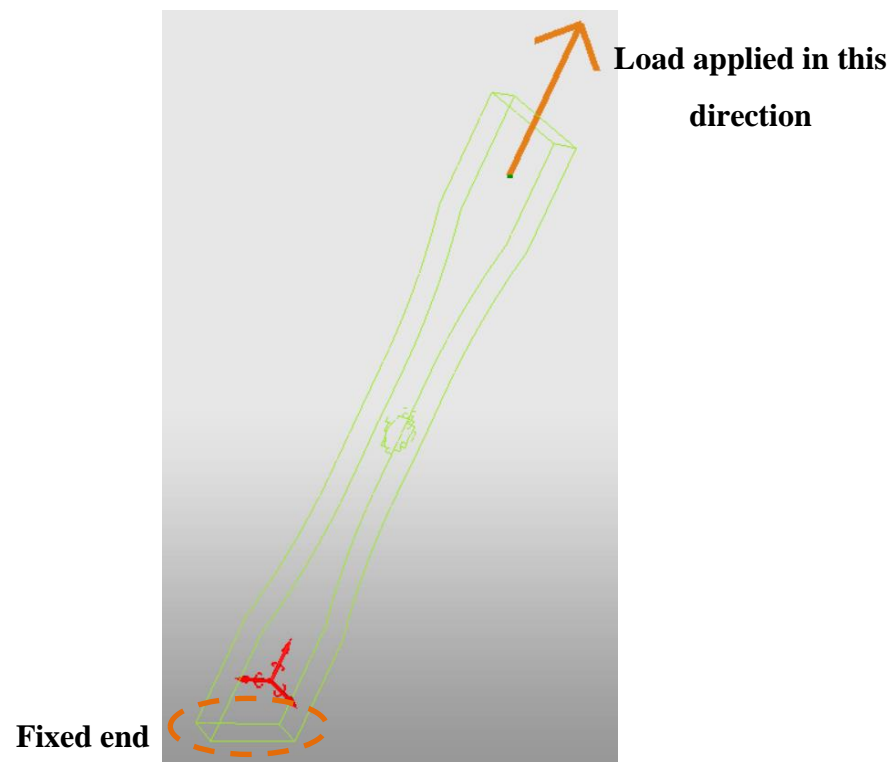


Figure 3.16 Boundary condition and load setup.

In this simulation, the cyclic load was introduced using load function (load vs time). Two amplitudes of cyclic load were applied to the model to simulate the actual condition in the experimental part. The ratio of the minimum and maximum load is 0.1 ($R = 0.1$). Low cyclic load fluctuates between 499.2 N to 4992 N which is 20% of the Yield Strength (52 MPa). While the high cyclic load fluctuates between 1996.8 N and 19,968 N which is 80% of the Yield Strength (208 MPa). The force applied was calculated by multiplying the value of tensile stress, σ_t with the cross-section area, A (Equation 3.2):

$$\sigma_{t_{max}} = \frac{F_{max}}{A} \quad (3.2)$$

Equation 3.2 is re-arranged into Equation 3.3:

$$F_{max} = \sigma_t A \quad (3.3)$$

Where $\sigma_t = 52 \text{ MPa}$ (20% of Yield strength of 260 MPa)

And $A = (15 \text{ mm} \times 6.4 \text{ mm}) = 96 \text{ mm}^2$

The values are substituted into Equation 3.3 to generate:

$$F_{max} = (52 \text{ MPa})(96 \text{ mm}^2)$$

$$F_{max} = 4992 \text{ N}$$

The ratio of minimum load to maximum load is 0.1. Therefore, F_{min} was calculated as below:

$$F_{min} = \frac{4992 \text{ N}}{10}$$

$$F_{min} = 499.2 \text{ N}$$

Same steps were applied to calculate high load, where $\sigma_t = 208 \text{ MPa}$ (80% of Yield strength of 260 MPa). The σ_t value was substituted into Equation 3.3 to generate:

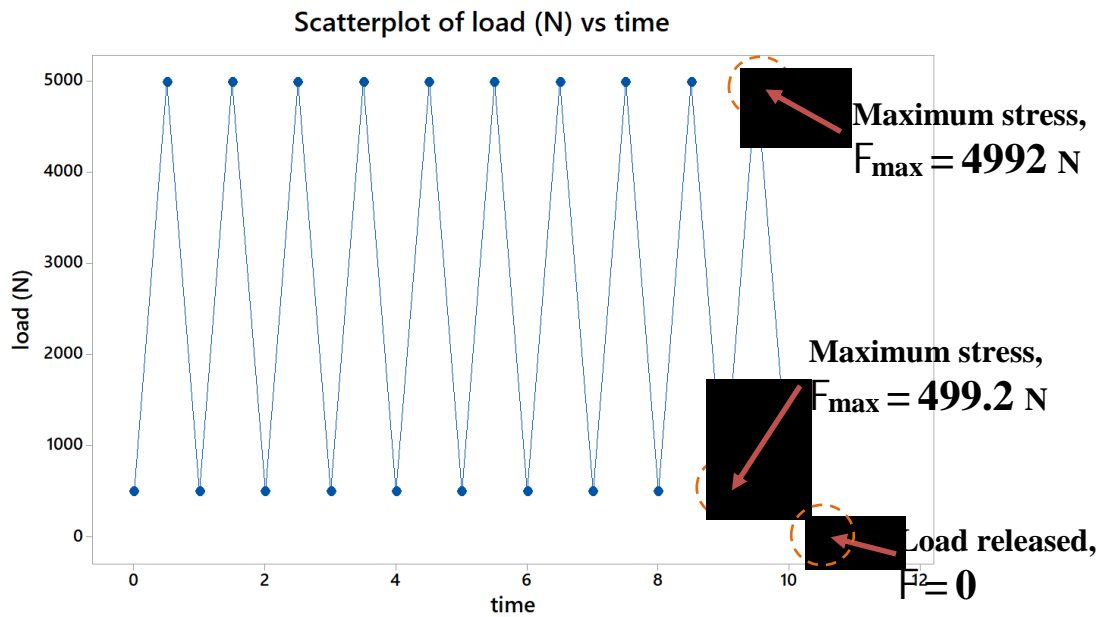
$$F_{max} = (208 \text{ MPa})(96 \text{ mm}^2)$$

$$F_{max} = 19,968 \text{ N}$$

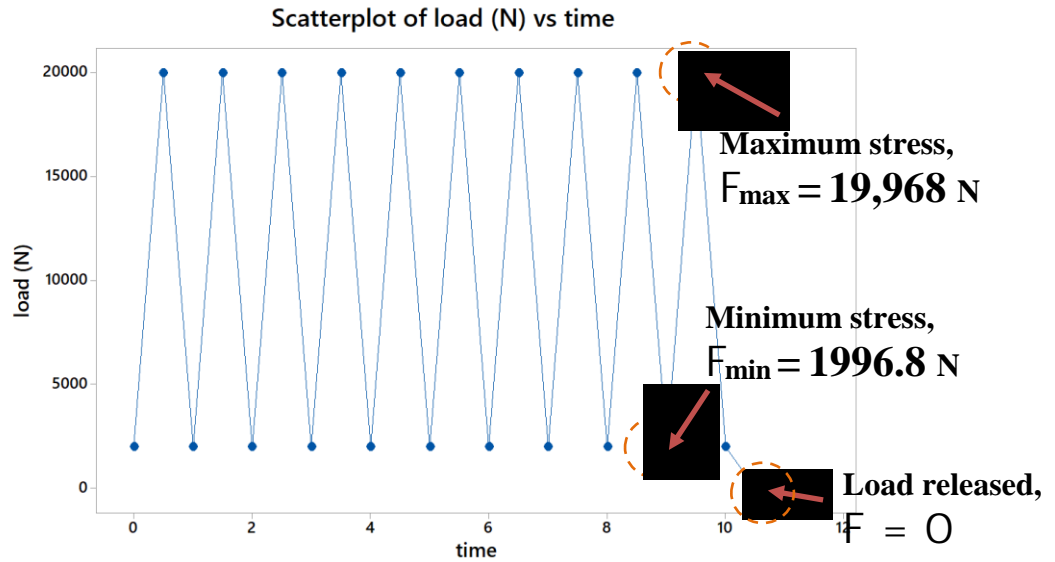
and

$$F_{min} = 1996.8 \text{ N}$$

Figure 3.17 demonstrates the low and high cyclic load function applied to the model respectively.



(a)



(b)

Figure 3.17 Cyclic load function defined in the residual stress relaxation simulation (a) low cyclic tensile loading (b) high cyclic tensile loading.

CHAPTER 4

RESULTS AND DISCUSSION

4.1 Introduction

This chapter discusses the results obtained from the FEM simulation and experiments that were conducted on ASTM A516 grade 70 steel in this sequence: the simulation result of residual stress relaxation, effects of shot peening process on the mechanical properties of the material, the initial residual stress induced by different shot peening process intensities, and the experimental relaxation of residual stress due to tensile cyclic loading. Additionally, the effects of the shot peening process on the material surface roughness were also assessed. Finally, the numerical and empirical model of residual stress relaxation of ASTM A516 grade 70 carbon steel were developed based on the results.

4.2 Experimental results

This subchapter discusses the variation in mechanical properties of the before and after the shot peening processes. The results include a tensile test, hardness test, fatigue test, and microstructure test using SEM. The discussion also includes the residual stress value induced by different shot peening intensities, the surface hardness reduction result due to cyclic loads applied to the material and the residual stress relaxation result due to cyclic loads applied to the material.

4.2.1 Tensile behaviour

Tensile test was performed to study the change in the tensile strength of the material due to the shot peening process. The tensile test was executed on raw material, shot peened with intensity 6.28 A and 12.9 A according to the standard ASTM E8 [11]. The test was done on 3 samples for each variant and the average value for stress-strain for each variant were calculated and plotted (Figure 4.1).

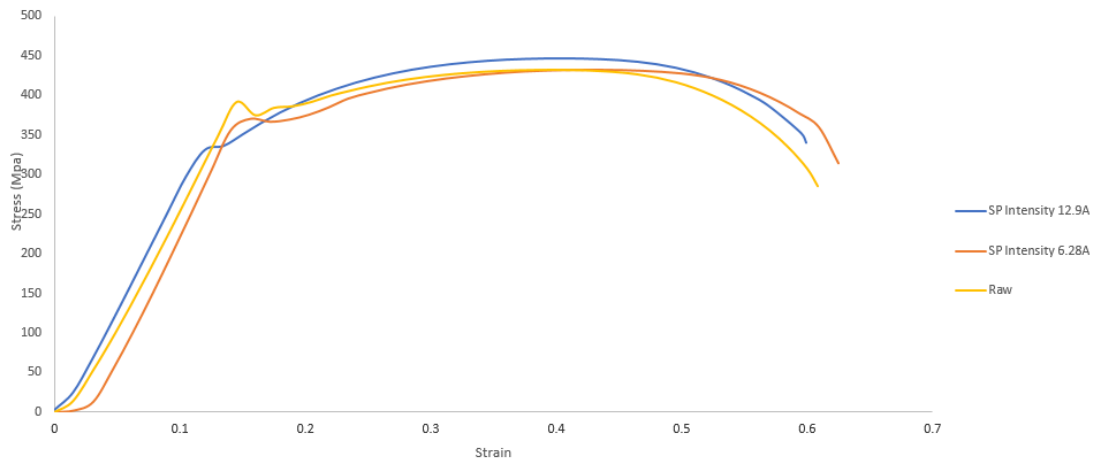


Figure 4.1 Stress-strain curve for raw material and shot-peened ASTM A516 grade 70 steel.

Based on the results obtained, raw material possessed the ultimate tensile strength (UTS) of 420 MPa. When the materials were shot peened with 6.28A intensity, the UTS value for this sample was recorded at 422 MPa, which was only 0.5% higher than that of the raw material. To the contrary, samples with shot peening intensity of 12.9A recorded a significant increase in the UTS value. The value of UTS for these samples was 450 MPa, 7.1% higher than the UTS of raw material.

Therefore, the UTS is higher when the materials were shot-peened with higher intensity. However, a similar pattern was not observed in terms of elongation. The elongation for materials shot-peened with higher intensity was slightly lower compared to the lower intensity shot peening and raw materials. As hardness increases, tensile strength also increases but the material becomes more brittle causing a smaller strain value. Figure 4.2 displays the broken sample after the tensile test. A necking region formed in the middle of the specimen before the specimen broke.

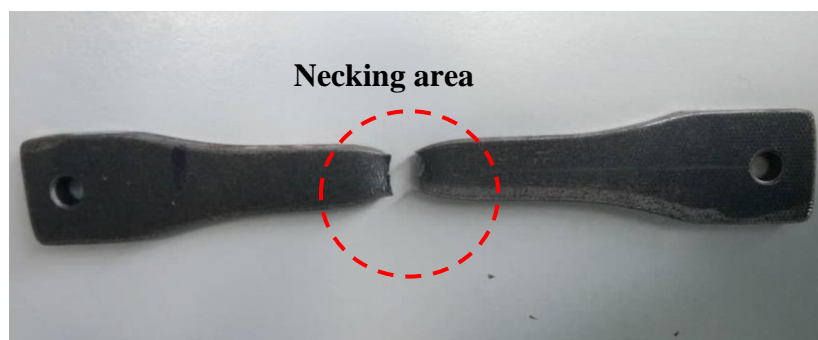


Figure 4.2 Broken sample after tensile test.

4.2.2 Hardness

Hardness test was performed to study the change in the surface hardness of the material due to the shot peening process. The hardness test was performed on raw material, shot peened with intensity 6.28 A and 12.9 A according to the standard ASTM E18 [12]. Table 4.1 summarises the results generated through the hardness test. The average value of hardness increased by 4.3% and 6.9% due to shot peening with 6.28 A and 12.9 A intensity, respectively.

Table 4.1 Rockwell hardness value of ASTM A516 Grade 70.

Number of measurement	Raw Material	Intensity 6.28A	Intensity 12.9A
1	75.4	84.5	81.5
2	81.3	82.0	83.0
3	77.1	84.5	85.4
4	79.9	85.5	91.7
5	81.4	78.0	86.0
6	80.3	87.5	86.0
7	80.2	83.0	84.1
8	80.6	81.0	85.3
9	79.4	87.5	83.0
10	77.8	73.5	80.5
Average	79.3	82.7	84.7

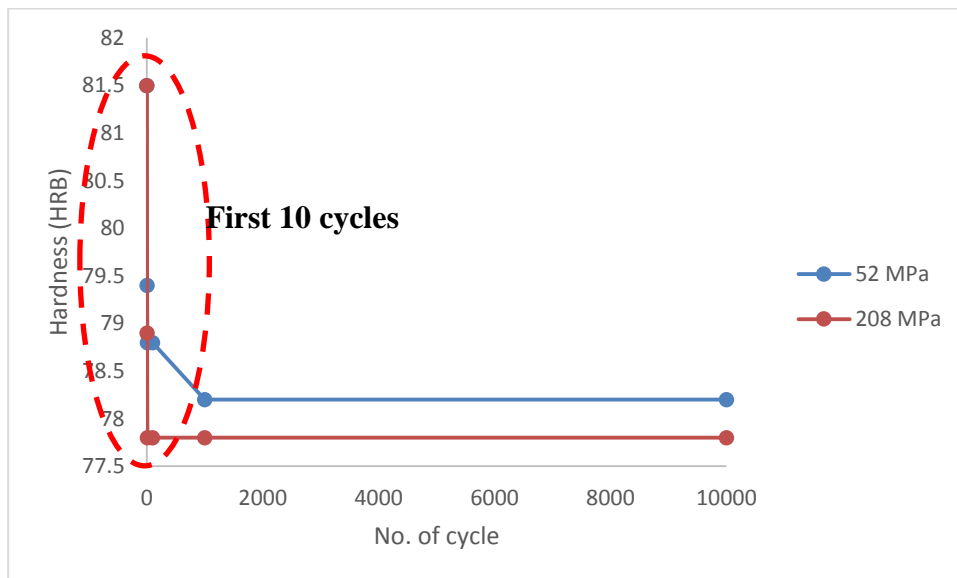
Hardness increases due to the change in dislocation and percentage of cold work of the material. By applying shot peening with higher intensity, dislocation occurs more rapidly and the material becomes harder [117].

In addition, to study the effects of cyclic loads on the hardness, further investigation was conducted. The relationship between these two variables is tabulated in Table 4.2.

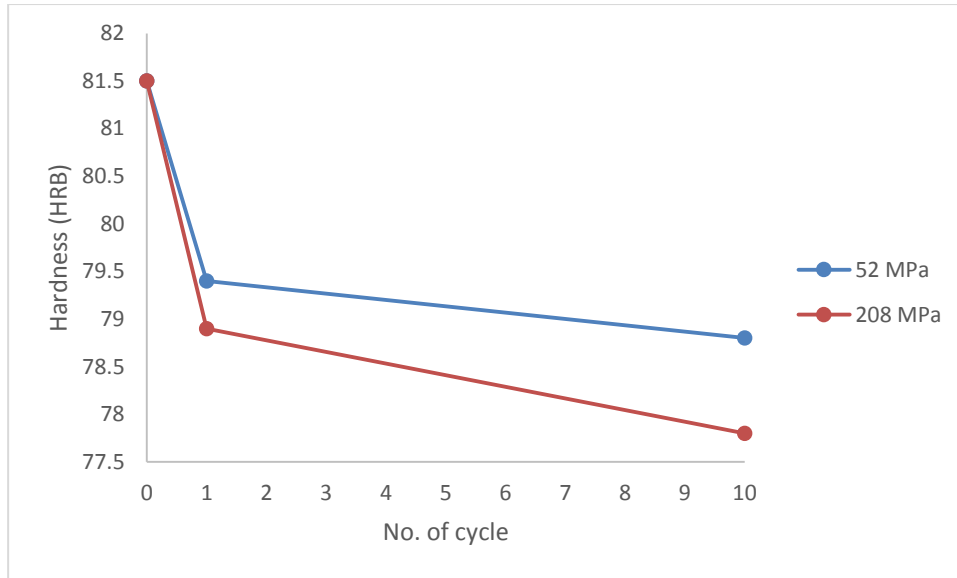
Table 4.2 Hardness reduction for shot-peened material by 6.28 A and 12.9 A intensities against cyclic load with 52 MPa and 208 MPa amplitudes.

Cycle/Load	Hardness (HRB)			
	Intensity 6.28 A		Intensity 12.9 A	
	52 MPa	208 MPa	52 MPa	208 MPa
0	82.7.	82.7	84.7	84.7
1	79.4	78.9	82.2	80.9
10	78.8	77.8	81.8	80.2
100	78.8	77.8	81.7	80.1
1000	78.2	77.8	80.7	79.9
10000	78.2	77.8	80.7	78.8

The values of hardness against the number of cycles were plotted to observe the trend more clearly. Figure 4.3 (a) for full region and; (b) low cyclic region demonstrates the plotted trend of hardness reduction against cyclic loading of 52 MPa and 208 MPa for shot-peened samples with 6.28 A intensity.



(a)



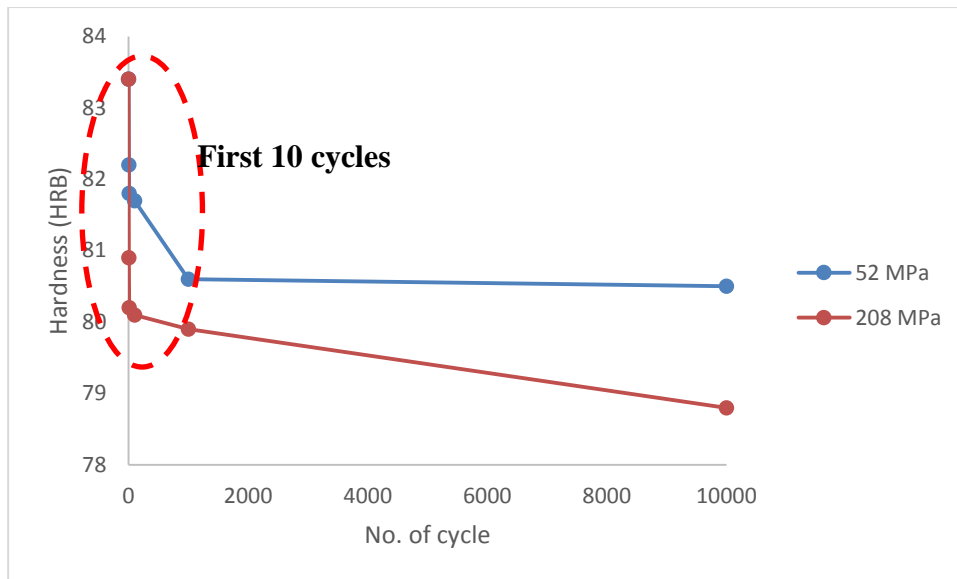
(b)

Figure 4.3 Hardness values against number of cycle for shot peening with intensity 6.28 A (a) 0 to 10,000 cycles (b) 0 to 10 cycles.

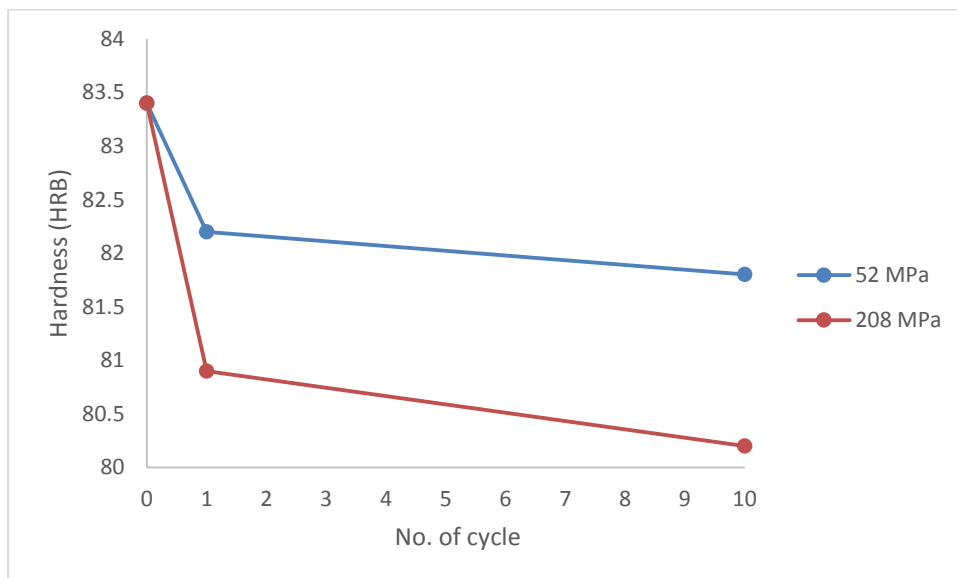
Based on the result from the hardness test of a low cyclic load of 52 MPa, the initial value of hardness was recorded at 82.7 HRB which experienced a reduction by 4% to 79.4 HRB in the first cycle. HRB continued to decrease by 0.76% in the tenth cycle to 78.8 HRB, where this value was maintained at 100 cycles. After 1000 cycles of 52 MPa loading, the hardness decreased by another 0.76% to 78.2 HRB. The value of hardness remained constant from 1000 to 10,000 cycles at 78.2 HRB.

However, by applying a higher load of 208 MPa, the initial value of hardness reduced by 4.6% from 82.7 HRB to 78.9 HRB, 0.6% more than the reduction by 52 MPa load amplitude. The hardness reduced by 1.4% from 78.9 HRB to 77.8 HRB after the tenth cycle. The value remained constant from 10 to 10,000 cycles at 77.8 HRB.

Figure 4.4 (a) and (b) demonstrates the hardness against number of cycles after being applied with 52 MPa and 208 MPa tensile cyclic loads shot-peened samples with 12.9 A intensity.



(a)



(b)

Figure 4.4 Hardness values against number of cycle for shot peening with intensity 12.9 A (a) 0 to 10,000 cycles (b) 0 to 10 cycles.

Based on the result from the hardness test of a low cyclic load of 52 MPa for samples shot peened with 12.9 A intensity, the initial value of hardness, 84.7 HRB, reduced by 2.95% to 82.2 HRB in the first cycle. It continued to decrease by 0.49% at the tenth cycle to 81.8 HRB. Followed by a reduction of 0.12% between 10 to 100 cycles from 81.8 HRB to 81.7 HRB. After 1000 cycles of 52 MPa loading, the hardness decreased by 1.22% to 80.7 HRB. The value of hardness remained constant from 1000 to 10,000 cycles at 80.7 HRB.

With a higher load of 208 MPa, the initial value of hardness reduced by 4.5% from 82.7 HRB to 80.9 HRB, 1.55% more than the reduction by 52 MPa load amplitude. After the tenth cycle, the hardness reduced by 0.87% from 80.9 HRB to 80.2 HRB. HRB reduced by only 0.12% between 10 to 100 cycles from 80.2 HRB to 80.1 HRB, similar to data from 52 MPa load. The value of hardness continued to drop further by 0.25% from 80.1 HRB to 79.9 HRB between 100 to 1000 cycles and by 1.38% from 79.9 HRB to 78.8 HRB between 1000 to 1000 cycles.

Therefore, in short, higher load significantly reduces the hardness of a material which agrees with [73]. High amplitude of external load would superpose more residual stress resulting in a smaller value of stress left under the material surface.

4.2.3 Fatigue behaviour

Fatigue test was conducted only on the SP A samples. This test was done to prove that the shot peening process increases the fatigue life. For this test, 85% and 75% of the UTS were treated as the maximum stress for the fluctuating load force to be applied on all specimens before and after shot peening.

For the samples before shot peening, the 85% UTS sample failed after 7 hours of applied cyclic load with a max elongation of 2.433 mm. The 75% took 9.4 hours with a max elongation of 3.195 mm. As for the samples after shot peening, the 85% UTS sample failed after 7.5 hours of applied cyclic load with a max elongation of 2.446 mm. While the 75% took 10 hours with a max elongation of 3.212 mm.

Table 4.3 summarises the final result for number of cycles before and after shot peening samples. The fatigue increased by an average of 6.78% in number of cycles before fatigue fracture shown in this test. This increment proved that the fatigue life of a material can be increased by the shot peening process. However, the slight increment in the fatigue life is again due to the instability of SP A process which reflects on the results of hardness and tensile test.

Table 4.3 Summary of fatigue test results before and after shot peening.

Parameters	Result	Before SP	After SP
85% of UTS (527 MPa)	Elongation (mm)	2.433	2.446
	Time (h)	7	7.5
	No. of cycle	252029	270032
75% of UTS (465 MPa)	Elongation (mm)	3.195	3.212
	Time (h)	9.4	10
	No. of cycle	338440	360005

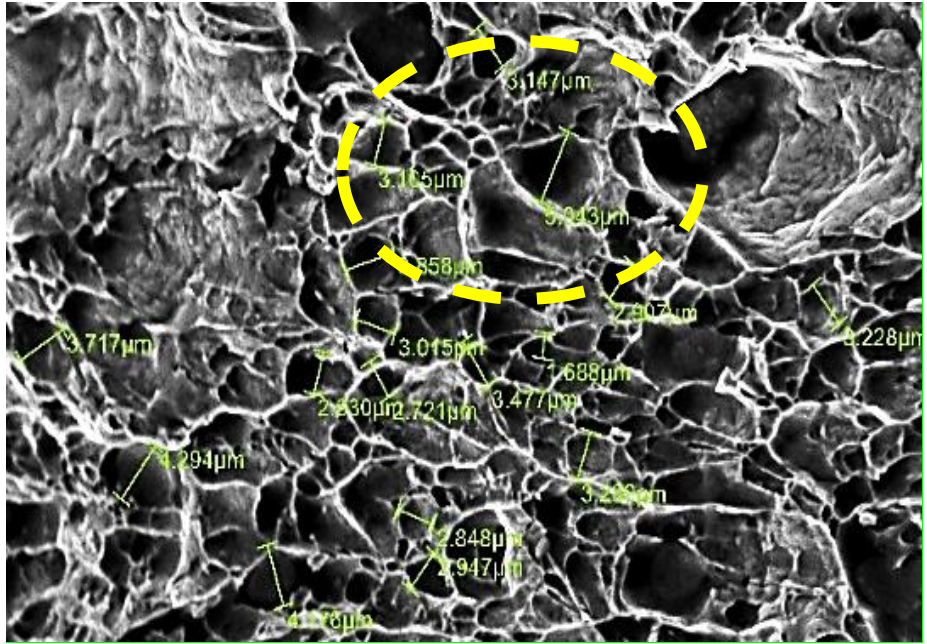
Fatigue life increases due to compressive residual stress (negative stress) on the surface which can encounter the external tensile stress (positive stress) applied to the samples. Higher intensity would increase the fatigue life. Although only one intensity was tested in this experiment, the enhancement in fatigue life still could be measured.

4.2.4 Microscopy test

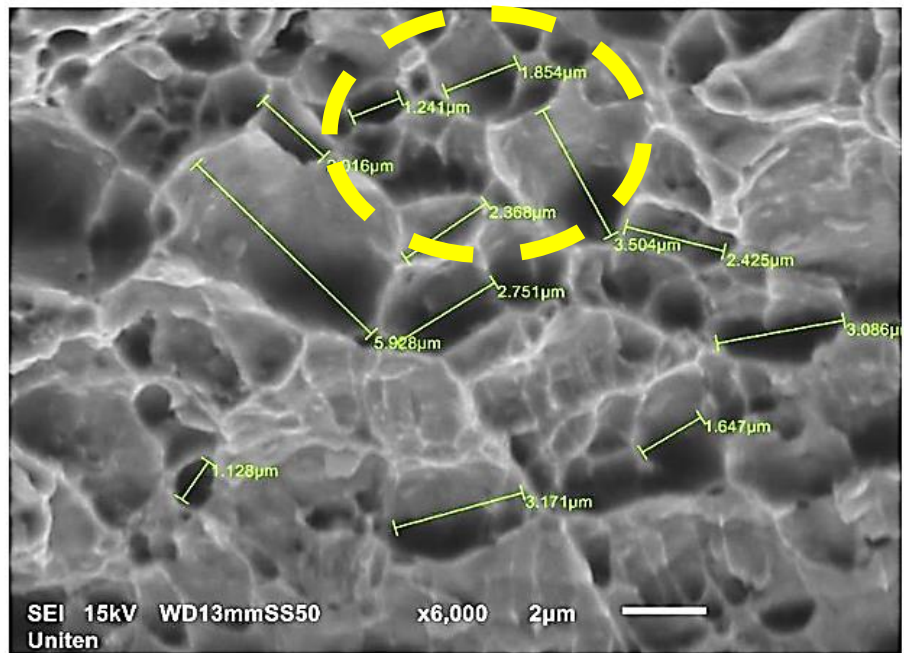
SEM was performed on raw and both shot-peened materials (SP A and SP B) to observe the effects of shot peening process on the microstructure of ASTM A516 Grade 70 carbon steel.

4.2.4.1 SEM of shot peening A

Based on the microstructure photos of the samples, it was observed that the molecules appeared closer to each other after shot peening. Shot peening process compresses the molecules closer to produce compressive residual stress in the surface of the material. Figure 4.5 (a) and (b) represents the microscopic view of the material before and after SP A.



(a)



(b)

Figure 4.5 Grain size of ASTM A516 Grade 70 microstructure. Tensile fracture before and after shot peening A (a) SEM before shot peening (b) SEM after shot peening.

By taking an area as a reference (see Figure 4.5 (a) and (b)), the size in molecules after shot peening decreased by 55.3%. The calculation is as following:

$$\text{Average size before SP} = \frac{3.147 + 3.105 + 5.943}{3} = 4.065 \mu\text{m}$$

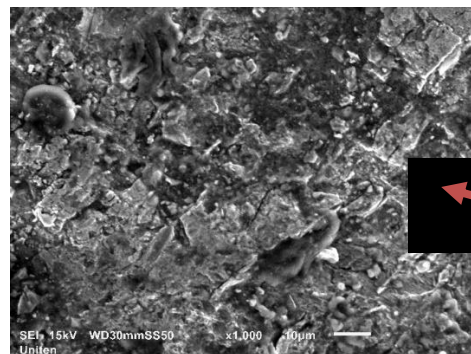
And

$$\text{Average size after SP} = \frac{1.241 + 1.845 + 2.368}{3} = 1.818 \mu\text{m}$$

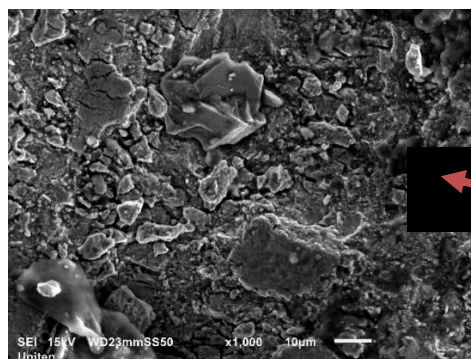
$$\text{The reduction percentage is } \frac{4.065 - 1.818}{4.065} \times 100\% = 55.3\%$$

4.2.4.2 SEM of shot peening B

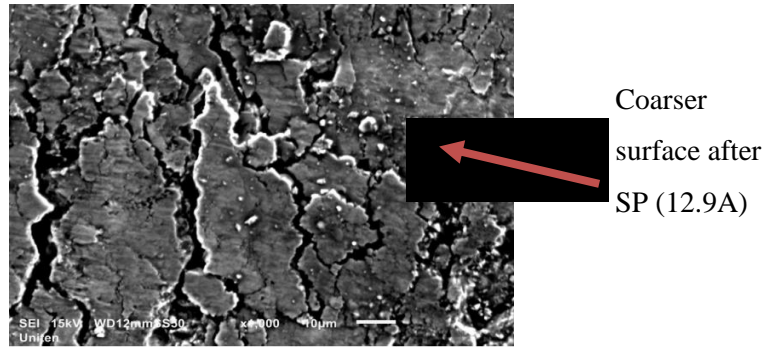
Morphological analysis was performed on raw samples without shot peening, SP B with intensities of 6.28 A and 12.9 A. Figure 4.6 (a); (b) and (c) displays the microstructure of each sample. It was observed that the molecules became coarser with higher intensity of the shot peening.



(a)



(b)



(c)

Figure 4.6 Grain size of ASTM A516 Grade 70 microstructure. Tensile fracture before and after shot peening B (a) SEM before shot peening (b) SEM after shot peening 6.28 A (c) SEM after shot peening 12.9 A.

4.2.5 Residual stress induced by shot peening process

The initial residual stress values introduced by the shot peening process with 6.28A and 12.9A intensities were 259 MPa and 273 MPa, respectively. Based on this result, it was stipulated that higher intensity can introduce higher compressive residual stress.

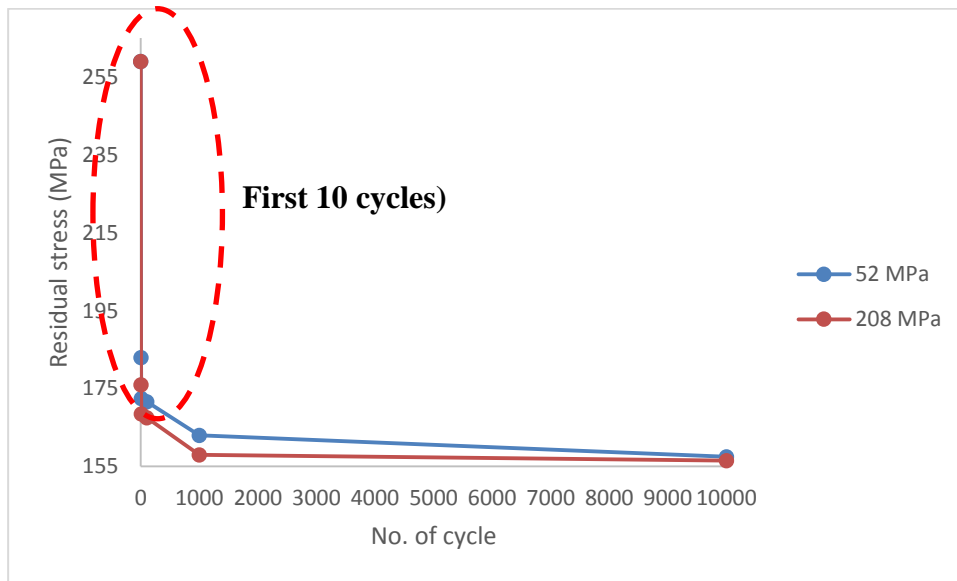
4.2.6 Residual stress relaxation against cyclic loading

Table 4.4 tabulates the data collection of XRD measurement for samples that were exposed to cyclic loads with shot peening intensity of 6.28 A.

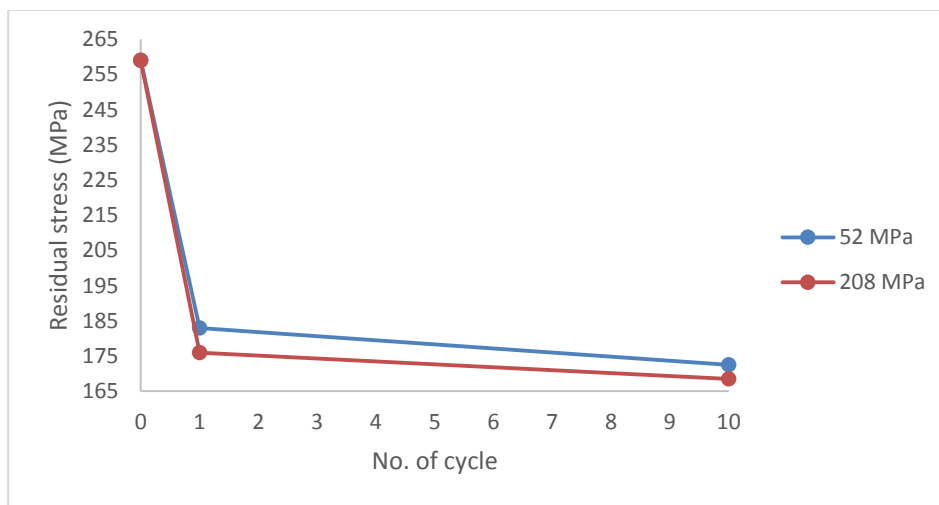
Table 4.4 Residual Stress after Cyclic Loads for shot-peened samples with intensity 6.28 A.

No. Of Cycle	Residual Stress	
	Load 52 MPa	Load 208 MPa
0	259	259
1	183	176
10	172.5	168.5
100	171.6	167.5
1000	163	158
10000	157.5	156.5

Figure 4.7 (a) and (b) represents the trend plotted for the high and low load applied on the samples that underwent a shot peening process with 6.28 A intensity against number of cycles.



(a)



(b)

Figure 4.7 Experimental residual stress relaxation against cyclic load for shot-peened material with intensity 6.28 A (a) 0 to 1000 cycles; (b) 0 to 10 cycles.

Similar to the simulation trend of relaxation, initial residual stress of 259 MPa induced by shot peening with 6.28 A intensity reduced by 29.3% to 183 MPa after the first cycle of 52 MPa tensile load. The residual stress then decreased by 10.5 MPa after the tenth cycle.

Based on the results from the residual stress against the low cyclic load of 52 MPa, the initial value of residual stress, 259 MPa, was reduced by 29.3% to 183 MPa in the first cycle. It continued to decrease by 5.7% in the tenth cycle to 172.5 MPa. Residual stress relaxed only by 0.52% from 172.5 MPa to 171.6 MPa between 10 to 100 cycles. The value further decreased by 5% from 171.6 MPa to 163 MPa between 100 to 1000 cycles. It relaxed by 3.37% from 163 MPa to 157.5 MPa between 1000 to 10,000 cycles.

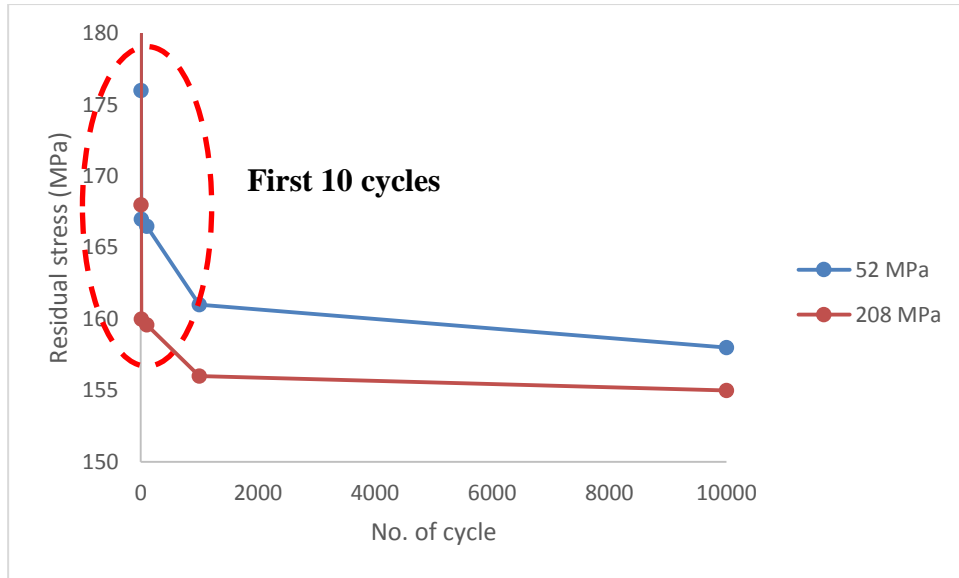
However, by applying a higher load of 208 MPa, the initial value of residual stress was reduced by 32% from 259 MPa to 176 MPa, 2.7% more reduced than that of the 52 MPa load amplitude. The residual stress relaxed by 4.26% from 176 MPa to 168.5 MPa after the tenth cycle. The value continued to decrease until 167.5 MPa at 100 cycles, only 0.59% less than the residual stress at the tenth cycle. It continued to decrease by 5.67% from 167.5 MPa to 158 MPa between 100 to 1000 cycles and by another 0.95% from 158 MPa to 156.5 MPa between 1000 to 10,000 cycles.

Table 4.5 represents the data collection of XRD measurement for samples that had undergone cyclic loads with shot peening intensity of 12.9A.

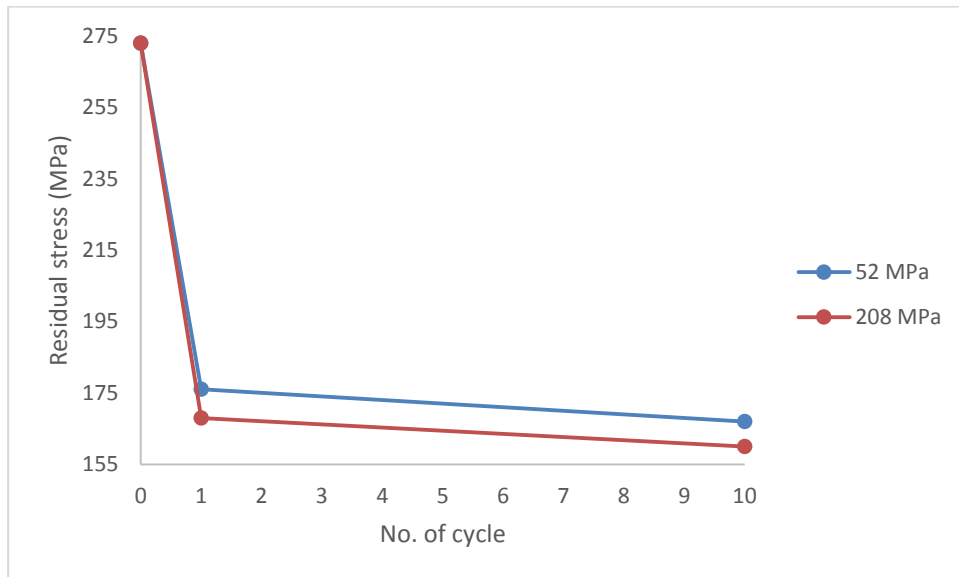
Table 4.5 Residual Stress after Cyclic Loads for shot-peened samples with intensity 12.9 A.

No. Of Cycle	Residual Stress	
	Load 52 MPa	Load 208 MPa
0	273	273
1	176	168
10	167	160
100	166.5	159.6
1000	161	156
10000	158	155

Figure 4.8 displays the trend plotted for the high and low load applied to the samples that had undergone shot peening with 12.9 A intensity against number of cycles.



(a)



(b)

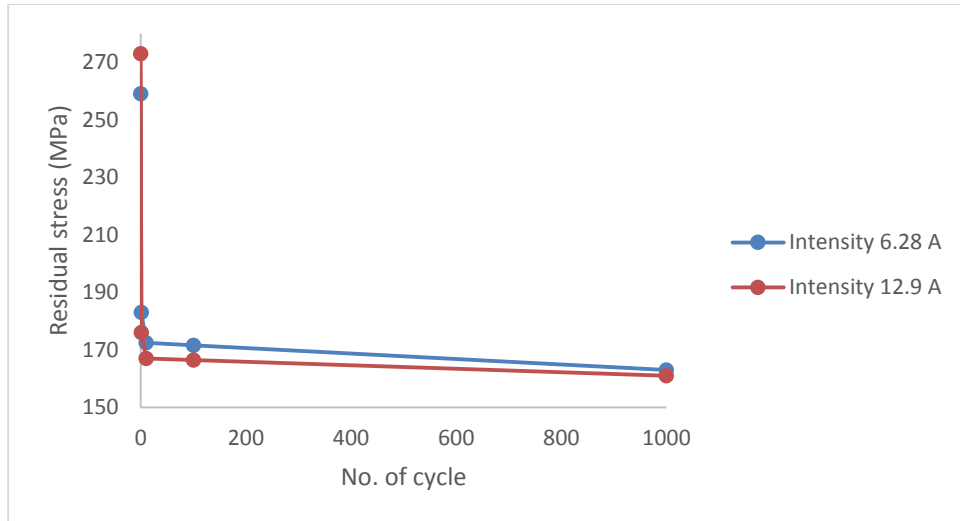
Figure 4.8 Experimental residual stress relaxation against cyclic load for shot-peened material with intensity 12.9 A (a) 0 to 1000 cycles; (b) 0 to 10 cycles.

Based on the results from the residual stress against a low cyclic load of 52 MPa, the initial value of residual stress which was recorded at 273 MPa, reduced by 35.5% to 176 MPa in the first cycle. It continued to decrease by 5.1% at the tenth cycle from 176 MPa to 167 MPa and by another 0.3% from 167 MPa to 166.5 MPa between 10 to 100 cycles. The value decreased further by 3.3% from 166.5 MPa to 161 MPa between 100 to 1000 cycles. It relaxed by 1.86% from 161 MPa to 158 MPa between 1000 to 10,000 cycles.

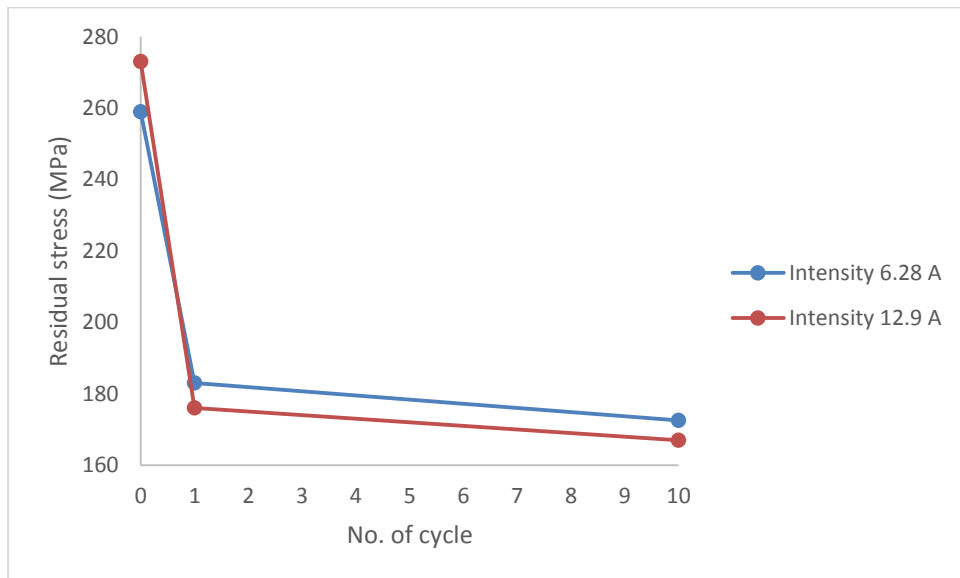
However, by applying a higher load of 208 MPa, the initial value of residual stress reduced by 38.5% from 273 MPa to 168 MPa, 3% more reduced than the 52 MPa load amplitude. The residual stress relaxed by 4.8% from 168 MPa to 160 MPa after the tenth cycle. The value continued to decrease until 159.6 MPa at 100 cycles, 0.25% less than the residual stress at the tenth cycle. It continued to decrease by 2.26% from 159.6 MPa to 156 MPa between 100 to 1000 cycles and by another 0.64% from 156 MPa to 155 MPa between 1000 to 10,000 cycles.

Based on the results, the relaxation of residual stress increases by applying a higher load. It is observed that materials are most reduced during the lower cycle region, especially during the first few cycles (cycle 1 to cycle 10). Concurrently, high load amplitude could also cause more relaxation compared with lower load amplitude. Hence, it was concluded that the relaxation of the residual stress increases by increasing the applied load due to quasi-static relaxation effect. Previous literature explained the relaxation of residual stress using the theory of Bauschinger's effect. This theory states the work hardened surface yield in compression during the compressive part of the initial cycle [148]. Residual stress relaxation may occur after the few low cycles due to micro-plastic strain accumulating from cycle to cycle. As such, the increase in residual stress relaxation can be related to an increasing number of cycles and applied load.

Other than comparison of the relaxation of residual stress due to different cyclic load amplitudes, comparison of relaxation of residual stress due to different shot peening intensities on ASTM A516 grade 70 steel for the same cyclic load amplitude was also conducted. The purpose is to investigate if the shot peening intensity influences the reduction value of the initial residual stress when two different load amplitudes are applied (52 MPa and 208 MPa). Figure 4.9 (a) and (b) show the graphs for residual stress against number of cycle after being applied with 52 MPa tensile cyclic loads on shot-peened ASTM A516 grade 70 carbon steel with intensities 6.28 A and 12.9 A.



(a)

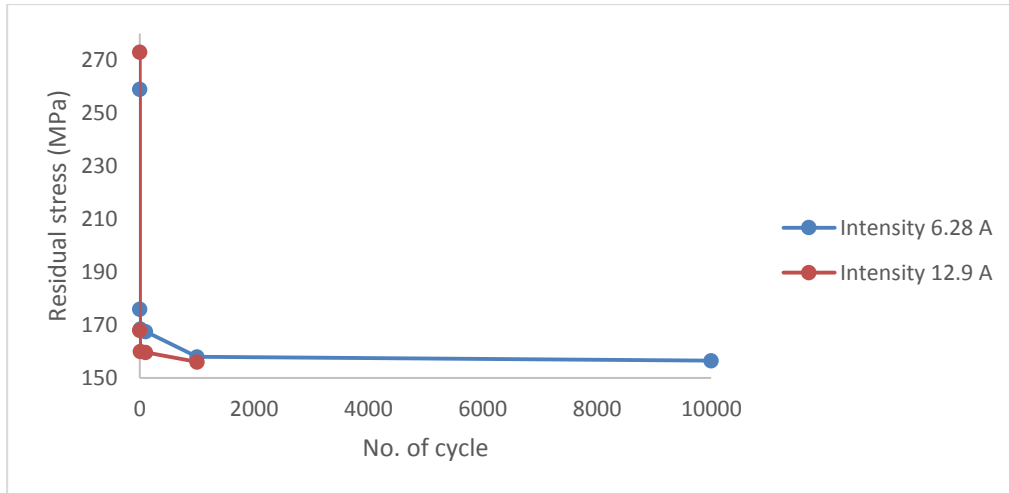


(b)

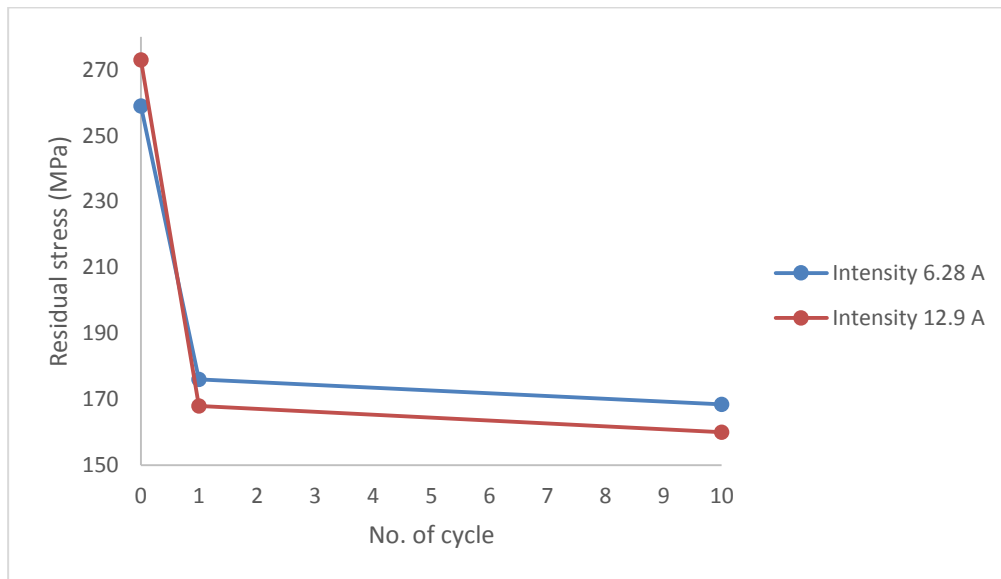
Figure 4.9 Residual stress relaxation against cyclic loading with amplitude of 52 MPa for intensities 6.28 A and 12.9 A (a) 0 to 1000 cycles; (b) 0 to 10 cycles.

Based on the result from the simulation of low cyclic load of 52 MPa, the trend shows agreement with previous study by [139] where higher intensity of shot peening causes more relaxation of residual stress during operation. This can be observed in Figure 4.10 (a) and (b) where the values of residual stress for intensity 12.9 A is lower in every cycle in comparison with intensity 6.28 A. For the first cycle, the reduction of residual stress value after being applied with 52 MPa is 29.3% for intensity 6.28 A and 35.5% for intensity 12.9 A. By the end of 10,000th cycle, the total reduction is 39.2% for intensity 6.28 A and 42.1% for intensity 12.9 A.

On the other hand, same analysis was done on 208 MPa applied on two different intensities (6.28 A and 12.9 A). Figure 4.21 (a) and (b) shows the graphs for residual stress against number of cycle after being applied with 208 MPa tensile cyclic loads on shot-peened ASTM A516 grade 70 carbon steel with intensities 6.28 A and 12.9 A.



(a)



(b)

Figure 4.10 Residual stress relaxation against cyclic loading with amplitude of 208 MPa for intensities 6.28 A and 12.9 A (a) 0 to 1000 cycles; (b) 0 to 10 cycles.

Based on the result from the simulation of low cyclic load of 52 MPa, the trend also shows agreement with previous study by [139] where higher intensity of shot peening causes more relaxation of residual stress during operation. This can be observed in Figure 4.10 (a) and (b) where the values of residual stress for intensity 12.9 A is lower in

every cycle in comparison with intensity 6.28 A. For the first cycle, the reduction of residual stress value after being applied with 208 MPa is 32% for intensity 6.28 A and 38.5% for intensity 12.9 A. By the end of 10,000th cycle, the total reduction is 39.6% for intensity 6.28 A and 43.2% for intensity 12.9 A.

4.2.7 Surface roughness

This test was conducted on raw material, samples shot peened with 6.28A and 12.9A intensities. Table 4.6 indicates the surface roughness value for each sample. It was observed that the shot peening process was able to roughen the surface of the material. Similarly, the higher intensity will also produce a rougher material surface. Due to the impact of bigger steel ball size, the surface became dented with a bigger diameter. This dented region is a representation of resulting rough surface.

Table 4.6 Surface roughness result before and after SP B.

Sample	5DP
Raw material	3.202
Intensity 6.28A	6.990
Intensity 12.9A	14.500

4.2.8 Empirical modelling of residual stress relaxation

The empirical residual stress relaxation model was developed from experimental data based on the best curve-fitting (Equation 4.1).

$$\sigma_R = EN^F \quad (4.1)$$

where E and F are constants depending on the shot peening intensity and the amplitude of applied tensile stress. The values were also differentiated into low and high cyclic regions. The values for E and F are tabulated in Table 4.7 and Table 4.8 for intensities 6.28 A and 12.9 A respectively.

Table 4.7 Constant values of residual stress relaxation shot peening with intensity 6.28 A.

Load Applied	Low cyclic region		
	E	F	R ²
52 MPa	187.85	-0.046	0.9885
208 MPa	183.06	-0.049	0.9775
	High cyclic region		
52 MPa	186.43	-0.019	0.9869
208 MPa	177.82	-0.015	0.8530

Table 4.8 Constant values of residual stress relaxation shot peening with intensity 12.9 A.

Load Applied	Low cyclic region		
	E	F	R ²
52 MPa	183.79	-0.056	0.9791
208 MPa	177.0	-0.061	0.9747
	High cyclic region		
52 MPa	175.03	-0.011	0.9742
208 MPa	163.89	-0.006	0.9053

As for hardness, another empirical model was developed for the low cyclic region (Equation 4.2):

$$H = GN^h \quad (4.2)$$

where C and D are constants depending on the shot peening intensity and the amplitude of applied tensile stress.

Equation 4.3 is the model developed for hardness in the high cyclic region.

$$H = I.N + J \quad (4.3)$$

Where I and J are also constants depending on the shot peening intensity and the amplitude of applied tensile stress. The values for G, h, I and J are tabulated in Table 4.9 and 4.10.

Table 4.9 Constant values of hardness reduction constants in low cyclic region for shot peening with intensity 6.28 A and 12.9 A.

Load Applied	Intensity 6.28 A		
	G	h	R ²
52 MPa	79.62	-0.005	0.9908
208 MPa	78.96	-0.007	0.9995
	Intensity 12.9 A		
52 MPa	82.394	-0.004	0.9873
208 MPa	81.147	-0.006	0.9912

Table 4.10 Constant values of hardness reduction constants in high cyclic region for shot peening with intensity 6.28 A and 12.9 A.

Load Applied	Intensity 6.28 A		
	I	J	R ²
52 MPa	-4×10^5	78.533	0.3243
208 MPa	0	77.8	1
Intensity 12.9 A			
52 MPa	-8×10^5	81.217	0.3964
208 MPa	-0.0001	80.072	0.9963

The equation of residual stress relaxation and hardness against the number of cycles can be integrated to generate a new empirical model including initial residual stress, σ_0 residual stress at any cycle, σ_{RN} and hardness, H. For low cyclic region i.e. number of cycle 10 and below, Equation 4.4 is applicable.

$$\frac{\sigma_{RN}}{\sigma_{R_0}} = \frac{E \left(\frac{H}{G}\right)^{F/h}}{\sigma_{R_0}} \quad (4.4)$$

Equation 4.4 can be simplified into Equation 4.5.

$$\frac{\sigma_{RN}}{\sigma_{R_0}} = K \cdot \left(\frac{H}{G}\right)^{F/h} \quad (4.5)$$

where σ_{R_0} is the initial residual stress induced on the surface of material due to shot peening process and K is calculated as in Equation 4.6.

$$K = \frac{E}{\sigma_{R_0}} \quad (4.6)$$

E, F, G and h are constants depending on the shot peening intensity and the amplitude of the cyclic load applied on the sample. In summary, the values for E, F, G and h are as tabulated in Table 4.16.

Table 4.11 Values for constant E, F, G and h for low cyclic region model.

Shot Peening Intensity	Load Applied	E	F	G	h
S110 (6.28A)	52 MPa	186.43	-0.019	79.62	-0.005
	208 MPa	177.82	-0.015	78.96	-0.007
S230 (12.9A)	52 MPa	175.03	-0.011	82.394	-0.004
	208 MPa	163.89	-0.006	81.147	-0.006

The equation of residual stress relaxation and hardness against high cyclic region (number of cycle 10 and above) is represented as Equation 4.7.

$$\frac{\sigma_{RN}}{\sigma_{R_0}} = \frac{E \left(\frac{H - J}{I} \right)^F}{\sigma_{R_0}} \quad (4.7)$$

Equation 4.9 can be simplified to equation 4.8.

$$\frac{\sigma_{RN}}{\sigma_{R_0}} = L \cdot \left(\frac{H - J}{I} \right)^F \quad (4.8)$$

where σ_{R_0} is the initial residual stress induced on the surface of material due to shot peening process and L is calculated using Equation 4.9.

$$L = \frac{E}{\sigma_{R_0}} \quad (4.9)$$

E, F, I and J are constants depending on the shot peening intensity and the amplitude of the cyclic load applied on the sample. In summary, the values for E, F, I and J are as tabulated in Table 4.12.

Table 4.12 Values for constant E, F, I and J for high cyclic region model.

Shot Peening Intensity	Load Applied	E	F	I	J
S110 (6.28A)	52 MPa	186.43	-0.019	-4×10^5	0.3243
	208 MPa	177.82	-0.015	0	1
S230 (12.9A)	52 MPa	175.03	-0.011	-8×10^5	0.3964
	208 MPa	163.89	-0.006	-0.0001	0.9963

Accordingly, Equation 4.7 can be used to calculate the residual stress values in low cycle region and Equation 4.10 can be used to calculate the residual stress values in high cycle region. By having these equation, the hardness values can be used to determine the residual stress values.

4.3 Simulation results

The simulation result that was conducted using Hyperworks software were presented in this part. The simulation result is divided into two parts. The first one is to present the simulation result of the process to induce the residual stress namely the shot peening process. The shot peening simulation introduces initial residual stress on the surface of ASTM A516 grade 70 carbon steel material. The first part of shot peening simulation discusses on the determination of the shot speed since it is initially unknown. The result of shot peening is used as the initial residual stress. Secondly the residual stress generated from shot peening simulation is used in residual stress relaxation simulation when cyclic load is applied.

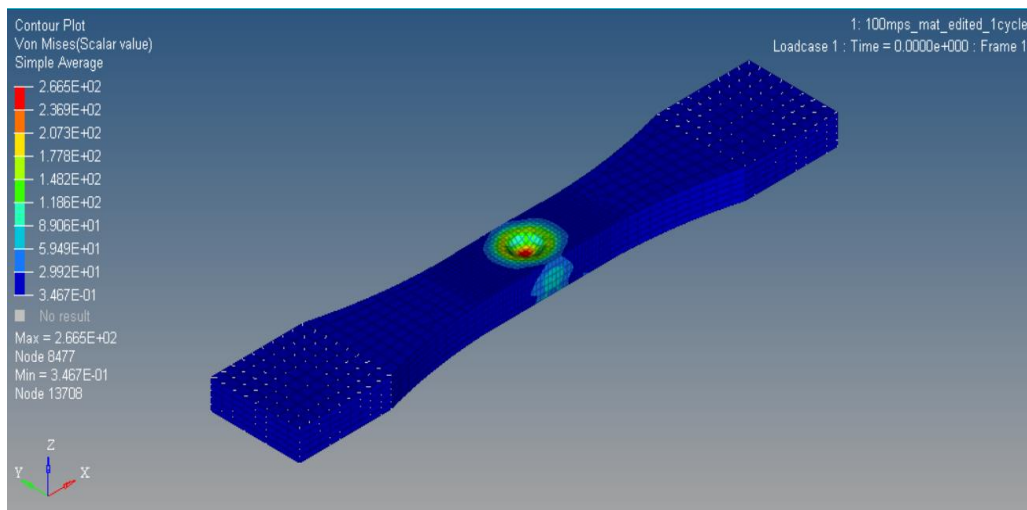
4.3.1 Shot peening simulation result

Shot peening simulation was done using Hyperworks software. To simulate shot peening, many parameters are involved, such as shot angle, shot size and shot speed. For this study the angle is fixed at 90 degree and shot size is set at 10 mm of steel with Young modulus of 200 GPa. The shot speed is increased gradually to get the initial residual stress value close to the actual residual stress induced by experimental. The parameters are not equal with the experiment, due to the usage of single impact model. The main purpose is to introduce the initial residual stress value which is equivalent to the experimental value as explained in subchapter 3.3.4.

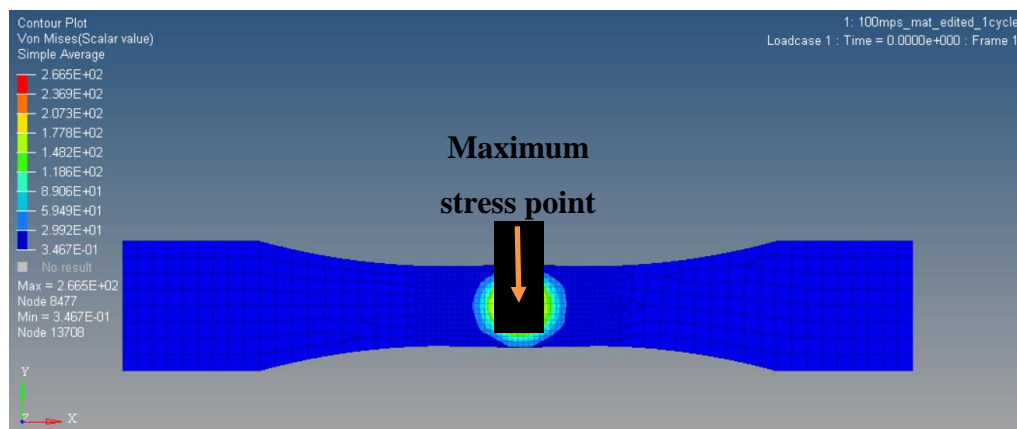
The initial speed exerted on the ball to hit the sample was 2 m/s. The selection of the speed is based on the experimental setup which the nozzle speed of 0.1 m/s only. Since the selected speed during the simulation did not produce the expected residual stress in comparison with the expected value from the experimental result, the speed of the ball was increased. The speed is increased to compensate other fix parameters (shot angle and shot size). The speed is increased to 5 m/s, 25 m/s, 50 m/s and 100 m/s. The residual stress resulted from each speed is depicted in Table 4.13, while Figure 4.11 shows the isometric view (a) and top view (b) of the stress distribution on the impacted area. The stress distribution could be observed that the maximum stress is in the middle of the impacted area.

Table 4.13 Residual stress values for each shot speed.

Shot Speed (m/s)	Residual Stress (MPa)
2	19.91
5	36.94
25	75.35
50	135.30
100	266.5



(a)



(b)

Figure 4.11 Result of simulation of shot peening (a) 3D view (b) Top view. The colour contours represent the different values of the stress. Red for the maximum stress where the highest impact occurred. Followed by the other colours in a descending pattern (orange, yellow, greens and blues).

Based on the results, the most suitable shot speed to introduce the similar amount of residual stress during the experimental shot peening process with intensities of 6.28 A and 12.9 A was 100 m/s (Table 4.1). Using the shot speed of 100 m/s, the initial residual stress values were estimated between 259 MPa and 273 MPa for intensities 6.28A and 12.9 A respectively (266.5 MPa). Figure 4.12 illustrates the depth of the dented area upon the impact (between the ball and the specimen). The depth measured was 2.017 mm which is approximately 1/3 of the specimen thickness (Figure 4.12). Figure 4.13 depicts the diameter of the dented area which is 7.190 mm.

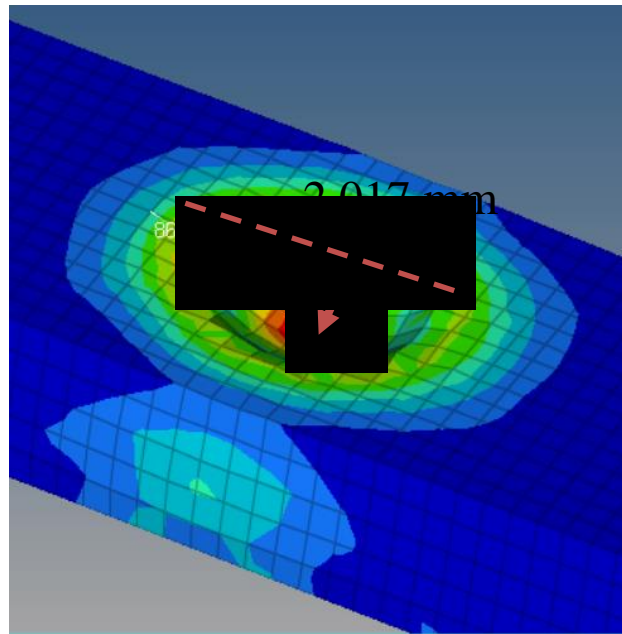


Figure 4.12 Depth measurement of the dented area after impact.

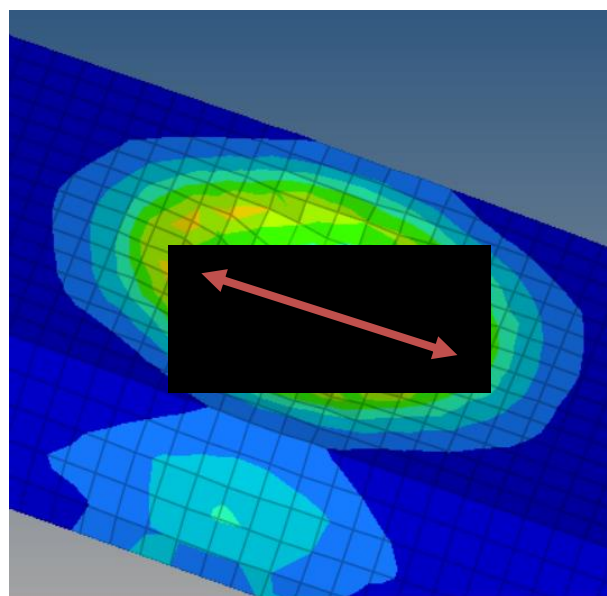


Figure 4.13 Diameter measurement of the dented area after impact.

4.3.2 Mesh convergence result

Conducting shot peening simulation needs meshing process to be done on the solid model. To identify the number of meshing element to be used in the shot peening and result stress simulation several models with different number of elements were created. The purpose is to determine the right number of meshing element known as mesh convergence study. The number of meshing element is started with 61,237 elements, which resulted in initial residual stress of 279.63 MPa. The number of meshing elements were increased gradually. Accordingly, increasing the number element resulted the change in residual stress. As the number of elements is increased, the change in initial residual stress becomes minor. The number of element is selected when the initial residual stress starts to become consistent. Five models of meshing elements were produced and the results from the mesh sensitivity are summarized in Table 4.14.

Based on the results, Model 1 recorded the maximum stress value at 279.63 MPa with 61,237 elements. By increasing the number of elements in Model 2 by approximately 2% to 62,337, the maximum stress value dropped by 3% to 270.85 MPa. An increase by another 1600 elements in Model 3 decreased the maximum stress value by 1.6% to 266.45 MPa. Model 4 with a total of 71,498 elements, which is approximately 12% more than Model 3 recorded a decrease in the maximum stress value by 0.2% to 265.80 MPa. The value of maximum stress was becoming constant at 63,937 elements. To verify this assumption, additional 7,370 elements were added in Model 5 with a total of 78,868 elements. The value of maximum stress only decreased by 0.6% from 265.80 MPa to 264.10 MPa. Based on the results obtained from each model, a graph of stress value against the number of elements was plotted (Figure 4.14).

Table 4.14 Mesh convergence study result.

	No of elements	End stress result (MPa)
Model 1	61237	279.63
Model 2	62337	270.85
Model 3	63937	266.48
Model 4	71498	265.80
Model 5	78868	264.10

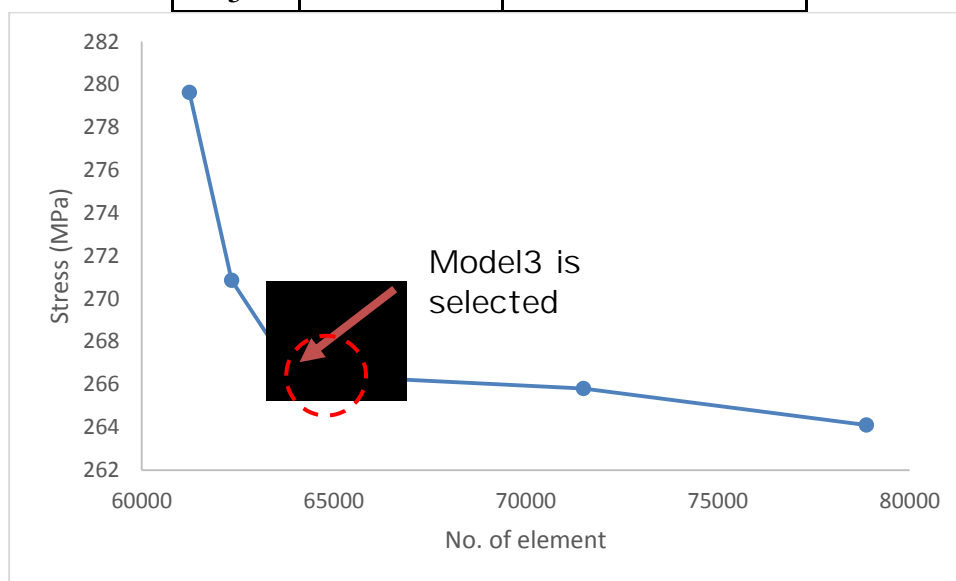


Figure 4.14 Graph of stress value against number of element for the mesh convergence study.

Since Model 3 with 63,937 elements was the starting point for the value of stress to become consistent, Model 3 was therefore selected to be used for the shot peening and relaxation of residual stress simulation. The selection of Model 3 over Model 4 and Model 5 is due to simulation (computational) time consumption as well as the result of Model 3 is not so much different compared to Model 4 and Model 5.

4.3.3 Residual stress relaxation simulation result

The initial stress value was transferred (mapped) for the shot peening simulation and the cyclic load simulation. The mapped model is illustrated in Figure 4.15. The impact area on the surface was caused by the ball shot during the shot peening simulation yielding an initial stress value of 266.5 MPa. The coding of the simulation can be referred in Appendix A.

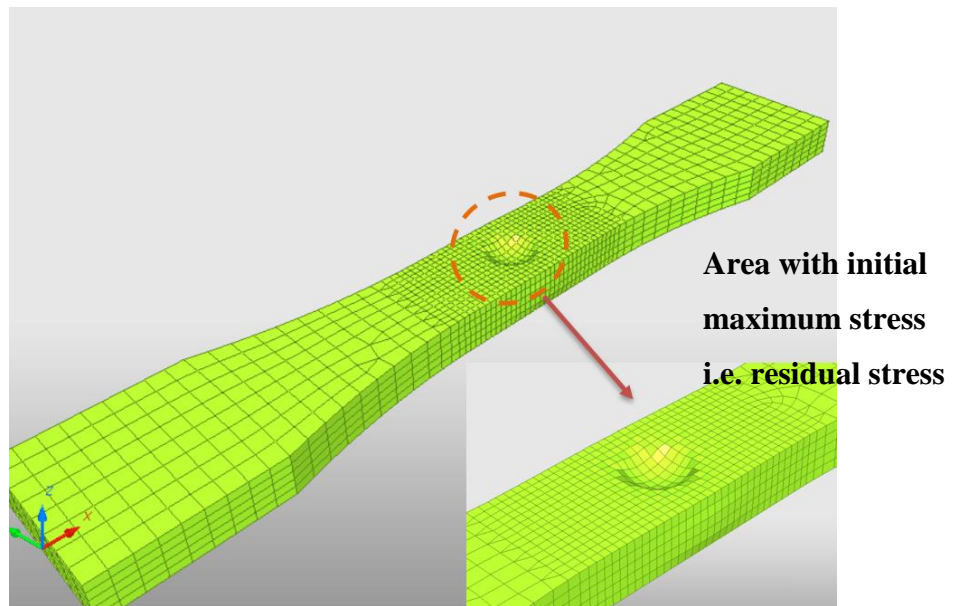


Figure 4.15 Model used in relaxation of residual stress simulation.

The maximum initial residual stress value of 266.5 MPa was measured at node 8477. The same node was measured at the end of the simulation after the cyclic load was applied and released. This node represents the centre area of the sample. Figure 4.16 shows the point of residual stress measurement.

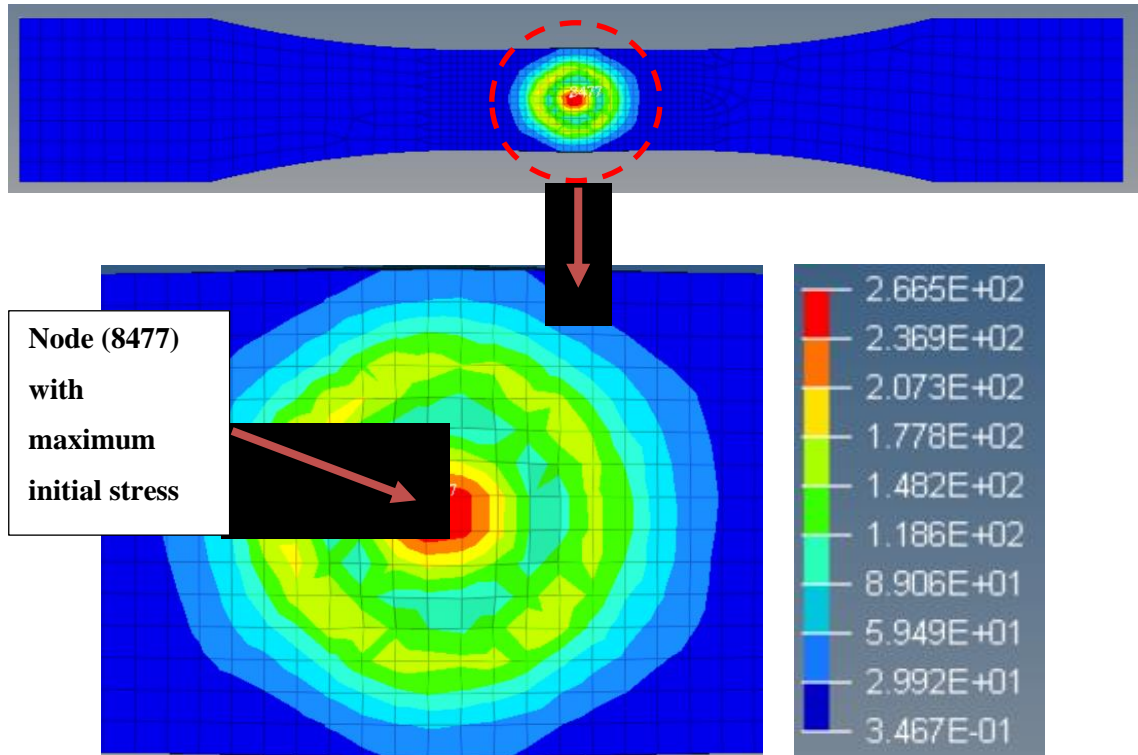
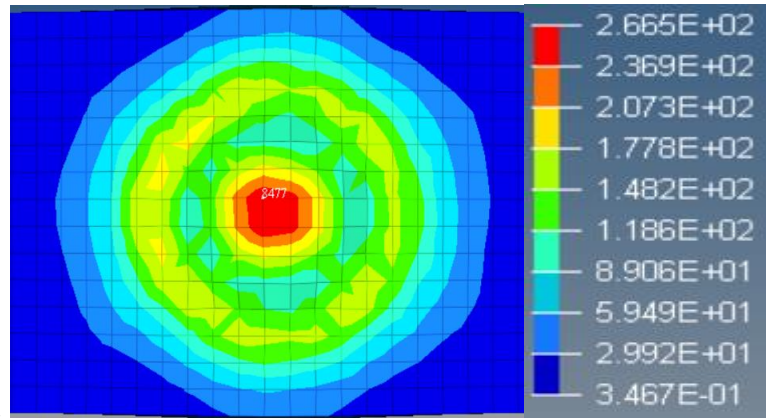
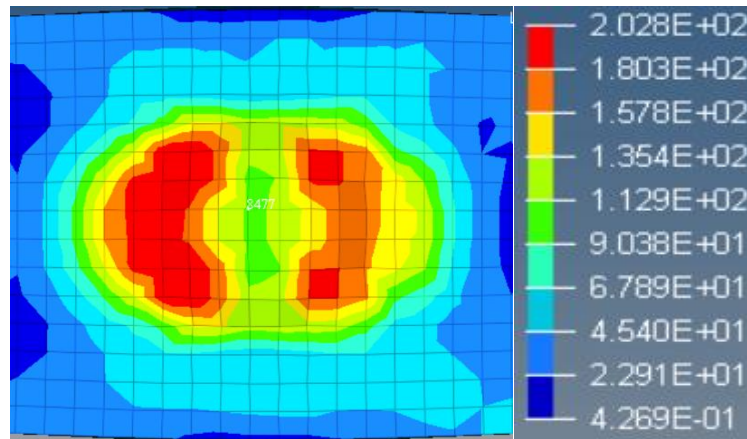


Figure 4.16 Point of measurement with maximum residual stress value (node 8477).

Residual stress relaxation simulation was done for two different amplitude of cyclic loads (52 MPa and 208 MPa). As explained in Chapter 3 (subchapter 3.3.5), these values were obtained from 20% of Yield Strength and 80% of Yield Strength of the material. For each load, simulation has been conducted for different number of cycles namely 1, 2, 5, 10, 100, 200, 500 and 1000. The result at the node before and after the applied load were measured. Based on the observation of the stress area, it was visible that the initial residual stress was distributed after the first cycle. However, the measurement of the same node with maximum initial stress prior to the commencement of the simulation indicated a decrease in the value of stress. Figure 4.17 displays the stress area (a) before and (b) after cyclic loads applied on the model after one cycle. Figure 4.17 (b) shows the residual stress is re-distributed and it decreased in the middle area and this is due to the starting of cyclic load is in tension (pulling) which allow the stress to redistribute and decrease in the middle of the measuring point (node 8477).



(a)



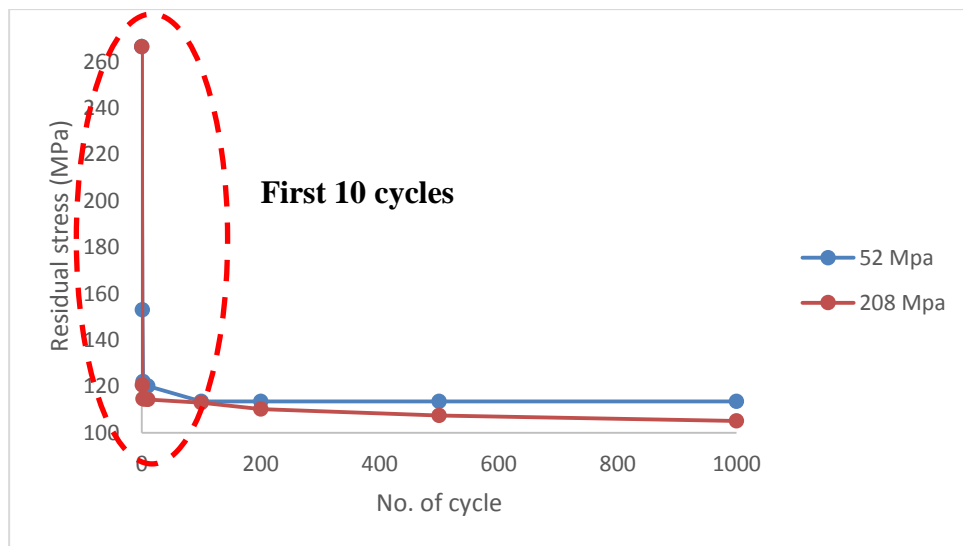
(b)

Figure 4.17 Stress distribution (a) before and (b) after cyclic load applied (1 cycle).

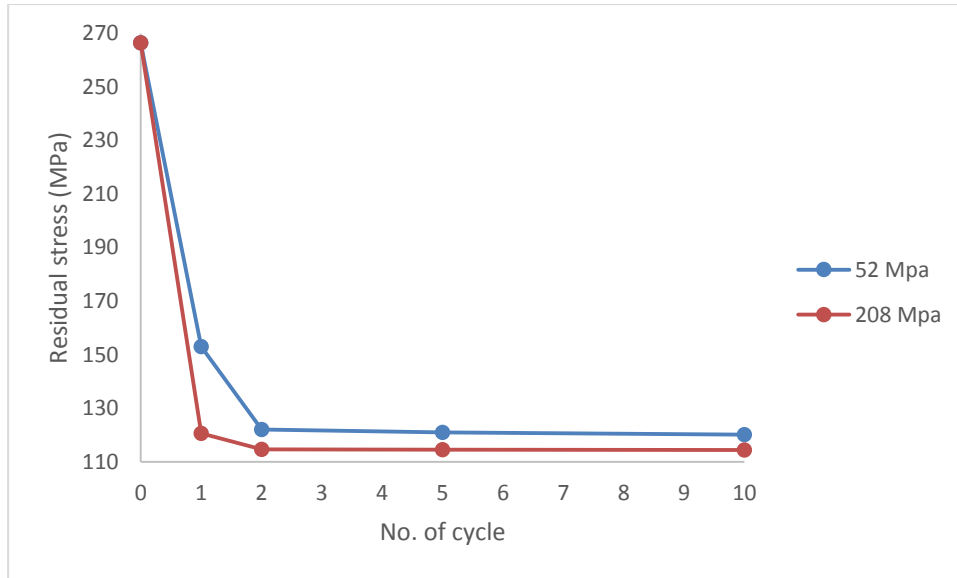
Table 4.15 represents the residual stress values once cyclic loads were applied to the samples. Moreover, Figure 4.18 (a) and (b) demonstrate the residual stress against number of cycles after being applied with 52 MPa and 208 MPa tensile cyclic load on shot-peened samples with an intensity of 6.28 A.

Table 4.15 Simulation result of residual stress values against cyclic loads for intensity 6.28 A and 12.9A.

No. of cycle	Intensity 6.28 A		Intensity 12.9 A	
	52 MPa	208 MPa	52 MPa	208 MPa
0	266.5	266.5	266.5	266.5
1	153.0	120.6	132.9	122.5
2	122.1	114.7	128.0	117.2
5	121.0	114.5	127.6	116.8
10	120.2	114.4	127.3	115.9
100	113.6	113.0	127.2	115.5
200	113.6	110.2	126.9	115.4
500	113.6	107.5	126.7	115.3
1000	113.6	105.2	126.0	115.0



(a)



(b)

Figure 4.18 Residual stress relaxation against cyclic loading with amplitude of 52 MPa and 208 MPa for intensity 6.28 A (a) 0 to 1000 cycles; (b) 0 to 10 cycles

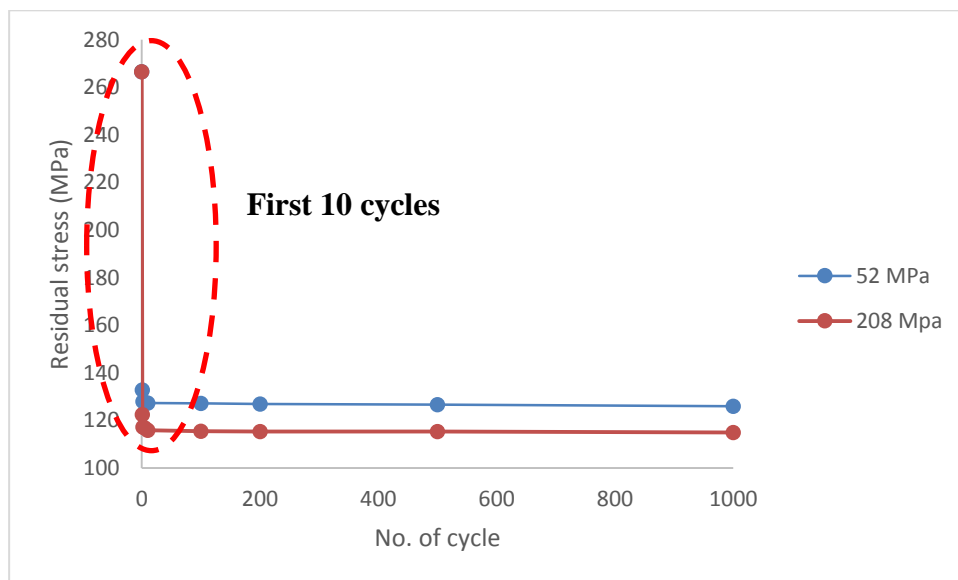
Based on the results, the initial value of residual stress was reduced by 42.6% from 266.5 MPa to 153 MPa after the first cycle for the simulation of a low cyclic load of 52 MPa (20% of the Yield Strength of the material). After the second cycle, the value of residual stress of 153 MPa dropped by another 20.2% to 122.1 MPa. At the tenth cycle, the value further dropped by 1.6%. However, from 100 cycles to 1000 cycles, the residual stress value which decreased by 5.5% (6.6 MPa) from the tenth cycle remained constant at 113.6 MPa throughout the end of the simulation. In overall, the total reduction of residual stress at 1000 cycle from initial residual stress by 57.4% from 266.5 MPa to 113.6 MPa. Out of this 57.4%, there are 42.6% only during the first cycle. 14.8% relaxation occurred from second cycle to 1000 cycle which indicate the most of the relaxation is in the first cycle.

On the other hand, by applying a higher load of 208 MPa (80% of Yield Strength of the material), the initial value of residual stress was reduced by 55% from 266.5 MPa to 120.6 MPa, 12.4% more reduced compared to the 52 MPa load amplitude. The residual stress relaxed by 4.9% from 120.6 MPa to 114.7 MPa after the second cycle. The value continued to decrease exponentially to lower load until 105.2 MPa at 1000 cycles, around 8.3% lesser than the residual stress at the second cycle. In overall, the total reduction of residual stress at 1000 cycle from initial residual stress by 60.5% from 266.5 MPa to

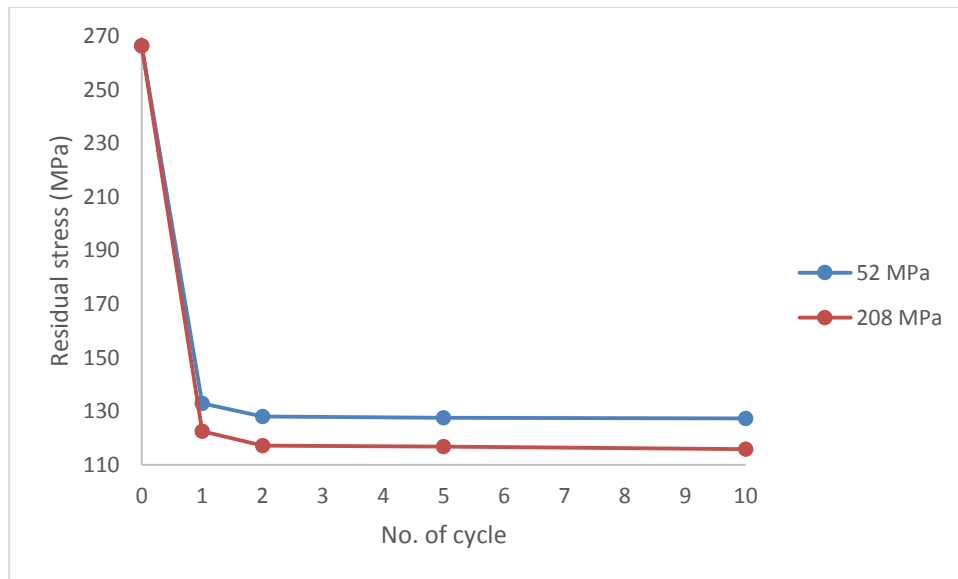
105.2 MPa. Out of this 60.5%, there are 55% is only during the first cycle. 5.5% relaxation occurred from second cycle to 1000 cycle which indicate the most of the relaxation is in the first cycle. Comparing to the low load relaxation, it could be observed that high load resulted high residual stress relaxation (60.5% at high load and 57.4% at low load). Moreover, the relaxation in the first cycle due to high load is higher than the relaxation due to low load (55% for high load and 42.6% for low load).

This agrees with the findings in previous study [134], whereby higher load will cause the residual stress to relax more. Higher amplitude of external load would superpose more residual stress resulting smaller value of stress left under the material surface.

Figure 4.19 (a) and (b) illustrate the residual stress against number of cycles after being applied with 52 MPa and 208 MPa tensile cyclic loads on shot-peened samples with an intensity of 12.9 A.



(a)



(b)

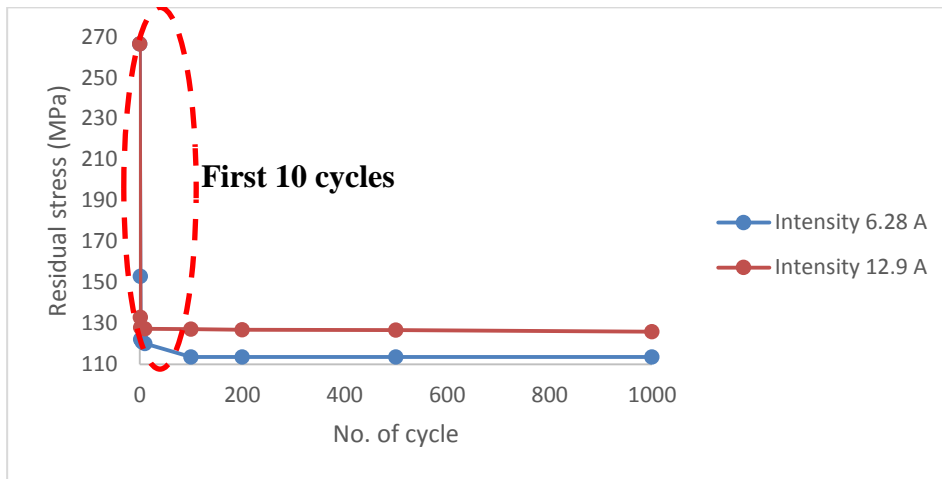
Figure 4.19 Residual stress relaxation against cyclic loading with amplitude of 52 MPa and 208 MPa for intensity 12.9 A (a) 0 to 1000 cycles; (b) 0 to 10 cycles

Based on the results (Table 4.3) from the simulation of a low cyclic load of 52 MPa, the initial value of residual stress which was estimated at 266.5 MPa for control reduced by 50% to 132.9 MPa in the first cycle. The residual stress continued to decrease in the following cycles but only by small variation. After the second cycle, the value of 132.9 MPa dropped by only 3.7% to 128 MPa. The value continued to decrease by approximately 0.3% with the increasing number of cycles. The simulation was completed until 1000 cycles where the residual stress value at this cycle was recorded at 126 MPa, which only 6.9 MPa lower than the first cycle.

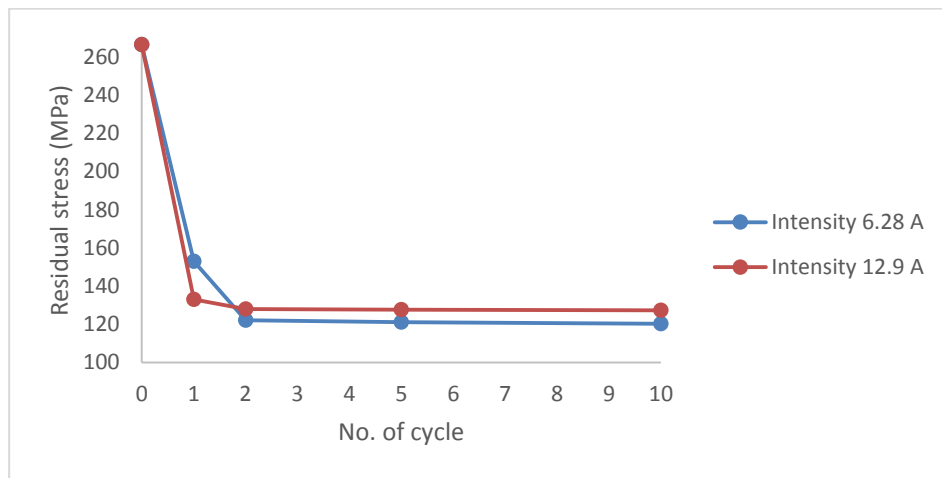
By applying a higher load of 208 MPa, the initial value of the residual stress reduced by 54% from 266.5 MPa to 122.5 MPa after the first cycle, which was 4% more reduced than the 52 MPa load amplitude. The value continued to decrease similarly to a lower load of 115 MPa at 1000 cycles, approximately 6% lower than the residual stress at the first cycle. This data substantiated previous studies by indicating that higher load causes the residual stress to relax more. Higher amplitude of external load would superpose more residual stress resulting in a smaller value of residual stress under the material surface.

Other than comparison of the relaxation of residual stress due to different cyclic load amplitudes, comparison of relaxation of residual stress due to different shot peening intensities on ASTM A516 grade 70 steel for the same cyclic load amplitude was also

conducted. The purpose is to investigate if the shot peening intensity influences the reduction value of the initial residual stress when two different load amplitudes are applied (52 MPa and 208 MPa). Figure 4.20 (a) and (b) shows the graphs for residual stress against number of cycle after being applied with 52 MPa tensile cyclic loads on shot-peened ASTM A516 grade 70 carbon steel with intensities 6.28 A and 12.9 A.



(a)



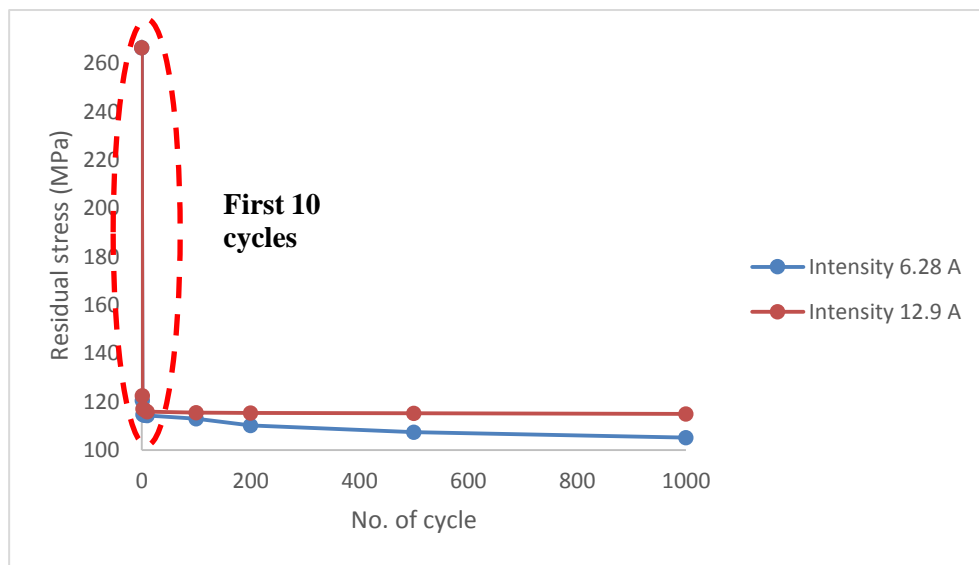
(b)

Figure 4.20 Residual stress relaxation against cyclic loading with amplitude of 52 MPa for intensities 6.28 A and 12.9 A (a) 0 to 1000 cycles; (b) 0 to 10 cycles

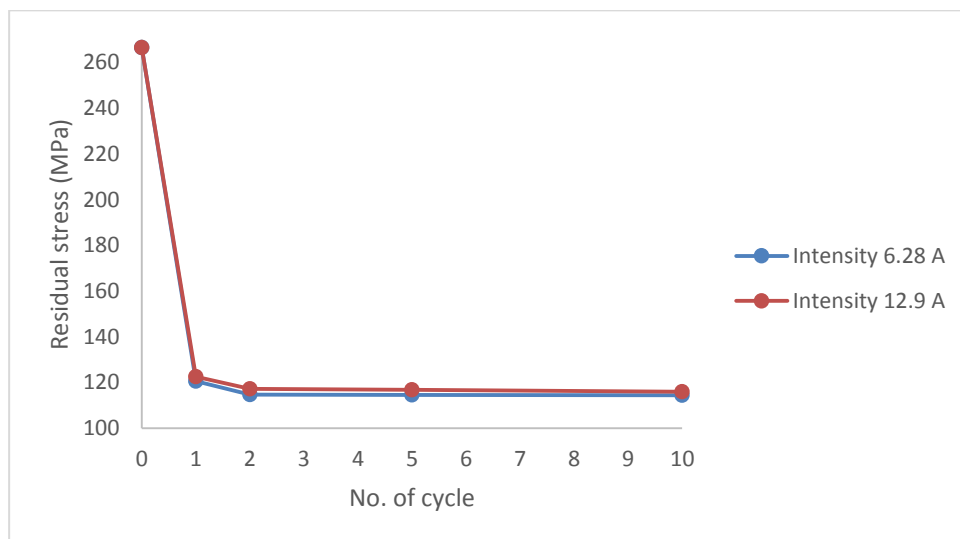
Based on the comparison of shot-peened ASTM A516 grade 70 carbon steel between two intensities (6.28 A and 12.9 A) after being applied with 52 MPa, it could be observed that the trend of relaxation is similar. However, during the first cycle, the relaxation caused by intensity 12.9 A is more than intensity 6.28 A which is 50.1% and 42.6% from initial value respectively. This agrees with previous findings where higher intensity of shot

peening process causes more relaxation of residual stress in material [92]. The value of residual stress continues to decrease gradually until 1000th cycle as explained in previous pages for Figure 4.8 and Figure 4.9.

On the other hand, same analysis was done on 208 MPa applied on two different intensities (6.28 A and 12.9 A). Figure 4.21 shows the graphs for residual stress against number of cycle after being applied with 208 MPa tensile cyclic loads on shot-peened ASTM A516 grade 70 carbon steel with intensities 6.28 A and 12.9 A.



(a)



(b)

Figure 4.21 Residual stress relaxation against cyclic loading with amplitude of 208 MPa for intensities 6.28 A and 12.9 A (a) 0 to 1000 cycles; (b) 0 to 10 cycles

Based on the comparison of shot-peened ASTM A516 grade 70 carbon steel between two intensities (6.28 A and 12.9 A) after being applied with 208 MPa, it could be observed that the trend of relaxation is similar. The difference of relaxation between intensity 6.28 A and 12.9 A for the first cycle is very minor which is only 1.6%.

Simulation results show that residual stress relaxation under cyclic loading is associated with mean-strain shift, which is indicative of stress redistribution. Residual stress is associated with residual strain which also acts as virtual mean strain under constant amplitude cyclic loading. This would also result in biased strain loading condition and, for the case of compressive residual strain, would aid deformation in the compressive direction but oppose deformation in the tensile loading direction. Thus, plastic deformation in the compressive direction within a cycle would not be completely recovered during tensile or forward loading. The net effect would be that the cyclic stress-strain curve and, hence, the mean strain would shift with cycle towards the compressive strain direction causing the reduction value of initial residual stress, this result agrees with theory that has been raised in previous study [137]. Following study still agrees with this theory for different materials [148].

Under cyclic/fatigue loads, residual stress can be regarded as virtual mean stress and causes biased amplitude loading conditions. Thus, the material would be subjected to both cyclic stress and residual (mean) stress. When the sum of cyclic stress and residual stress exceeds the local yield stress of the material, cyclic-plastic deformation would occur. The occurrence of plastic deformation causes reduction in the residual stress which tends to shift the stress-strain curve vertically towards zero mean stress. For the compressive residual stress the shift would be in the tensile direction. Plastic deformation in the biased stress/strain direction would not be completely recovered during reversed loading, resulting in the shift of mean strain position on the strain axis, in the direction of bias strain. For the compressive residual stress, the shift is in the compressive direction. According to this discussion the compressive residual stress is not beneficial for a part that is operating in compressive load application while it will be only beneficial and increase the fatigue life if the part is operating under tension loading, vice versa; tension residual stress is not beneficial for a part that is operating under tension load but it will be beneficial and increase fatigue life if the part is operating under compressive loading.

This is due to the summation of applied stress and residual stress depends on the direction of the opposition loading.

4.3.4 Numerical modelling of residual stress relaxation

The numerical residual stress relaxation model was developed for low cyclic region (0 to 10 cycles) for high and low loads and high and low intensities from simulation data based on the best curve fitting. The trend is in power equation which includes the residual stress relaxation at each cycle σ_{RN} with number of cycles, N as shown in equation 4.10.

$$\sigma_{RN} = A \cdot N^B \quad (4.10)$$

where A and B are the constants depending on the shot peening intensity and the amplitude of applied tensile stress. The value of A and B for low load (52 MPa) and high load (208 MPa) as well as low intensity (6.28 A) and high intensity (12.9 A) are shown in Table 4.16.

Table 4.16 Residual stress relaxation constants for of low cyclic region for shot peening with intensity 6.28 A and 12.9A.

Load Applied	Intensity 6.28 A		
	A	B	R ²
52 MPa	142.5	-0.091	0.9674
208 MPa	130.94	-0.099	0.9625
	Intensity 12.9 A		
	A	B	R ²
52 MPa	143.29	-0.086	0.9620
208 MPa	132.91	-0.097	0.9644

The numerical residual stress relaxation model was developed for high cyclic region (10 to 1000 cycles) for high and low loads and high and low intensities from simulation data based on the best curve fitting. The trend is in linear equation which also includes the residual stress relaxation at each cycle σ_{RN} with number of cycles, N as shown in equation 4.11.

$$\sigma_{RN} = C.N + D \quad (4.11)$$

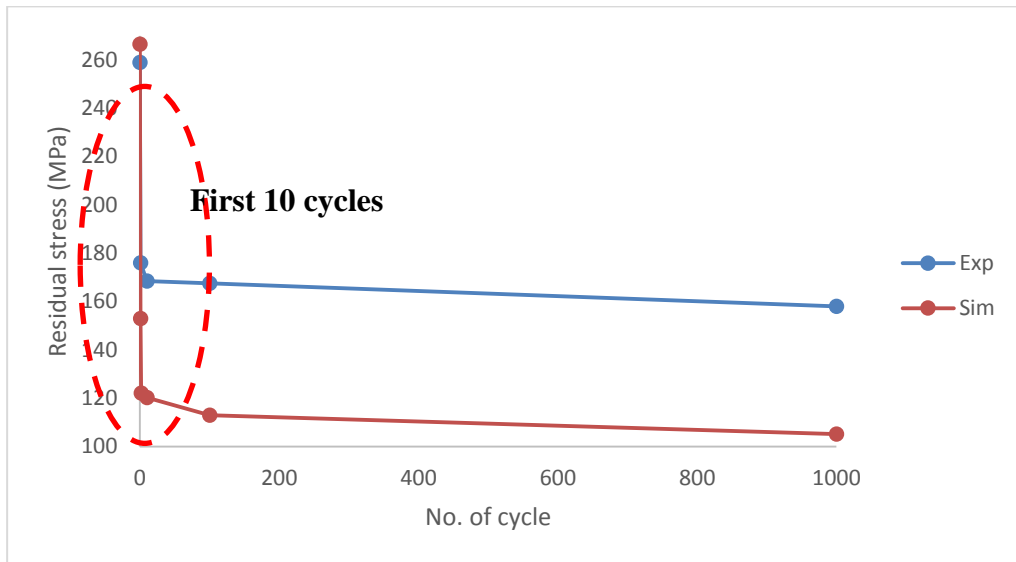
where C and D are the constants depending on the shot peening intensity and the amplitude of applied tensile stress. The value of C and D for low load (52 MPa) and high load (208 MPa) as well as low intensity (6.28 A) and high intensity (12.9 A) are shown in Table 4.17.

Table 4.17 Residual stress relaxation constants for of high cyclic region for shot peening with intensity 6.28 A and 12.9A.

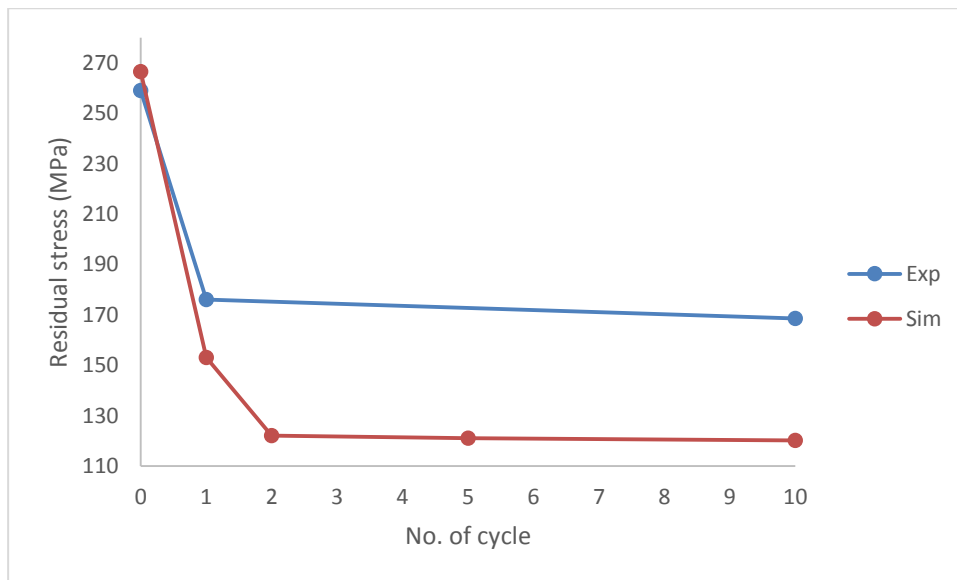
Load Applied	Intensity 6.28 A		
	C	D	R ²
52 MPa	0	113.6	-
208 MPa	-0.0079	112.52	0.8933
	Intensity 12.9 A		
52 MPa	-0.0012	127.26	0.9736
208 MPa	-0.0005	115.54	0.9854

4.3.5 Validation of experimental result by simulation result

Four sets of graphs were plotted to validate the simulation result i.e. the numerical model using the experimental result. Each set of graphs were plotted based on the parameters of the shot peening intensity and the amplitude of the cyclic load applied to the sample. Figure 4.22 (a) and (b) shows the simulation and experimental results of residual stress against the number of cycles for 6.28 A intensity with 52 MPa of the cyclic load.



(a)



(b)

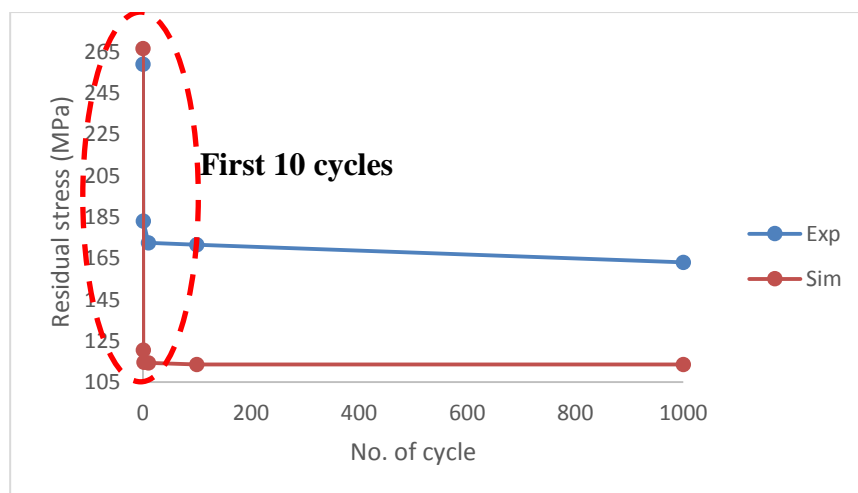
Figure 4.22 Comparison between simulation and experimental residual stress relaxation of shot-peened material with intensity 6.28A and cyclic load applied with amplitude of 52 MPa (a) 0 to 1000 cycles; (b) 0 to 10 cycles.

In reference to the results obtained from this study , both the simulation and experimental methods produced an equivalent trend of residual stress relaxation. The reduction mostly occurred in the first cycle. During the simulation methods, the initial residual stress dropped by 42.6% to 153.0 MPa from 266.5 MPa. Both the methods reached uniformity with a difference of 13.3%. As for the experimental process, the initial residual stress that was estimated at 259 MPa was reduced by 29.3% to 183 MPa. This shows an agreement with 13.3% of difference between experimental and simulation reduction during the first cycle.

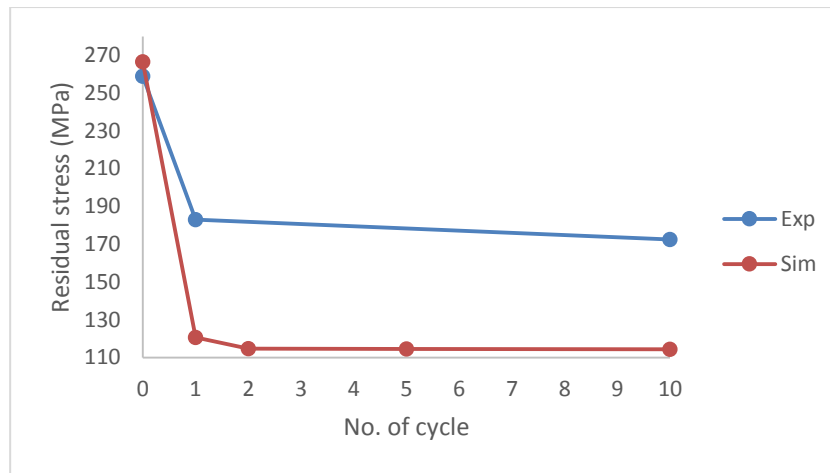
Throughout the simulation methods, the residual stress continuously reduced by 20.2% in the second cycle from 153.0 MPa to 122.1 MPa. The residual stress continued to relax till 1000th cycles estimated at 113.6 MPa. The residual stress experienced a 25.8% reduction from the first cycle, 153.0 MPa to 113.6 MPa at 1000th cycle.

The experimental method did not include measurement for cycle 2 and 5. At 10th cycle, the residual stress dropped to 172.5 MPa from 183 MPa, a 5.7 % reduction. This also shows agreement in the percentage of reduction with only 0.6% difference (5.7% experimental and 5.1% simulation). The relaxation of residual stress continued until it reached a minimum value of 163 MPa at 1000th cycles.

Next, the comparison between the simulation and experimental results of residual stress against the number of cycles at 6.28 A intensity and 208 MPa of the cyclic load is demonstrated in Figure 4.23.



(a)



(b)

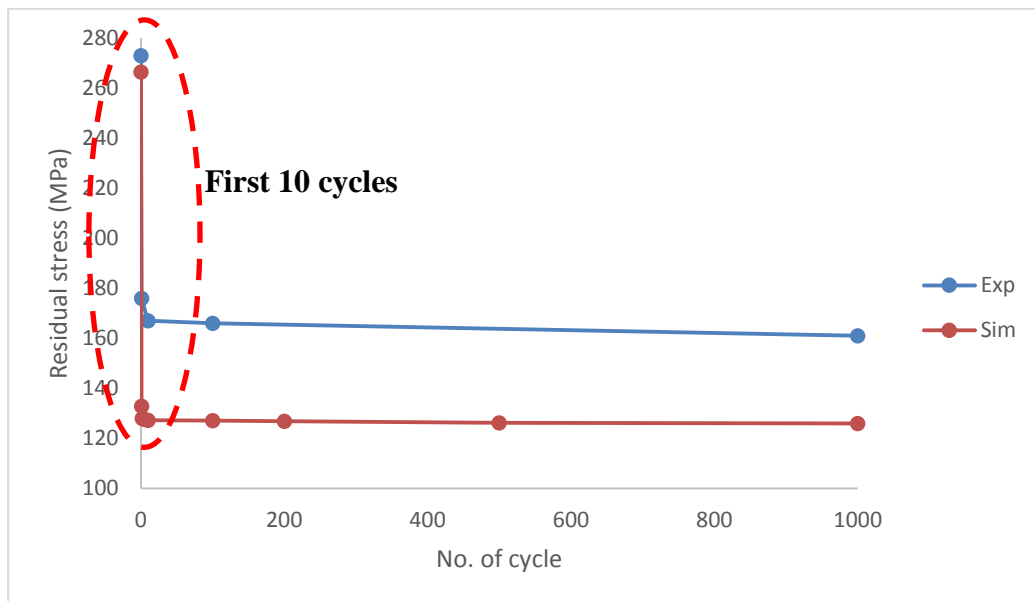
Figure 4.23 Comparison between simulation and experimental residual stress relaxation of shot-peened material with intensity 6.28A and cyclic load applied with amplitude of 208 MPa (a) 0 to 1000 cycles; (b) 0 to 10.

Both simulation and experimental methods demonstrated a similar trend in residual stress relaxation. Relaxation occurred primarily in the first cycle. The experimental result indicated a reduction in initial residual stress by 32% from 259 MPa to 176 MPa. The simulation result, on the other hand, exhibited a reduction by 54.7% from 266.5 MPa to 120.6 MPa during the first cycle. An agreement between the two parts was achieved with a difference of 22.7%.

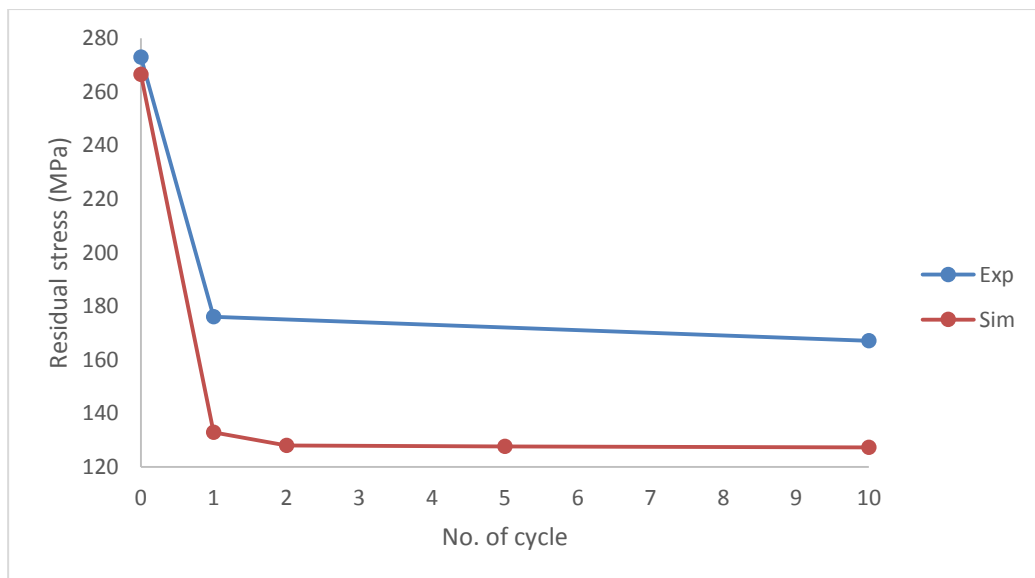
The residual stress for the simulation part continued to relax gradually during the second cycle with 30.9 MPa difference which approximately 4.9% from 120.6 MPa to 114.7 MPa. This behaviour continues until the 1000th cycle when the minimum residual stress is 105.2 MPa. Starting from the second cycle, the residual stress reduce by 8.3% difference from 114.7 MPa to 105.2 MPa. For comparison with the experimental result, the value of residual stress at the 10th cycle is reduced by 5.1% from 120.6 MPa in the first cycle to 114.4 MPa.

Meanwhile, for the experimental part, the residual stress value was not measured for the second cycle. The next measurement was done on the 10th cycle sample. The value of residual stress reduced by 4.3% from 176 MPa to 168.5 MPa. This also shows agreement in the reduction percentage with only 0.8% difference (4.3% experimental and 5.1% simulation). The residual stress relaxed gradually to a minimum value of 158 MPa during the 1000th cycle. Figure 4.24 shows the simulation and experimental results of residual

stress against a number of the cycle for intensity 12.9 A and applied with 52 MPa of the cyclic load.



(a)



(b)

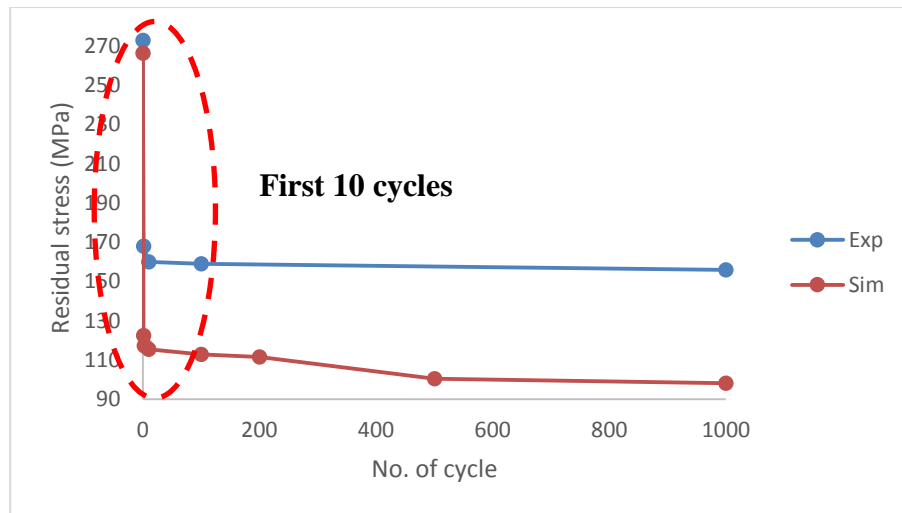
Figure 4.24 Comparison between simulation and experimental residual stress relaxation of shot-peened material with intensity 12.9 A and cyclic load applied with amplitude of 52 MPa (a) 0 to 1000 cycles; (b) 0 to 10.

Based on the results obtained the trend of residual stress relaxation for experimental and simulation are similar. The most reduction occurs during the first cycle. The initial residual stress reduced by 35.5% from 273 MPa to 176 MPa for experimental. On the other hand, the initial residual stress in the simulation part reduced by 50% from 266.5

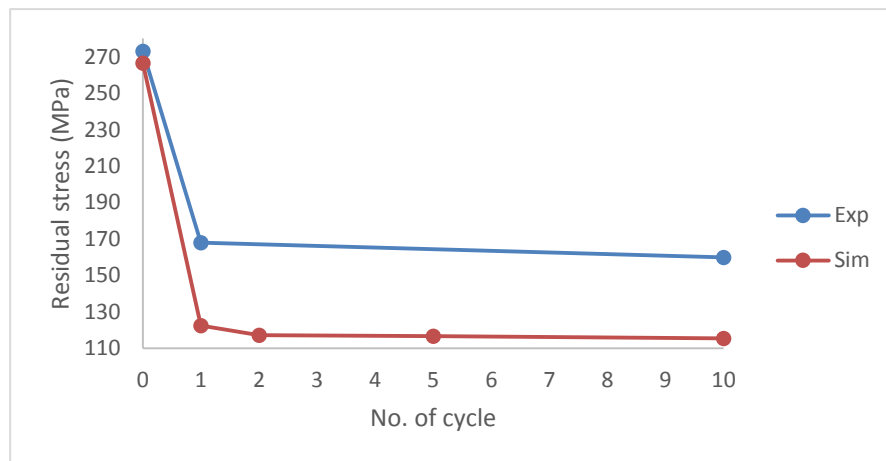
MPa to 132.9 MPa. The agreement between the two parts is achieved with a difference of 16.5%.

For the simulation part, the residual stress continues to relax gradually during the second cycle with only 4 MPa difference which approximately 3.7% from 132.9 MPa to 128 MPa. This behaviour continues until the 1000th cycle when the minimum residual stress is 126 MPa. Starting from the second cycle, the residual stress does not reduce much by only 1.6% difference from 128 MPa to 126 MPa. For comparison with the experimental result, the value of residual stress at the 10 cycles is reduced by 4.2% from 132.9 MPa in the first cycle to 127.3 MPa.

Meanwhile, for the experimental part, the residual stress value was not measured for the second cycle. The next measurement was done on the 10th cycle sample. The value of residual stress reduced by 5% from 176 MPa to 167 MPa. This also shows agreement in the reduction percentage with only 0.8% difference (5% experimental and 4.2% simulation). The residual stress relaxed gradually to a minimum value of 161 MPa during the 1000th cycle. Figure 4.25 shows the simulation and experimental results of residual stress against a number of the cycle for intensity 12.9 A and applied with 209 MPa of the cyclic load.



(a)



(b)

Figure 4.25 Comparison between simulation and experimental residual stress relaxation of shot-peened material with intensity 12.9A and cyclic load applied with amplitude of 208 MPa (a) 0 to 1000 cycles; (b) 0 to 10.

Based on the results obtained the trend of residual stress relaxation for experimental and simulation are similar. The most reduction occurs during the first cycle. The initial residual stress reduced by 38.5% from 273 MPa to 168 MPa for experimental. On the other hand, the initial residual stress in the simulation part reduced by 54% from 266.5 MPa to 122.5 MPa. The agreement between the two parts is achieved with a difference of 15.5%.

For the simulation part, the residual stress continues to relax gradually during the second cycle with only 5.3 MPa difference which approximately 4.3% from 122.5 MPa to

117.2 MPa. This behaviour continues until the 1000 cycle when the minimum residual stress is 98.2 MPa. Starting from the second cycle, the residual stress reduce by 16% difference from 117.2 MPa to 98.2 MPa. For comparison with the experimental result, the value of residual stress at the 10 cycles is reduced by 5.7% from 122.5 MPa in the first cycle to 115.5 MPa.

Meanwhile, for the experimental part, the residual stress value was not measured for the second cycle. The next measurement was done on the 10th cycle sample. The value of residual stress reduced by 4.8% from 168 MPa to 160 MPa. This also shows agreement in the reduction percentage with only 1.1% difference (5.7% experimental and 4.8% simulation). The residual stress relaxed gradually to a minimum value of 156 MPa during the 1000th cycle.

In summary, both experimental and simulation result showed a good agreement in term of the trend of relaxation of residual stress especially during the first cycle where the most relaxation occurred (with a difference of 16% in average). This finding agreed with previous studies where the compressive residual stress decreases at most during the first cycle (approximately 50% reduction from initial value) [148]. The difference between simulation and experimental result is due to some limitations. Firstly, the initial residual stress is considered as equal for both intensities in simulation. The relaxation is calculated based on the initial residual stress introduced in shot peening simulation. On the other hand, the initial values of residual stress in experimental are different for each intensity. This is based on the result of shot peening process with different parameters which were conducted on the material. The number of elements could influence the result where it well known that higher number of element would produce more accurate result [149]. However, this could increase the computational time and this might be irrelevant in terms of validating the trend of residual stress relaxation against experimental work. Other limitation of the model is the time stepping stability where this parameter also has high influence on the computational time [150 – 151]. Time stepping stability needs to be investigated in the future for more uniform stress distribution against cyclic load.

CHAPTER 5

CONCLUSION AND RECOMMENDATIONS FOR FUTURE WORK

5.1 Conclusion

The present study utilised numerical and experimental evaluation methods to investigate the trends in residual stress and surface hardness of low carbon steel namely ASTM A516 grade 70 based on different shot peening intensities against cyclic loading. The variables within the cyclic loading were categorised into low and high cyclic regions. Hence, based on the results and observations, the study has achieved the five objectives that were proposed. Below is a summary of the main findings:

1. Upon subjecting to shot peening, ASTM A516 grade 70 steel yielded higher tensile strength. This result indicated that shot peening was capable of improving the mechanical properties of the tested material. However, there were variations between the different parameters that were employed. Compared to the raw material, samples that were shot peened with a low intensity of 6.28 A did not experience a significant change in tensile strength with only a minor increment of 0.5%. On the other hand, the tensile strength significantly increased by 7.1% when the materials were shot peened with a higher intensity of 12.9 A. Though, the elongation was shortened. Hence, it was concluded that although the strength of a material is improved by shot peening with higher intensity, it makes the material more brittle. For this reason, manufacturing lines should choose the appropriate shot peening intensity for their product. Choosing the right intensity ensures the product reaches its specification and fatigue requirement. In addition, shot peening intensity also influences the hardness of the material. The shot peening intensity of 12.9 A increased the hardness by 6.8% and of 6.28 A by 4.3% compared to the raw ASTM A516 grade 70 steel. The data is suggestive that higher intensity yields higher hardness. Previous literature has also suggested that shot peening also improves a material's fatigue life. Although only samples from SP A were subjected to the test, fatigue life was significantly improved by 7.14% and 6.37% upon applying a load of 85% and 75% UTS. Besides, higher shot peening intensity also resulted in a coarser microstructure.

2. High peening intensity also aids in increasing the amount of initial compressive residual stress. With high impacts, more molecules get dislocated and deformed plastic result in increased compressive residual stress in the material.

3. The application of cyclic loading decreased the initial compressive residual stress. A similar pattern was identified in both numerical and experimental approaches. Both the methods employed in this study demonstrated that the highest reduction of residual stress occurred during the first cycle. The initial residual stress was reduced in the first cycle by 40% to 50% and by 25% to 30% for the simulation and experimental method, respectively. During the following cycles, the residual stress experienced an exponential reduction against the number of cycles for both simulation and experimental methods. The results were indicative of a significant reduction in residual stress with higher intensity. The residual stress is lowered due to the higher amplitude of external load which could superpose compressive residual stress.

4. Increased shot peening intensity results in a rougher material surface. The surface roughness was increased by 118% and 353% at 6.28 A and 12.9 A intensities, respectively, compared to the raw material. The increased roughness was due to the impacts from the steel balls hitting the material surface, hence, a dented area with a higher coverage is produced. The surface gets rougher.

5. Finally, the residual stress relaxation model that was developed was successful because the proposed numerical trend demonstrated a good consensus with the experimental result. Furthermore, the division of the proposed numerical model into the low and the high cyclic regions assists in predicting the compressive residual stress at any cycle depending on the peening intensities and the amplitude of cyclic loads applied to ASTM A516 grade 70 steel. The empirical model which was developed integrated the residual stress relaxation with the surface hardness. Therefore, by using this model, if the surface hardness is known, the value of residual stress can be predicted. The development of this model greatly contributed to lowering the cost of operation by bypassing the need to perform residual stress measurement in order to obtain the value of residual stress.

5.2 Recommendation for future works

For future work, various materials and parameters can be tested to produce additional data to understand the relaxation of residual stress in different scenarios. The different parameters include different approaches to introducing residual stress apart from shot peening and various amplitude of cyclic load applied to the material. Potential suggestions for future work include:

1. This model could be expanded by generating more parameters for different peening intensities and amplitude of cyclic loading.
2. Investigate whether a combination of cyclic load and different temperatures could affect residual stress relaxation.
3. Compare residual stress generated by other surface treatments to shot peening process, based on the magnitude of residual stress, surface hardness and surface roughness. Each process should be subjected to a simulation followed by experimental validation.
4. Further study can be done by using strain model where the method is more complex but more accurate in determining the relaxation of residual stress.
5. This study could be enhanced by creating new model to simulate the “in-depth” residual stress values and validated with experimental “in-depth” XRD measurement.

REFERENCES

- [1] Residualstress.org. (2019). Residual Stress – Measurements. [online] Available at: <http://www.residualstress.org/>.
- [2] P. J. Withers and H. K. D. H. Bhadeshia, “Residual stress Part 1 – Measurement Techniques,” 2001.
- [3] C. You, M. Achintha, B. Y. He, and P. A. S. Reed, “A numerical study of the effects of shot peening on the short crack growth behaviour in notched geometries under bending fatigue tests,” *Int. J. Fatigue*, vol. 103, pp. 99–111, 2017.
- [4] L. Wagner, “Mechanical surface treatments on titanium , aluminum and magnesium alloys,” *Materials Science and Engineering A263*, vol. 263, pp. 210–216, 1999.
- [5] B. Y. He, K. A. Soady, B. G. Mellor, G. Harrison, and P. A. S. Reed, “Fatigue crack growth behaviour in the LCF regime in a shot peened steam turbine blade material,” *Int. J. Fatigue*, vol. 82, pp. 280–291, 2016.
- [6] M. E. Turan, F. Aydin, Y. Sun, and M. Cetin, “Residual stress measurement by strain gauge and X-ray diffraction method in different shaped rails,” *Eng. Fail. Anal.*, vol. 96, no. June 2018, pp. 525–529, 2019.
- [7] E. Maleki, O. Unal, and K. Reza Kashyzadeh, “Fatigue behavior prediction and analysis of shot peened mild carbon steels,” *Int. J. Fatigue*, vol. 116, no. June, pp. 48–67, 2018.
- [8] O. S. Zaroog, A. Ali, B. Sahari, and R. Zahari, “Modelling of Residual Stress Relaxation: A Review,” *Pertanika J Sci Technol*, vol. 17, no. January, pp. 211–218, 2009.
- [9] A. B. Ibrahim, F. A. Al-badour, A. Y. Adesina, and N. Merah, “Effect of process parameters on microstructural and mechanical properties of friction stir di ff usion cladded ASTM A516-70 steel using 5052 Al alloy,” *J. Manuf. Process.*, vol. 34, no. February, pp. 451–462, 2018.
- [10] S. Khadijah et al., “Mechanical properties of paste carburized ASTM A516 steel,” *Procedia Eng.*, vol. 68, pp. 525–530, 2013.
- [11] SA-516/ SA-516M, “Specification for pressure vessel plates , carbon steel, for moderate - and lower – temperature service,” pp. 959–965, 2013.

- [12] T. O. Standard, A. American, and N. Standard, “Standard Test Methods for Tension Testing of Metallic Materials 1,” 2013.
- [13] M. O. F. Solids, “Depth of penetration due to Minor load of 98.07 N. E,” pp. 1–38.
- [14] H. Testing, “Vickers Hardness Test,” pp. 8–9.
- [15] T. Equipment, “Micro Vickers Hardness Testing Machines.”
- [15] O. The and I. Hardness, “Hardness test 1.,” pp. 1–8.
- [16] Q. Yang, W. Zhou, Z. Niu, X. Zheng, Q. Wang, X. Fu, G. Chen, Z. Li, “Surface & Coatings Technology Effect of different surface asperities and surface hardness induced by shot-peening on the fretting wear behavior of Ti-6Al-4V,” *Surf. Coat. Technol.*, vol. 349, no. July, pp. 1098–1106, 2018.
- [17] P. Fu, R. Chu, Z. Xu, G. Ding, and C. Jiang, “Relation of hardness with FWHM and residual stress of GCr15 steel after shot peening,” *Appl. Surf. Sci.*, vol. 431, pp. 165–169, 2018.
- [18] K. D. Ramkumar, S. Singh, J. C. George, S. Anirudh, G. Brahadees, S. Goyal, S. K. Gupte, C. Vishnu, N.R. Sharan, S. Kalainathan, “Effect of pulse density and the number of shots on hardness and tensile strength of laser shock peened, activated flux TIG welds of AISI,” *J. Manuf. Process.*, vol. 28, pp. 295–308, 2017.
- [19] ASTM E466, “Standard Practice for Conducting Force Controlled Constant Amplitude Axial Fatigue Tests of Metallic Materials”.
- [20] C. Leser, “High-Cycle Fatigue Testing August Wöhler Fatigue Experiments Simplified representation of his rotating beam experiments”, 2013.
- [21] B. No, “QUICK GUIDE TO SURFACE,” no. 2229.
- [22] L. Zhu, Y. Guan, Y. Wang, Z. Xie, J. Lin, and J. Zhai, “Surface & Coatings Technology Influence of process parameters of ultrasonic shot peening on surface roughness and hydrophilicity of pure titanium,” *Surf. Coat. Technol.*, vol. 317, pp. 38–53, 2017.
- [23] Y. G. Liu, M. Q. Li, and H. J. Liu, “Materials Characterization Nanostructure and surface roughness in the processed surface layer of Ti-6Al-4V via shot peening,” vol. 123, pp. 83–90, 2017.

- [24] R. K. Kumar, P. Sampathkumaran, S. Seetharamu, S. A. Kumar, T. Pramod, G. J. Naveen, “Investigation of Shot Peening Effect on Titanium Alloy Affecting Surface Residual Stress and Roughness for Aerospace Applications,” *Procedia Structural Integrity*, vol 14, pp. 134 – 141, 2019.
- [25] W. Zhou, R. P. Apkarian, and Z. L. Wang, “Fundamentals of Scanning Electron Microscopy.”
- [26] R. F. Kubler, S. Berveiller, D. Bouscaud, R. Guiheux, E. Patoor, and Q. Puydt, “Shot peening of TRIP780 steel: Experimental analysis and numerical simulation,” *J. Mater. Process. Technol.*, vol. 270, pp. 182–194, 2019.
- [27] H. Soyama, “Comparison between the improvements made to the fatigue strength of stainless steel by cavitation peening , water jet peening , shot peening and laser peening,” *J. Mater. Process. Tech.*, vol. 269, no. July 2018, pp. 65–78, 2019.
- [28] T. Klotz, M. Lévesque, and M. Brochu, “Effects of rolled edges on the fatigue life of shot peened Inconel 718,” *J. Mater. Process. Technol.*, vol. 263, no. May 2018, pp. 276–284, 2019.
- [29] R. J. D. Tatton, “Shot peen-forming,” In: S.A. Meguid. *Proceedings of the 2nd International Conference on Impact Treatment Process*, Elsevier applied science: pp. 134-143, 1986.
- [30] American Wheelabrator & Equipment Corporation, “Shot Peening”. 3rd ed. Mishawaka, Indiana; p. 82, 1947.
- [31] The Wheelabrator Corporation, “Shot peening of metal parts”. Military Specification, MIL-S-13165C, The Wheelabrator Corporation: USA, 1989.
- [32] The Wheelabrator Corporation, “Shot peening of metal parts”. Military Specification, MIL-S-13165C, The Wheelabrator Corporation: USA, 1989.
- [33] D. L. Baughman, “Evolution of centrifugal wheel shot peening in the aerospace industry and recent applications”. In: A. Niku-Lari. *First International Conference on Shot Peening. Proceedings of the International Conference on Shot Peening (ICSP-1)*. Paris; Pergamon press, pp. 101-108, 1981.
- [34] H. J. Plaster, “Technical aspects of shot peening machinery and media”. In A. Niku-Lari. *First International Conference on Shot Peening. Proceedings of the International Conference on Shot Peening (ICSP-1)*. Paris; Pergamon press, pp. 83-94, 1981.

- [35] Y. Lecoffre and X. H. Bonazzi, "TRAVEL: A real time particle velocity measuring system for use in shot peening". In: D Kirk. The fifth International Conference on Shot Peening (ICSP-5). Oxford; Coventry University, pp. 61-68, 1993.
- [36] R. Fathallah, "Prediction of plastic deformation and residual stresses induced in metallic parts by shot peening", *Materials Science and Technology*. 14: pp. 631-639, 1998.
- [37] Y. F. Al-Obaid, "A rudimentary analysis of improving fatigue life of metals by shot peening", *Journal of applied mechanics*. 57: 307-312, 1990.
- [38] B. L. Boyce, X. Chen, J. W. Hutchinson and R. O. Ritchie, "The residual stress state due to a spherical hard-body impact", *Mechanics of materials*, 33: pp. 441-454, 2001.
- [39] S. T. S. Al-Hassani, "The shot peening of metal-mechanics and structures", *Shot peening for advance aerospace design. SP-528*, Society of Automotive Engineers: Warrendale, PA., p. 2, 1982.
- [40] M. Kobayashi, T. Matsui and Y. Murukami, "Mechanism of creation of compressive residual stress by shot peening", *International Journal of Fatigue*, 20(5): 351-357, 1998.
- [41] H.J. Frost and M. F. Ashby, "Deformation-Mechanism Maps: The plasticity and creep of metals and ceramics", Oxford: Pergamon Press, 1982.
- [42] Gillespie & K., L., 2009. Hit it again, harder. *Cutting Tool Engineering Plus*.
- [43] N. K. Burrell, "Controlled Shot Peening of Automotive Components," vol. 7, 1985.
- [44] Mfn.li.(2019).[online]Available at:http://www.mfn.li/article/print_article.php?id=695.
- [45] N. S. Sizes, "Size and Variability of Cast Steel Shot Particles," 2009.
- [46] J. P. Fuhr, M. Basha, M. Wollmann, L. Wagner, "Coverage and Peening Angle Effects in Shot Peening on HCF Performance of Ti-6Al-4V," *Procedia Engineering*, vol 213, pp. 682–690, 2018.
- [47] T. Kim, H. Lee, H. Chul, and S. Jung, "Effects of Rayleigh damping , friction and rate-dependency on 3D residual stress simulation of angled shot peening," *Mater. Des.*, vol. 46, pp. 26–37, 2013.

- [48] A. Gariépy, H. Y. Miao, and M. Lévesque, “Simulation of the shot peening process with variable shot diameters and impacting velocities,” *Adv. Eng. Softw.*, vol. 114, pp. 121–133, 2017
- [49] L. Xie et al., “Mechanics of Materials Numerical analysis and experimental validation on residual stress distribution of titanium matrix composite after shot peening treatment,” *Mech. Mater.*, vol. 99, pp. 2–8, 2016.
- [48] E. Maleki, O. Unal, and K. Reza Kashyzadeh, “Fatigue behavior prediction and analysis of shot peened mild carbon steels,” *Int. J. Fatigue*, vol. 116, no. June, pp. 48–67, 2018.
- [49] J. Zhang, X. Li, B. Yang, H. Wang, and J. Zhang, “Effect of micro-shot peening on fatigue properties of precipitate strengthened Cu-Ni-Si alloy in air and in salt atmosphere,” *Surf. Coatings Technol.*, vol. 359, no. July 2018, pp. 16–23, 2019.
- [50] M. Aslan, A. F. Yetim, H. Kovacı, A. Çelik, and Y. B. Bozkurt, “The effect of surface plastic deformation produced by shot peening on corrosion behavior of a low-alloy steel,” *Surf. Coatings Technol.*, vol. 360, no. July 2018, pp. 78–86, 2019.
- [51] C. Liu, H. Zheng, X. Gu, B. Jiang, and J. Liang, “Effect of severe shot peening on corrosion behavior of AZ31 and AZ91 magnesium alloys,” *J. Alloys Compd.*, vol. 770, pp. 500–506, 2019.
- [52] T. Otsuka, K. Goto, A. Yamamoto, and K. Hashizume, “Effects of shot-peening on permeation and retention behaviors of hydrogen in alpha iron,” *Fusion Eng. Des.*, vol. 136, no. March, pp. 509–512, 2018.
- [53] G. K. Poongavanam and V. Ramalingam, “Effect of shot peening on enhancing the heat transfer performance of a tubular heat exchanger,” *Int. J. Therm. Sci.*, vol. 139, no. January, pp. 1–14, 2019.
- [54] A. Hoffman, O. Stav, I. Etsion, Y. Kligerman, R. Akhvlediani, and H. Kasem, “Simultaneous Shot-Peening of hard and soft particles for friction reduction in reciprocal sliding,” *Tribol. Int.*, vol. 130, no. May 2018, pp. 19–26, 2018.
- [55] R. F. Kubler, S. Berveiller, D. Bouscaud, R. Guiheux, E. Patoor, and Q. Puydt, “Shot peening of TRIP780 steel: Experimental analysis and numerical simulation,” *J. Mater. Process. Technol.*, vol. 270, pp. 182–194, 2019.

- [56] X. Xiao, X. Tong, Y. Sun, Y. Li, S. Wei, and G. Gao, "An analytical model for predicting peening stresses with general peening coverage," *J. Manuf. Process.*, vol. 45, no. July, pp. 242–254, 2019.
- [57] R. Guiheux, S. Berveiller, R. Kubler, D. Bouscaud, E. Patoor, and Q. Puydt, "Martensitic transformation induced by single shot peening in a metastable austenitic stainless steel 301LN : Experiments and numerical simulation," *J. Mater. Process. Tech.*, vol. 249, no. May, pp. 339–349, 2017.
- [58] Zarka, J., 1990. A New Approach in Inelastic Analysis of Structures. CADLM.
- [59] W. Jianming, L. Feihong, Y. Feng, Z. Gang, "Shot peening simulation based on SPH method," *The International Journal of Advanced Manufacturing Technology*, vol 56 (5), pp. 571–578, 2011.
- [60] K. Murugaratnam, S. Utili, N. Petrinic, "A combined DEM-FEM numerical method for shot peening parameter optimisation." *Advances in Engineering Software*, vol 79, pp. 13 – 26, 2015.
- [61] F. Tu, D. Delbergue, H. Miao, T. Klotz, M. Brochu, P. Bocher, M. Levesque, "A sequential DEM-FEM coupling method for shot peening simulation," *Surface and Coatings Technology*, vol 319, pp. 200 – 212, 2017.
- [62] J. Zhang, S. Lu, T. Wu, Z. Zhou, W. Zhang, "An evaluation on sp surface property by means of combined FEM-DEM shot dynamics simulation," *Advances in Engineering Software*, vol 115, pp. 283 – 296, 2018.
- [63] M. Guagliano, "Relating almen intensity to residual stresses induced by shot peening: a numerical approach," *Journal of Materials Processing Technology* vol 110(3), pp. 277 – 286, 2001.
- [64] M. Klemenz, V. Schulze, I. Rohr, D. Löhle, "Application of the FEM for the prediction of the surface layer characteristics after shot peening," *Journal of Materials Processing Technology*, vol 209 (8), pp. 4093–4102, 2009.
- [65] A. Gariépy, H. Miao, M. L'évesque, "Simulation of the shot peening process with variable shot diameters and impacting velocities," *Advances in Engineering Software*, vol 114, pp. 121 – 133, 2017.
- [66] S. Bagherifard, R. Ghelichi, M. Guagliano, "On the shot peening surface coverage and its assessment by means of finite element simulation: A critical review and some original developments," *Applied Surface Science*, vol 259, pp. 186 – 194, 2012.

- [67] X. Xiao, X. Tong, G. Gao, R. Zhao, Y. Liu, Y. Li, “Estimation of peening effects of random and regular peening patterns,” *Journal of Materials Processing Technology*, vol 254, pp. 13 –24, 2018.
- [68] D. Gallitelli, V. Boyer, M. Gelineau, Y. Colaitis, E. Rouhaud, D. Retraint, R. Kubler, M. Desvignes, L. Barrallier, “Simulation of shot peening: From process parameters to residual stress fields in a structure,” *Computational Simulation of Manufacturing Processes*, vol 344(4), pp. 355 – 374, 2016.
- [69] T. Chaise, J. Li, D. N´elias, R. Kubler, S. Taheri, G. Douchet, V. Robin, P. Gilles, “Modelling of multiple impacts for the prediction of distortions and residual stresses induced by ultrasonic shot peening (USP),” *Journal of Materials Processing Technology*, vol 212 (10), pp. 2080 – 2090, 2012.
- [70] G. I. Mylonas and G. Labeas, “Surface & Coatings Technology Numerical modelling of shot peening process and corresponding products : Residual stress , surface roughness and cold work prediction,” *Surf. Coat. Technol.*, vol. 205, no. 19, pp. 4480–4494, 2011.
- [71] G. H. Majzoobi, R. Azizi, and A. A. Nia, “A three-dimensional simulation of shot peening process using multiple shot impacts,” vol. 165, pp. 1226–1234, 2005.
- [72] Q. Lin, H. Liu, C. Zhu, and R. G. Parker, “Applied Surface Science Investigation on the effect of shot peening coverage on the surface integrity,” *Appl. Surf. Sci.*, vol. 489, no. February, pp. 66–72, 2019.
- [73] J. Badreddine, E. Rouhaud, M. Micoulaut, and S. Remy, “International Journal of Mechanical Sciences Simulation of shot dynamics for ultrasonic shot peening : Effects of process parameters,” *Int. J. Mech. Sci.*, vol. 82, pp. 179–190, 2014.
- [74] H. Chen, S. Wang, S. Lu, Y. Qiao, X. Wang, N. Fan, P. Guo, J. Niu, “Simulation and experimental validation of residual stress and surface roughness of high manganese steel after shot peening,” *Procedia CIRP*, vol 71, pp. 227 – 231, 2018.
- [75] X. Xiao, X. Tong, Y. Liu, R. Zhao, G. Gao, and Y. Li, “International Journal of Mechanical Sciences Prediction of shot peen forming effects with single and repeated impacts,” *Int. J. Mech. Sci.*, vol. 137, no. November 2017, pp. 182–194, 2018.

- [76] M. Marini, V. Fontanari, M. Bandini, and M. Benedetti, "Surface & Coatings Technology Surface layer modifications of micro-shot-peened Al-7075-T651: Experiments and stochastic numerical simulations," *Surf. Coat. Technol.*, vol. 321, pp. 265–278, 2017.
- [77] R. Purohit, C. S. Verma, R. S. Rana, R. Dwivedi, and S. Dwivedi, "Simulation of shot peening process," *Mater. Today Proc.*, vol. 4, no. 2, pp. 1244–1251, 2017.
- [78] V. B. Nguyen, H. Joo, and Y. Zhang, "Predicting shot peening coverage using multiphase computational fluid dynamics simulations," *Powder Technol.*, vol. 256, pp. 100–112, 2014.
- [79] T. Kim, J. Haeng, H. Lee, and S. Cheong, "An area-average approach to peening residual stress under multi-impacts using a three-dimensional symmetry-cell finite element model with plastic shots," *Mater. Des.*, vol. 31, no. 1, pp. 50–59, 2010.
- [80] J. O. Peters, O. Roder, B. L. Boyce, A. W. Thompson, and R. O. Ritchie, "Role of Foreign-Object Damage on Thresholds for High-Cycle Fatigue in Ti-6Al-4V," no. June, 2000.
- [81] X. Kang, T. Wang, and J. Platts, "Multiple impact modelling for shot peening and peen forming," vol. 224, pp. 689–697, 2009.
- [82] Z. Liu, L. Xiu, J. Wu, G. Lv, and J. Ma, "Numerical simulation on residual stress eliminated by shot peening using SPH method," *Fusion Eng. Des.*, vol. 147, no. June, p. 111231, 2019.
- [83] S. A. Meguid, "Development and Validation of Novel FE Models for 3D Analysis of Peening of Strain-Rate," *Journal of Eng. Mat. And Tech*, no. 1 January 2015, 2007.
- [84] T. Kim, J. Haeng, H. Lee, and S. Cheong, "An area-average approach to peening residual stress under multi-impacts using a three-dimensional symmetry-cell finite element model with plastic shots," *Mater. Des.*, vol. 31, no. 1, pp. 50–59, 2010.

- [85] C. Wang, J. Hu, Z. Gu, Y. Xu, and X. Wang, "Simulation on Residual Stress of Shot Peening Based on a Symmetrical Cell Model" *Chinese Journal of Mechanical Engineering*, vol. 30. 2017
- [86] C. Wang, L. Wang, X. Wang, and Y. Xu, "International Journal of Mechanical Sciences Numerical study of grain refinement induced by severe shot peening," *Int. J. Mech. Sci.*, vol. 146–147, no. August, pp. 280–294, 2018.
- [87] L. Faksa et al., "Surface & Coatings Technology Shot peening-induced plastic deformation of individual phases within a coated WC-Co hard metal composite material including stress-strain curves for WC as a function of temperature," *Surf. Coat. Technol.*, vol. 380, no. September, p. 125026, 2019.
- [88] X. Wang, Z. Wang, G. Wu, J. Gan, Y. Yang, and H. Huang, "Combining the finite element method and response surface methodology for optimization of shot peening parameters," *Int. J. Fatigue*, vol. 129, no. April, p. 105231, 2019.
- [89] H. Materials, W. Daves, W. Ecker, T. Klünsner, M. Tkadletz, and C. Czettl, "International Journal of Refractory Metals Effect of shot peening on residual stresses and crack closure in CVD coated hard metal cutting inserts," vol. 82, no. October 2018, pp. 174–182, 2019.
- [90] R. Eriksson, J. Moverare, and Z. Chen, "A low cycle fatigue life model for a shot peened gas turbine disc alloy," *Int. J. Fatigue*, vol. 124, no. February, pp. 34–41, 2019
- [91] J. A. Joy, M. Sajjad, and D. W. Jung, "The Finite Element Analysis for Shot Peening Process of 20 Balls," *Journal of Automation and Control Engineering*, vol. 6, no. 1, pp. 9–16, 2018.
- [92] K. Zaleski, "The numerical fem model of the kinematics of the vibratory," *Advances in Science and Technology Research Journal*, vol. 11, pp. 260–269, 2017.
- [93] X. Liu, J. Liu, Z. Zuo, and H. Zhang, "International Journal of Mechanical Sciences Numerical study on residual stress redistribution of shot-peened aluminum 7075-T6 under fretting loading," vol. 160, pp. 156–164, 2019.
- [94] F. Tu, D. Delbergue, H. Miao, T. Klotz, M. Brochu, P. Bocher, M. Levesque, "Surface & Coatings Technology A sequential DEM-FEM coupling method for shot peening simulation," *Surf. Coat. Technol.*, vol. 319, pp. 200–212, 2017.

- [95] E. Sonde, T. Chaise, N. Boisson, and D. Nelias, "Modeling of cavitation peening : Jet , bubble growth and collapse , micro-jet and residual stresses," *J. Mater. Process. Tech.*, vol. 262, pp. 479–491, 2018.
- [96] M. Benedetti, V. Fontanari, B. Winiarski, M. Allahkarami, and J. C. Hanan, "Residual stresses reconstruction in shot peened specimens containing sharp and blunt notches by experimental measurements and finite element analysis," *Int. J. Fatigue*, vol. 87, pp. 102–111, 2016.
- [97] H. Ullah, A. Rauf, and M. Rehan, "Explicit dynamics simulation of shot peening process induced by various types of shots impacts," *Journal of the Brazilian Society of Mechanical Sciences and Engineering*, vol. 37, pp. 110–112, 2018.
- [98] Y. H. Yang, M. Wan, and W. H. Zhang, "Finite element modelling of shot peening process- A progress overview," *Int. J. Simul. Multidiscip. Des. Optim.*, vol. 3, pp. 332–336, 2009.
- [99] H. Y. Miao, S. Larose, C. Perron, and M. Lévesque, "Advances in Engineering Software On the potential applications of a 3D random finite element model for the simulation of shot peening," *Adv. Eng. Softw.*, vol. 40, no. 10, pp. 1023–1038, 2009.
- [100] S. M. H. Gangaraj, M. Guagliano, and G. H. Farrahi, "Surface & Coatings Technology An approach to relate shot peening finite element simulation to the actual coverage," *Surf. Coat. Technol.*, vol. 243, pp. 39–45, 2014.
- [101] S. C. Wu, S. Q. Zhang, and Z. W. Xu, "Thermal crack growth-based fatigue life prediction due to braking for a high-speed railway brake disc," vol. 87, pp. 359–369, 2016.
- [102] Y. S. Kong, M. Z. Omar, L. B. Chua, and S. Abdullah, "Fatigue life prediction of parabolic leaf spring under various road conditions," *Eng. Fail. Anal.*, vol. 46, pp. 92–103, 2014.
- [103] Y. Li et al., "Fatigue failure of dentin – composite disks subjected to cyclic diametral compression," *Dent. Mater.*, vol. 31, no. 7, pp. 778–788, 2015.
- [104] M. Izaham, Z. Abidin, J. Mahmud, M. Juzaila, A. Latif, and A. Jumahat, "Experimental and Numerical Investigation of SUP12 Steel Coil Spring," *Procedia Eng.*, vol. 68, pp. 251–257, 2013.

- [105] X. Wang and X. Zhang, "Simulation of dynamic cornering fatigue test of a steel passenger car wheel," *Int. J. Fatigue*, vol. 32, no. 2, pp. 434–442, 2010.
- [106] Anon, (2019). [online] Available at: <https://www.quora.com/Which-software-is-beter-ANSYS-or-Hyperworks>.
- [107] H. Sigwart, "Influence of residual stresses on the fatigue limit", In: *Proceedings of the International Conference on Fatigue of Metals*, Institution of Mechanical Engineers, London, UK, 1957.
- [108] J. Lu and D. Reiraint, "A review of recent development and applications in the field of X-ray diffraction for residual stress studies", *J. Strain Anal.* 33(2): 127–136, 1998.
- [109] P.S. Prevéy, N. Jayaraman and R. Ravindranath, "Incorporation of Residual Stresses in the Fatigue Performance Design of Ti-6Al-4V", In: *Proceedings International Conference on Fatigue Damage of Structural Materials V*. Hyannis, MA, USA, 2004.
- [110] William Cassada, John Liu, and James Staley, "Aluminium alloy for aircraft structure. *Advanced Materials and Processes*", 12: 27-29, 2002.
- [111] J. M. Story, G. W. Jarvis, H. R. Zonker and S. J. Murtha, "Issues and Trends in Automotive Aluminium Sheet Forming", *Proceedings of Sheet Metal and Stamping Symposium*. Detroit, MI. SAE SP-944. pp. 1-25, 1993.
- [112] S. Kuyucak and M. Sahoo, "A review of the machinability of copper-base alloys", *Canadian Metallurgical Quarterly*, 35(1): 1-15, 1996
- [113] Airbus Industrie Test Method standards, "AITM 1-0011 Constant amplitude fatigue testing of metallic materials", AIRBUS INDUSTRIE, Editor. Airbus Industrie, Engineering Directorate, Blagnac cedex, France. p. 1–24, 2001.
- [114] ASTM E3-2001, "Standard method of preparation of metallographic specimens", *Annual Book of ASTM Standards 03.01*, American Society for Testing and Materials, Philadelphia, 1983.
- [115] ASTM E384-99, "Standard test method for microhardness of material", *Annual Book of ASTM Standards 03.01*, American Society for Testing and Materials, 2003.
- [116] SAE International, "Residual Stress Measurement by X-Ray Diffraction", HS-784, pp. 77-84, 2003.

- [117] ASTM E1426 – 98, “Standard Test Method for Determining the Effective Elastic Parameter for X-Ray Diffraction Measurements of Residual Stress”, Annual Book of ASTM Standards 03.01, American Society for Testing and Materials, Philadelphia, 2003.
- [118] S. Han, T. Lee and B. Shin, “Residual stress relaxation of welded steel components under cyclic load”, *Materials Technology (Steel Research)*, 73(9): 414-420, 2002.
- [119] W.Z. Zhuang and G.R. Halford, “Investigation of residual stress relaxation under cyclic load”, *Int. J. Fatigu.*, 23: S31-S37, 2001.
- [120] Gages S. Measurement of Residual Stresses by the Hole-Drilling * Strain Gage Method TN-503-6.
- [121] R.J.H Paynter, A.H Mahmoudi, M.J Pavier, D.A Hills, “Residual stress measurement by deep hole drilling and trepanning – analysis with distributed dislocations,” 2009.
- [122] A.N.J Lu, J.F Havenot, P.M Dornoy, “Measurement of Residual Stress Distribution by the Incremental Hole-Drilling Method,” 1985.
- [123] A. Stupakov, T. Takagi, “Barkhausen Noise Testing of Residual Stresses Introduced by Surface Hardening Techniques,” 2013.
- [124] I. Khidirov, “Complimentary Contributor Copy,” 2017.
- [125] A.A Bunaciu, H.Y Aboul-enein, “X-Ray Diffraction : Instrumentation and Applications Critical Reviews in Analytical Chemistry X-Ray Diffraction,” Instrumentation and Applications. 2016.
- [126] M.E Turan, F. Aydin, Y. Sun, M. Cetin, “Residual stress measurement by strain gauge and X-ray diffraction method in different shaped rails,” *Eng Fail Anal*, 2018.
- [127] S.D Salehi, M.M Shokrieh, “Residual stress measurement using the slitting method via a combination of eigenstrain, regularization and series truncation techniques,” *Int J Mech Sci.*, 2018.
- [128] T.U Schüllli , S.J Leake, “ Current Opinion in Solid State & Materials Science X-ray nanobeam diffraction imaging of materials,” *Curr Opin Solid State Mater Sci.*, pp. 188–201, 2018.

- [129] A.C.F Fagundes, L.M Lopes, M. Antoniassi, R.S Sousa, I. Mazzaro, A.L.C Conceição, “Structural characterization of canine mammary tissue by x-ray diffraction.,” *Radiat Phys Chem* , vol 155, 2018.
- [130] C. Cui, Q. Zhang, Y. Bao, S. Han, Y. Bu, “Residual stress relaxation at innovative both-side welded rib-to-deck joints under cyclic loading,” *J Constr Steel Res*, vol 156, 2019.
- [131] R.L. Champoux, J.H. Underwood and J.A. Kapp. (1988), “Analytical and Experimental Methods for Residual Stress Effects in Fatigue”, ASTM STP 1004, American Society for Test and Materials, West Conshohocken, PA, 1988.
- [132] R. L. Mattson and W. S. Coleman, Jr, “Effect of shot peening variables and residual stresses on fatigue life of leaf spring specimens”, *Transactions, Society of Automotive Engineers*. 62: 546–556, 1954.
- [133] J. Morrow and G. M. Sinclair, “Cycle-dependent stress relaxation”, In: *Symposium on Basic Mechanisms of Fatigue*, ASTM STP 237. American Society for Testing and Materials, 1958.
- [134] H.R. Jhansale and T.H. Topper, “Engineering analysis of the inelastic stress response of a structural metal under variable cyclic strains”, In: *Cyclic Stress–Strain Behavior Analysis, Experimentation, and Failure Prediction*. ASTM STP 519, American Society for Testing and Materials pp. 246–270, 1973.
- [135] W.P. Wallace and J.P. Frankel, “Relief of residual stresses by single fatigue cycle”, *Welding Journal*. 38: 565s, 1949.
- [136] S. Kodama, “The behavior of residual stress during fatigue stress cycles”, In: *Proceedings of the International Conference on Mechanical Behavior of Metals II*. Kyoto. Society of Material Science, pp. 111–118, 1972.
- [137] H. Holzapfel, V. Schulze, O. Vohringer and E. Macherauch, “Residual stress relaxation in an AISI 4140 steel due to quasistatic and cyclic loading at higher temperatures”, *Materials Science and Engineering A* 248: 9–18, 1998.
- [138] Y. Ghaderi, A. Pourkamali, and A. Reza, “Thin-Walled Structures Study of the effective parameters on welding residual stress relaxation in aluminum cylindrical shells under cyclic pressure,” *Thin Walled Struct.*, vol. 143, no. October 2018, p. 106235, 2019.

- [139] C. Cui, Q. Zhang, Y. Bao, S. Han, and Y. Bu, “Residual stress relaxation at innovative both-side welded rib-to-deck joints under cyclic loading,” *J. Constr. Steel Res.*, vol. 156, pp. 9–17, 2019.
- [140] K. Zhu, Z. Li, G. Fan, R. Xu, and C. Jiang, “Thermal relaxation of residual stress in shot-peened CNT / Al – Mg – Si alloy composites,” vol. 8, no. 2, pp. 2201–2208, 2019.
- [141] J. Huang, K. Zhang, Y. Jia, C. Zhang, and X. Zhang, “Journal of Materials Science & Technology Effect of thermal annealing on the microstructure , mechanical properties and residual stress relaxation of pure titanium after deep rolling treatment,” vol. 35, pp. 409–417, 2019.
- [142] F. Uzun and A. M. Korsunsky, “Materials Science & Engineering A On the analysis of post weld heat treatment residual stress relaxation in Inconel alloy 740H by combining the principles of artificial intelligence with the eigenstrain theory,” vol. 752, no. February, pp. 180–191, 2019.
- [143] N. Srinivasan, L. Kumar, R. Kumar, and S. Baragetti, “Residual stress gradient and relaxation upon fatigue deformation of diamond-like carbon coated aluminum alloy in air and methanol environments,” vol. 160, pp. 303–312, 2018.
- [144] K. W. Jones and R. W. Bush, “Investigation of residual stress relaxation in cold expanded holes by the slitting method,” vol. 179, pp. 213–224, 2017.
- [145] Q. Wang, X. Liu, Z. Yan, Z. Dong, and D. Yan, “On the mechanism of residual stresses relaxation in welded joints under cyclic loading,” vol. 105, pp. 43–59, 2017.
- [146] B. Vierneusel, L. Benker, S. Tremmel, M. Göken, and B. Merle, “Isolating the effect of residual stresses on coating wear by a mechanical stress relaxation technique,” vol. 638, pp. 159–166, 2017.
- [147] X. Xie, W. Jiang, Y. Luo, S. Xu, J. Gong, and S. Tu, “A model to predict the relaxation of weld residual stress by cyclic load : Experimental and finite element modeling,” vol. 95, pp. 293–301, 2017.
- [148] O. S. Zaroog, A. Ali, B. B. Sahari, and R. Zahari, “Modeling of residual stress relaxation of fatigue in 2024-T351 aluminium alloy,” *Int. J. Fatigue*, vol. 33, no. 2, pp. 279–285, 2011.
- [149] A.S Guide, “Crash Analysis with RADIOSS: A Study Guide,” 2015.

- [150] W. A. Mulder, E. Zhebel, and S. Minisini, “Geophysical Journal International,” pp. 1123–1133, 2014.
- [151] T. Ladygowski and W. Sumelka, “Limitation in Application of Finite Element Method in Acoustic Numerical Simulation”, Journal of Theoretical and Applied Mechanics, vol 44, pp. 849 – 865, 2006.

APPENDIX A

RADIOSS CODING FOR RESIDUAL STRESS RELAXATION SIMULATION

```

#RADIOSS STARTER
##=====
==
##
## Radioss Input Deck Generated by HyperMesh Version : 2017.2.0.16
## Generated using HyperMesh-Radioss Template Version : 2017.2
## Date: 02-25-2019   Time: 11:23:21
##
## Title
##-----
-----
/TITLE
##-----
-----
## Material Law No 1. ELASTIC
##-----
-----
#---1---|---2---|---3---|---4---|---5---|---6---|---7---|---8---|---9---
-|---10---|
#           E           nu
/MAT/ELAST/2
ball
#           RHO_I
7.850000000000000E-09           0.0
           210000.0           0.3
##-----
-----
## Material Law No 36. ELASTIC PLASTIC PIECEWISE LINEAR
##-----
-----
#           E           Nu           Eps_p_max           Eps_t
Eps_m
# N_funct F_smooth           C_hard           F_cut           Eps_f
VP
# fct_IDp           Fscale   Fct_IDE           EInf           CE
# func_ID1 func_ID2   func_ID3   func_ID4   func_ID5
#           Fscale_1           Fscale_2           Fscale_3           Fscale_4
Fscale_5
#           Eps_dot_1           Eps_dot_2           Eps_dot_3           Eps_dot_4
Eps_dot_5
/MAT/PLAS_TAB/1
dogbone
#           RHO_I
7.800000000000000E-09           0.0
           200000.0           0.29           0.0           0.0
0.0           1           0           0.0           0.0           0.0
0
           0           0.0           0           0.0           0.0
           1
           0.0
           0.0
##-----
-----
## NODES
##-----
-----
/NODE
      8377      11.739955458019      -0.36780358451273      6.4069146462815
      8378      11.725409164736      0.6172650995099      6.4093638236356
      8379      11.728999675901      1.6001926810969      6.4094651831823
      8380      11.727010902079      2.5814008661397      6.4112154285787
      8381      11.728451422859      3.5647526036598      6.4118044701992
      8382      11.72763664948      4.5453185544225      6.4122971537253
      8383      11.727549440399      5.5278826138541      6.4130431700514
      8384      11.726082621034      6.5090461117853      6.4135432702368
      8385      11.725885887846      7.4907221521842      6.413423240498
      8386      11.727792343566      8.4723756329512      6.4133071081133

```

```

8387      11.727694317385      9.4545604129144      6.4123097612776
8388      11.728393329626      10.43541657428      6.4117282405873
8389      11.727094602916      11.418859367586      6.4112048297309
8390      11.728483383695      12.399783801919      6.409687291623
8391      11.725827949745      13.382952271991      6.4093676704129
8392      11.725780200453      14.364736128821      6.40691593328
8393      12.717792319549      14.369250518476      6.4100959526601
8394      13.710003461357      14.372799873427      6.4113268947761
8395      14.703963117763      14.375791516203      6.4151966330451
##-----
## General Solid Property Set (pid 14)
##-----
#---1---|---2---|---3---|---4---|---5---|---6---|---7---|---8---|---9---
-|---10---|
#- 7. GEOMETRICAL SETS:
#---1---|---2---|---3---|---4---|---5---|---6---|---7---|---8---|---9---
-|---10---|
#
#          q_a          q_b          h          LAMBDA_V
MU_V
#          dt_min  istrain  IHKT
#---1---|---2---|---3---|---4---|---5---|---6---|---7---|---8---|---9---
-|---10---|
#- 8. FUNCTIONS:
#---1---|---2---|---3---|---4---|---5---|---6---|---7---|---8---|---9---
-|---10---|
/PROP/SOLID/1
solid
#  Isolid  Ismstr          Icpres          Inpts  Itetra  Iframe
#          24          0          0          0          0
0.0          0.0          0.0          0.0          0.0
0.0          0.0          1          0
##-----
## Functions
##-----
##HWCOLOR curves 1 4
/FUNCT/1
Engineering          TRUE          Effective
#          X          Y
#          0.0          1.985016346
0.015016983          24.23365529
0.030005263          65.48548889
0.045010943          110.5720215
0.060017537          157.0628866
0.075005203          204.0631917
0.09001191          251.178243
0.105000094          297.8753052
0.120006502          331.5326131
0.134999692          336.6884359
0.150048345          351.0821533
0.165004462          365.7616781
0.180049196          379.0201009
0.195014238          390.5030518
0.210014209          400.4747314
0.225013241          409.120931
0.240013227          416.6728516
0.255013406          423.1102702
0.270013362          428.5447998
0.285014302          433.1363932
0.300015152          436.927002
0.315015078          440.0191243
0.330014884          442.4778239
0.345014513          444.4156087
0.360013843          445.8827718
0.375014335          446.8347575
0.390013933          447.3947754
0.405012608          447.5604655
0.420013398          447.27771
0.435013771          446.5690918
0.450013638          445.2346598
0.465014756          443.1388753
0.480015814          440.0621745

```

```

0.495014817      435.6437174
0.510014594      429.6942546
0.525014102      422.0086263
0.540014029      412.4603678
0.555013955      400.7045492
0.570013344      386.2539063
0.595014572      352.7954915
0.599014461      340.5782064
#---1---|---2---|---3---|---4---|---5---|---6---|---7---|---8---|---9---
-|---10---|
##HWCOLOR curves 2 5
/FUNCT/2
New function
#           X           Y
           0.0           1996.8
           0.5           19968.0
           1.0           1996.8
           2.0           0.0
##-----
## Concentrated Loads
##-----
#---1---|---2---|---3---|---4---|---5---|---6---|---7---|---8---|---9---
-|---10---|
#- 9. CONCENTRATED LOADS:
#---1---|---2---|---3---|---4---|---5---|---6---|---7---|---8---|---9---
-|---10---|
##HWCOLOR loadcollectors 2 57
/CLOAD/2
pull
##funct_IDT      Dir      skew_ID sensor_ID grnod_ID      Ascalex
           2           X           0           0           9           1.000000000000000E-03
1.0
/GRNOD/NODE/9
grnodnode.2
      20021
##-----
## N Noded Rigid Bodies
##-----
#---1---|---2---|---3---|---4---|---5---|---6---|---7---|---8---|---9---
-|---10---|
#- 10. RIGID BODIES:
#---1---|---2---|---3---|---4---|---5---|---6---|---7---|---8---|---9---
-|---10---|
#           Jxx           Jyy           Jzz
#           Jxy           Jyz           Jxz
#Ioptoff Iexpams
##HMOVE elements 1 3
/RBODY/1
rigid
##      RBID      ISENS      NSKEW      ISPHER      MASS      Gnod_id      IKREM
0      20020      0           0           0           0.0           6           0
           0.0           0.0           0.0
           0.0           0.0           0.0
0
/GRNOD/NODE/6
RBODY_group_6_of_NODE
8913      8905      8906      8907      8908      8909      8910      8911      8912
8923      8915      8916      8917      8918      8919      8920      8921      8922
8962      8925      8926      8927      8928      8929      8930      8931      8961
8972      8964      8965      8966      8967      8968      8969      8970      8971
8982      8974      8975      8976      8977      8978      8979      8980      8981
8992      8984      8985      8986      8987      8988      8989      8990      8991
9002      8994      8995      8996      8997      8998      8999      9000      9001
9012      9004      9005      9006      9007      9008      9009      9010      9011

```

	9014	9015	9016	9017	9018	9019	9020	9021
9022	9023							
	9340	9341	9342	9343	9344	9345	9346	9347
9348	9349							
	9350	9351	9352	9353	9354	9355	9356	9357
9358	9359							
	10310	10311	10312	10313	10314	10315	10316	10317
10318	10319							
	10320	10321	10322	10323	10324	10325	10326	10327
10328	10329							
	11360	11361	11362	11363	11364	11365	11366	11367
11368	11369							
	11370	11371	11372	11373	11374	11375	11376	11377
11378	11379							
	11580	11581	11582	11583	11584	11585	11586	11587
11588	11589							
	11590	11591	11592	11593	11594	11595	11596	11597
11598	11599							
	11615	11616	11617	11618	11619	11620	11621	11622
11623	11624							
	11625	11626	11627	11628	11629	11630	11631	11632
11633	11634							
	11920	11921	11922	11923	11924	11925	11926	11927
11928	11929							
	11930	11931	11932	11933	11934	11935	11936	11937
11938	11939							
	11940	11941	11942	11943	11944	11945	11946	11947
11948	11949							
	11950	11951	11952	11953	11954	12000	12001	12002
12003	12004							
	12005	12006	12007	12008	12009	12010	12011	12012
12013	12014							
	12015	12016	12017	12018	12019	12060	12061	12062
12063	12064							
	12065	12066	12067	12068	12069	12150	12151	12152
12153	12154							
	12460	12461	12462	12463	12464	12465	12466	12467
12468	12469							
	12485	12488	12489	12492	12493	12496	12497	12500
12501	12504							
	12565	12566	12567	12568	12569	12570	12571	12572
12573	12574							
	12575	12576	12577	12578	12579	12580	12581	12582
12583	12584							
	12585	12586	12587	12588	12589	12625	12626	12627
12628	12629							
	12630	12631	12632	12633	12634	12635	12636	12637
12638	12639							
	12640	12641	12642	12643	12644	12740	12741	12742
12743	12744							
	12745	12746	12747	12748	12749	12750	12751	12752
12753	12754							
	12946	12948	12950	12952	12954	13065	13066	13067
13068	13069							
	13070	13071	13072	13073	13074	13075	13076	13077
13078	13079							
	13100	13101	13102	13103	13104	13105	13106	13107
13108	13109							
	13110	13111	13112	13113	13114	13115	13116	13117
13118	13119							
	13120	13121	13122	13123	13124	13130	13131	13132
13133	13134							
	13135	13136	13137	13138	13139	13140	13141	13142
13143	13144							
	13145	13146	13147	13148	13149	13215	13216	13217
13218	13219							
	13220	13221	13222	13223	13224	13265	13266	13267
13268	13269							
	13370	13371	13372	13373	13374	13375	13376	13377
13378	13379							
	13380	13381	13382	13383	13384	13445	13446	13447
13448	13449							
	13510	13511	13512	13513	13514	13605	13606	13607
13608	13609							
	13610	13611	13612	13613	13614	13620	13621	13622
13623	13624							

```

13660 13661 13662 13663 13664 13665 13666 13667
13668 13669
13670 13671 13672 13673 13674 13680 13681 13682
13683 13684
13685 13686 13687 13688 13689 13710 13711 13712
13713 13714
13715 13716 13717 13718 13719 13720 13721 13722
13723 13724
13735 13736 13737 13738 13739 13770 13771 13772
13773 13774
13790 13791 13792 13793 13794 13810 13811 13812
13813 13814
13885 13886 13887 13888 13889 13890 13891 13892
13893 13894
13900 13901 13902 13903 13904 13910 13911 13912
13913 13914
#---1-----|-----2-----|-----3-----|-----4-----|-----5-----|-----6-----|-----7-----|-----8-----|-----9-----|
-|-----10-----|
#
# Jxx Jyy Jzz
# Jxy Jyz Jxz
#Ioptoff Iexpams
##HMOVE elements 2 3
/RBODY/2
NULL
## RBID ISENS NSKEW ISPHER MASS Gnod_id IKREM
0 20021 0 0 0 0.0 7 0
0 0 0.0 0.0 0.0
0 0.0 0.0
/GRNOD/NODE/7
rigid63939nodeset
9119 9120 9121 9122 9123 9124 9125 9126
9127 9128
9129 9130 9131 9132 9133 9134 9135 9136
9137 9138
9139 9140 9141 9142 9143 9144 9145 9230
9231 9232
9233 9234 9235 9236 9237 9238 9239 9241
9242 9243
9244 9245 9246 9248 9250 9252 9253 9254
9255 9256
9257 9258 9260 9262 9264 9265 9266 9267
9268 9269
9270 9271 9272 9273 9274 9275 9276 9277
9278 9279
9280 9281 9282 9283 9284 9285 9286 9287
9288 9289
9290 9291 9292 9293 9294 9295 9296 9297
9298 9299
9585 9586 9587 9588 9589 9590 9591 9592
9593 9594
9595 9596 9597 9598 9599 9600 9601 9602
9603 9604
9725 9726 9727 9728 9729 9730 9731 9732
9733 9734
9735 9736 9737 9738 9739 9740 9741 9742
9743 9744
9965 9966 9967 9968 9969 9970 9971 9972
9973 9974
9975 9976 9977 9978 9979 9980 9981 9982
9983 9984
10140 10141 10142 10143 10144 10145 10146 10147
10148 10149
10150 10151 10152 10153 10154 10155 10156 10157
10158 10159
10645 10646 10647 10648 10649 10650 10651 10652
10653 10654
10655 10656 10657 10658 10659 10660 10661 10662
10663 10664
10690 10691 10692 10693 10694 10695 10696 10697
10698 10699
10700 10701 10702 10703 10704 10785 10786 10787
10788 10789
10790 10791 10792 10793 10794 10795 10796 10797
10798 10799

```

	11080	11081	11082	11083	11084	11085	11086	11087
11088	11089							
	11115	11116	11117	11118	11119	11120	11121	11122
11123	11124							
	11135	11136	11137	11138	11139	11140	11141	11142
11143	11144							
	11145	11146	11147	11148	11149	11150	11151	11152
11153	11154							
	11510	11511	11512	11513	11514	11550	11551	11552
11553	11554							
	11555	11556	11557	11558	11559	11560	11561	11562
11563	11564							
	11565	11566	11567	11568	11569	11635	11636	11637
11638	11639							
	11640	11641	11642	11643	11644	11645	11646	11647
11648	11649							
	11985	11986	11987	11988	11989	11990	11991	11992
11993	11994							
	11995	11996	11997	11998	11999	12185	12186	12187
12188	12189							
	12190	12191	12192	12193	12194	12195	12196	12197
12198	12199							
	12200	12201	12202	12203	12204	12410	12411	12412
12413	12414							
	12415	12416	12417	12418	12419	12470	12471	12472
12473	12474							
	12530	12531	12532	12533	12534	12545	12546	12547
12548	12549							
	12550	12551	12552	12553	12554	12555	12556	12557
12558	12559							
	12560	12561	12562	12563	12564	12645	12646	12647
12648	12649							
	12650	12651	12652	12653	12654	12655	12656	12657
12658	12659							
	12680	12681	12682	12683	12684	12700	12701	12702
12703	12704							
	12705	12706	12707	12708	12709	12710	12711	12712
12713	12714							
	12715	12716	12717	12718	12719	12805	12806	12807
12808	12809							
	12810	12811	12812	12813	12814	12815	12816	12817
12818	12819							
	13090	13091	13092	13093	13094	13095	13096	13097
13098	13099							
	13180	13181	13182	13183	13184	13185	13186	13187
13188	13189							
	13280	13281	13282	13283	13284	13285	13286	13287
13288	13289							
	13295	13296	13297	13298	13299	13300	13301	13302
13303	13304							
	13360	13361	13362	13363	13364	13485	13486	13487
13488	13489							
	13490	13491	13492	13493	13494	13635	13636	13637
13638	13639							
	13645	13646	13647	13648	13649	13650	13651	13652
13653	13654							
	13655	13656	13657	13658	13659	13695	13696	13697
13698	13699							
	13775	13776	13777	13778	13779	13830	13831	13832
13833	13834							
	13835	13836	13837	13838	13839	13840	13841	13842
13843	13844							
	13880	13881	13882	13883	13884	13905	13906	13907
13908	13909							

```

##-----
-----
## Sets
##-----
-----
##-----
-----
## Parts
##-----
-----
#---1---|---2---|---3---|---4---|---5---|---6---|---7---|---8---|---9---
-|---10---|
#- 6. PARTS:

```

```

#---1---|---2---|---3---|---4---|---5---|---6---|---7---|---8---|---9---
-|---10---|
##HWCOLOR components 2 5
/PART/2
solid
      1      1
##-----
## Time History - Nodes
##-----
/TH/NODE/3
TH NODE
##   var1      var2      var3      var4      var5      var6      var7      var8
DEF
    20020          0
    20021          0
#   NODid      Iskew
##-----
## Time History - Elems
##-----
/TH/RBODY/2
TH RBODY
##   var1      var2      var3      var4      var5      var6      var7      var8
DEF
      1      2
#---1---|---2---|---3---|---4---|---5---|---6---|---7---|---8---|---9---
-|---10---|
#- 11. TIME HISTORIES:
#---1---|---2---|---3---|---4---|---5---|---6---|---7---|---8---|---9---
-|---10---|
#   Obj1      Obj2      Obj3      Obj4      Obj5      Obj6      Obj7      Obj8
Obj9      Obj10
#---1---|---2---|---3---|---4---|---5---|---6---|---7---|---8---|---9---
-|---10---|
##-----
## Time History - Parts
##-----
##-----
## Time History - Frames
##-----
##-----
## Time History - Interfaces and Rwalls
##-----
##-----
## Time History - Cyl Joints
##-----
##-----
## Time History - Monv, Accel and Sections
##-----
##-----
## Time History - Subsets
##-----
##-----
## Time History - Control vols
##-----
##-----
## Time History - Cross Sections
##-----
##-----

```

```

##-----
##-----
## Time History - Load Collectors
##-----
##-----
## Time History - Sets
##-----
##-----

##-----
## End Of Radioss Block Deck
##-----
/END
##-----

## HM_FOOTER_COMMENTS - BEGIN
##-----
##-----
#--1---|---2---|---3---|---4---|---5---|---6---|---7---|---8---|---9---
-|---10---|
#--1---|---2---|---3---|---4---|---5---|---6---|---7---|---8---|---9---
-|---10---|
## HM_FOOTER_COMMENTS - END

```

APPENDIX B

SAMPLE OF STRESS STRAIN DATA FROM EXPERIMENTAL TENSILE TEST FOR SIMULATION MATERIAL PROPERTIES DEFINITION

Strain (%)	Stress
0	1.985016
0.015017	24.23366
0.030005	65.48549
0.045011	110.572
0.060018	157.0629
0.075005	204.0632
0.090012	251.1782
0.105	297.8753
0.120007	331.5326
0.135	336.6884
0.150048	351.0822
0.165004	365.7617
0.180049	379.0201
0.195014	390.5031
0.210014	400.4747
0.225013	409.1209
0.240013	416.6729
0.255013	423.1103
0.270013	428.5448
0.285014	433.1364
0.300015	436.927
0.315015	440.0191
0.330015	442.4778
0.345015	444.4156
0.360014	445.8828
0.375014	446.8348
0.390014	447.3948
0.405013	447.5605
0.420013	447.2777
0.450014	445.2347
0.465015	443.1389
0.480016	440.0622
0.495015	435.6437
0.510015	429.6943
0.525014	422.0086
0.540014	412.4604
0.555014	400.7045
0.595015	352.7955
0.599014	340.5782

